A radio and near-infrared study of 6.7 GHz methanol maser sources

Sharmila Goedhart

February 26, 2004

A radio and near-infrared study of 6.7 GHz methanol maser sources

Sharmila Goedhart B.Sc., B.Sc.(Hons.), M.Sc

Thesis submitted in the Department of Physics of the Potchefstroom University for Christian Higher Education in fulfilment of the requirements for the degree of Philospiae Doctor.

Supervisors: Prof. D. J. van der Walt, Dr M. J. Gaylard

Hartebeesthoek

February 26, 2004

Abstract

The 6.7 GHz $5_1 - 6_0$ A^+ methanol maser transition was discovered relatively recently, in 1991. The exact nature of these masers is not known to date, but it seems likely that they are closely associated with high mass stars ($M \gtrsim 10\ M_\odot$) in their earliest stages of evolution. Since the molecular cloud is optically thin to emission at radio wavelengths, the methanol masers can provide information about conditions deep in the star formation region.

Twelve southern 6.7 GHz methanol maser sources were imaged in the near-infrared (NIR) at I, J, H and K bands using the 1.5-m telescope at the Cerro Tololo Interamerican Observatory (Chile). Astrometry accurate to 0.5 arcsec and photometry down to a limiting magnitude of 14 was obtained. The positions of known H II regions, water masers, hydroxyl masers and mid- and far-infrared objects in the region are examined in order to try to determine the nature of the methanol maser sources. Seven out of 14 methanol maser sites were found to be within 8 kAU of a NIR source with colours characteristic of a deeply embedded source. In three cases, no NIR source, H II region, water maser or hydroxyl maser could be found in likely association with the methanol masers, leaving the methanol maser as the only indication that star formation is taking place at these locations.

An intensive programme was started in January 1999 to monitor a sample of 56 sources at 6.7 GHz using the Hartebeesthoek 26-m telescope. The observations were taken at 1–2 week intervals, with daily observations when possible if a maser was seen to be varying rapidly. It was found that the majority of the sources have a significant level of variability. In addition, nine sources were found to have periodic or quasi-periodic variations. The source G9.62+0.20E was the first such source detected in the dataset, and is the first reported instance of a periodic maser associated with a star formation region.

High-resolution images were obtained of the source G9.62+0.20E during a flare in 2001 using the Very Long Baseline Array (VLBA). The maser spots increased in intensity, with no changes to their morphology or relative positions during the flare. This indicates that the flare originated in an increase in radiation beyond the maser regions.

Opsomming

Die $5_1 - 6_0\ A^+$ (6.7 GHz) oorgang van metanol is redelik onlangs (1991) as 'n wydverspreide astronomiese maser ontdek. Die presiese aard van hierdie masers is tans nog onbekend. Daar bestaan egter sterk getuienis dat hulle 'n noue verbintenis met hoë-massa (swaarder as ongeveer $10M_\odot$) sterre in hul vroegste stadium van ontwikkeling het. Aangesien die molekulê wolk waarin hierdie jong sterre geleë is en waarin die maserstraling sy oorsprong het, opties dun is vir sentimetergolflengte radiostraling kan die metanolmasers belangrike inligting oor die toestande diep in stervormingsgebiede oplewer.

Naby-infrarooi (NIR) (IJHK) beelde van 12 suidelike 6.7 GHz metanolmaserbronne is met die 1.5m teleskoop van die Cerro Tololo Interamerican Observatory (Chile), verkry. Astrometrie met 'n onsekerheid van 0.5 boogsekondes en fotometrie met 'n magnitudegrens van 14 is behaal. Die posisies van naby-geleë H II gebiede, watermasers, hidroksielmasers en mid- en ver-infrarooivoorwerpe is ondersoek om die aard van die metanolmaserbronne te bepaal. Sewe van die 14 metanolmaserposisies is binne 8000 astronomiese eenhede vanaf 'n hoogsverrooide NIR-bron. In drie gevalle kon geen NIR-bron, H II gebied, watermaser of hidroksielmaser wat moontlik 'n verbintenis met die metanolmasers het, gevind word nie. Dit laat die metanolmaser as die enigste aanduiding dat swaar sterre besig is om binne hierdie gebied te vorm.

'n Intensiewe program is in Januarie 1999 begin om 'n groep van 56 metanolmaserbronne by 6.7 GHz te monitor. Die waarnemings is in 1–2 week intervalle geneem, met daaglikse waarnemings waar moontlik indien 'n maser vinnige veranderinge vertoon het. Daar is bevind dat die meerderheid bronne 'n beduidende vlak van veranderlikheid vertoon. Daarby is nege bronne met periodiese of kwasiperiodiese verhelderings gevind. Die bron G9.62+0.20E is die eerste sodanige periodiese metanol maser wat ontdek is asook die eerste periodiese maser wat met 'n stervormingsgebied geassosieer is.

Baie hoë resolusie radio beelde van die bron G9.62+0.20E is in 2001 tydens 'n fase van maser verheldering met die Very Large Baseline Array (VLBA) verkry. Die waarnemings toon dat die maservlekke tydens die verheldering slegs in intensiteit toeneem met geen verandering van morfologie of relatiewe posisies nie. Hierdie gedrag suggereer dat die verheldering heelwaarskynlik toegeskryf kan word aan 'n verandering in die stralingsveld van die onderliggende HII gebied en/of van die infrarooi stralingsveld in die molekulêre wolk.

Acknowledgements

First of all I would like to thank my supervisors, Johan van der Walt and Mike Gaylard, without whom this thesis would never have been started, let alone completed. Johan introduced me to methanol masers during my MSc studies, and instilled in me a deep interest in these strange but wonderful objects. I especially have to thank Johan for making the long drive from Potchefstroom to Hartebeesthoek whenever I needed to have an in-depth discussion with him. I knew nothing about radio astronomy when I started at Hartebeesthoek, but Mike patiently guided me through the process of calculating integration times, creating source files and reducing spectra. No matter how busy they have been, they have always taken time to answer my sometimes rather stupid questions.

I would like to thank Dr George Nicolson for his generous allocation of observing time, and for believing me whenever I told him that G9.62+0.20 was about to flare. He has dealt with many a frantic call at odd hours, and patiently walked me through solving observing problems. His achievements and great store of knowledge have been truly inspiring.

While the level of automation at HartRAO is very good, someone still had to physically set up the spectroscopy observing runs. Thank you to the following people for sharing the load so that I did not have to drive out to HartRAO every weekend: George Nicolson, Mike Gaylard, Beate Woermann, Augustine Chukwude, Marion West and Sarah Buchner.

Ian Glass at SAAO kindly let me tag along while he was doing engineering tests on a new near-infrared camera so that I could learn more about infrared imaging in preparation for my run at CTIO, while Ron Probst and Bob Blum at CTIO gave me invaluable advice on the imaging and reduction techniques.

The VLBA imaging project would never have happened without Vincent Minier. Since I knew nothing about VLBI techniques when we formulated the proposal, his input on the necessary observing parameters was invaluable, as was his guideline for data reduction. I am indebted to Mark Claussen at NRAO for making sure that the VLBA observations were scheduled at the necessary intervals, and for taking pity on me and setting up the SCHED file for me. Athol Kemball taught me more about amplitude calibration and how to make sure that the calibration was as accurate as possible.

I am grateful to Marisa Nickola for sharing the tedious task of cross-checking my bibliography and helping with the Afrikaans abstract.

My thanks to Peter Stocker for proof-reading my thesis.

Thank you also to everyone at HartRAO, for your friendship and encouragement.

Last but not least, I would like to thank my husband Andrew for always being there for me.

Contents

1 Introduction **1**

1.1 High mass star formation 2

1.1.1 Accretion vs coalescence 2

1.1.2 Evolutionary sequence 3

1.2 Observational probes of high mass star formation 3

1.3 Thesis outline 6

2 Near-infrared imaging **8**

2.1 Introduction 8

2.2 Observations and data reduction 9

2.3 Results 11

2.4 Notes on individual sources 18

2.4.1 G10.33–0.17 18

2.4.2 G12.68–0.18 (W33B) 20

2.4.3 G12.91–0.26 (W33A) 21

2.4.4 G45.07+0.13 22

2.4.5 G52.67–1.09 23

2.4.6 G328.81+0.63 23
2.4.7 G336.01–0.82 25
2.4.8 G337.92–0.46 25
2.4.9 G339.62–0.12 26
2.4.10 G339.88–1.26 26
2.4.11 G340.79–0.10 28
2.4.12 G351.78–0.54 30
2.5 Discussion 30
2.5.1 Association of methanol masers with near-infrared objects 30
2.5.2 Relation of methanol masers to other star formation tracers 31
2.5.3 MSX and IRAS sources 32
2.6 Summary 33

3 6.7 GHz maser monitoring at HartRAO 35

3.1 Introduction 35
3.2 Observations 36
3.3 Source selection 37
3.4 Overview of results 40
3.4.1 Variability index 40
3.4.2 Notes on individual sources 46
3.4.3 Summary of results 53
3.5 Discussion 54

4 Investigation into possible periodic masers 57

4.1 Introduction 57

4.2 Identifying periodic masers 58

4.3 Notes on individual sources 59

4.3.1 G9.62+0.20E 59

4.3.2 G188.95+0.89 61

4.3.3 G196.45-1.68 63

4.3.4 G312.11+0.26 65

4.3.5 G316.64-0.09 67

4.3.6 318.95-0.20 67

4.3.7 G328.25-0.53 67

4.3.8 G331.13-0.24 70

4.3.9 G338.93-0.06 72

4.3.10 G339.62-0.12 72

4.4 Summary and discussion 76

4.4.1 Periodic mechanisms in star formation regions 76

4.5 Conclusions 80

5 VLBA imaging of G9.62+0.20E during a flare 82

5.1 Introduction 82

5.2 Observations 82

5.3 Reductions 84

5.3.1 Amplitude calibration 85

5.3.2 Phase calibration 85

5.3.3 Imaging 86

5.4 Results 89

5.4.1 Structure of the maser components 89

5.4.2 Variations during the flare 95

5.5 Discussion 99

5.6 Conclusion 101

6 Summary and outlook **102**

6.1 Variability of 6.7 GHz methanol masers 102

6.2 The environment of methanol masers 103

6.3 Suggestions for future work 104

A Zero magnitude fluxes **106**

B Contour plots **108**

List of Figures

2.1 Three-colour composite image showing overlap between optical and infrared sources for G336.01–0.82 10

2.2 H-K vs J-K diagram of the stars possibly associated with methanol masers 12

2.3 K vs H-K diagram showing sources in all the fields imaged . . . 13

2.4 Three-colour composite image of G10.33-0.17 19

2.5 Three-colour composite image of G12.68-0.18 21

2.6 Three-colour composite image of G12.91-0.26 22

2.7 Three-colour composite image of G45.07+0.13 23

2.8 Three-colour composite image of G52.67-1.09 24

2.9 Three-colour composite image of G328.81+0.63 24

2.10 Three-colour composite image of G336.01-0.82 26

2.11 Three-colour composite image of G337.92-0.46 27

2.12 Three-colour composite image of G339.62-0.12 27

2.13 Three-colour composite image of G339.88-1.26 28

2.14 Three-colour composite image of G340.79-0.10 29

2.15 Three-colour composite image of G351.78-0.54 29

2.16 Venn diagram showing the association of methanol maser sources with other radio sources 33

3.1 Normalised time-series for sources showing strongly correlated variations. 37

3.2 Cross-correlation of the time-series of dominant feature in G339.88–1.26 with time-series from other sources showing similar variations. 38

3.3 Time-series of two maser features in G337.92–0.46. 38

3.4 Histogram of the variability indices. The most variable sources are identified on the histogram. 42

3.5 Time-series of the –5.786 km.s^{-1} feature in NGC6334F. This feature has the highest variability index in the sample. 42

3.6 Time-series of a moderately variable feature in G339.62–0.12 (I=2.98) and a non-varying feature in G10.47+0.03 (I=-0.04). . 43

3.7 Variability index plotted against average flux density. Note that the scales are logarithmic. 43

3.8 Range of variation in spectrum of G213.71-12.60. 46

3.9 Time-series for selected velocity channels in G213.71-12.60. . . 47

4.1 Time-series analysis of G9.62+0.20E 60

4.2 Cross-correlation between features at 1.26 km.s^{-1} and -0.14 km.s^{-1} for G9.62+0.20E. 61

4.3 Time-series analysis of G188.95+0.89 62

4.4 Time-series analysis of G196.45-1.68 64

4.5 Cross-correlation between time-series for different features in G196.45-1.68 65

4.6 Time-series analysis of G312.11+0.26 66

4.7 Time-series analysis of G316.66-0.09 68

4.8 Time-series analysis of G318.95-0.20 69

4.9 Time-series analysis of G328.25-0.53 71

4.10 Cross-correlation between time-series for G328.24-0.55 72

4.11 Time-series analysis of G331.12-0.24 73

4.12 Time-series analysis of G338.93-0.06 74

4.13 Time-series analysis of G339.62-0.12 75

4.14 Polynomial fits to folded time-series of periodic masers 77

5.1 Timing of VLBA observations relative to the flare cycle of feature C 84

5.2 *uv* coverage for observation A. 87

5.3 Dirty beam for observation epoch A. 87

5.4 Cleaned image of channel at 3.6 km.s^{-1} 88

5.5 Distribution of maser features in G9.62+0.20E 90

5.6 Close-up images of the velocity structure of selected maser components 92

5.7 Examples of total power and cross-power spectra 93

5.8 Visibility maplitude vs. *uv*-distance for the maser features . . . 94

5.9 Zero-moment images for each epoch 97

5.10 VLBA time-series for maser features in G9.62+0.20E 98

5.11 Comparison of flux density at 12.2 and 6.7 GHz for two velocity features 99

1 Intensity contour plot for G9.62+0.20 109

2 Intensity contour plot for G188.95-0.89 110

3 Intensity contour plot for G196.45-1.68 111

4 Intensity contour plot for G312.11+0.26 112

5 Intensity contour plot for G318.95-0.20 113

6 Intensity contour plot for G316.64-0.09 114

7 Intensity contour plot for G328.24-0.53 115

8 Intensity contour plot for G331.13-0.24 116

9 Intensity contour plot for G338.93-0.06 117

10 Intensity contour plot for G339.62-0.12 118

List of Tables

2.1 Central wavelengths of filters 9

2.2 J, H and K band magnitudes and flux densities of infrared objects close to the methanol maser positions 11

2.3 Positions of radio sources and references 15

2.4 Kinematic distances to methanol maser sources 16

2.5 Distances between methanol masers and other objects in the fields 16

3.1 Observing parameters for large and small velocity range sources 36

3.2 List of sources monitored at 6.7 GHz. The V_{lsr} on which the bandwidth was centred is given. 39

3.3 List of most variable maser peaks 6.7 GHz. 44

4.1 Results of sinusoidal fit to light curves from G196.45-1.68 65

4.2 Possible periodic masers 76

4.3 Keplerian orbital radii for objects orbiting a B0 star with the specified periods. 80

5.1 Timing of the VLBA observations 83

5.2 Velocity ranges of 12.2 GHz maser components in G9.62+0.20E 89

5.3 Beam parameters for the different epochs with Pie Town, Hancock and Fort Davis flagged out for all epochs. 95

A.1 Fluxes for Vega on the LCO system 107

Chapter 1

Introduction

Massive stars ($M \gtrsim 10\ M_{\odot}$) play an important role in the dynamical and chemical evolution of the Galaxy. Their radiation ionizes and eventually disperses the surrounding natal molecular cloud, halting further star formation in the immediate area eg the Trapezium cluster in Orion (Hillenbrand, 1997) or the Carina Nebula (Smith et al., 2003, and references therein). At the end of their lifetimes, they explode as supernovae, releasing a great deal of energy into the interstellar medium, creating shockwaves which could eventually trigger the next wave of star formation. In addition, the supernovae are responsible for the nucleosynthesis of heavy elements in the Galaxy, altering the composition of the interstellar medium (McKee & Ostricker, 1977). Thus knowledge of their birth-rate and evolutionary time-scales is essential for the understanding of Galactic evolution.

Despite the profound impact of massive stars, the process by which they form is still one of the unsolved problems in astrophysics. The natal stellar environment is deeply obscured – Molinari et al. (1998) found that their candidate for a high mass protostar had an estimated 2000 magnitudes of visual extinction towards it. The solar neighbourhood has a scarcity of high mass star formation regions, with the Orion nebula the closest at 450 pc, while most high mass star formation complexes are at a few kpc. This combination of greater distance and great extinction means that observational studies of high-mass star formation are extremely challenging and thus far no conclusive observations have been made that have been able to distinguish between the different scenarios of high mass star formation.

In Section 1 of this chapter, I will discuss the existing theories of high mass star formation. In Section 2, I will discuss the observational probes that can be used to examine these regions and I will outline the thesis in section 3.

1.1 High mass star formation

1.1.1 Accretion vs coalescence

Low mass star formation is reasonably well explained by the initial gravitational collapse of a molecular cloud and subsequent accretion by way of a rotating disc onto a proto-stellar core (Palla & Stahler, 1993). Circumstellar discs have been directly imaged for many instances of low mass proto-stars (McCaughrean & O'Dell, 1996), confirming the disc accretion scenario. However, the model for low mass stars can not simply be scaled up for O and B stars. A core that has accreted a mass of 10 $M_{\odot}$ will have already reached the ZAMS and has a high luminosity (Beech & Mitalas, 1994). This radiative presssure will rapidly halt infall from the surrounding dust cloud, unless the mass accretion rate is high enough to overcome the ram pressure (Stahler et al., 2000). Until recently, it was not certain whether stars greater than 10 $M_{\odot}$ could be formed in this manner. Yorke & Sonnhalter (2002) have simulated the collapse of slowly rotating, non-magnetic, massive molecular clumps. They found that even with radiative acceleration taken into account, it is possible for a massive star to form via a thick accretion disc, in a manner similar to low mass stars. The stellar energy is then carried away by powerful radiation-driven polar outflows. Thus an observational test of the accretion scenario would be to find massive bipolar outflows perpendicular to an accretion disc. Such a system appears to have been found in the high mass protostar candidate IRAS 20124+4104 (Cesaroni et al., 1997) and multiple outflows have been found in IRAS 05358+3543 (Beuther et al., 2002). Unfortunately, the high angular resolution required to directly image circumstellar discs in these distant star formation regions is not achievable with instruments currently available.

However, the tendency of newly born massive stars to be found in the central regions of dense clusters (Clarke et al., 2000) indicates that there is another mechanism by which high mass stars can be formed. The high density of protostellar cores would lead to gravitational interactions, some of which may lead to collisions and subsequent coalescence of the protostellar objects (Bonnell et al., 1998; Bonnell & Bate, 2002). This process can bypass the effects of radiative pressure and lead to the formation of extremely high mass stars. The high fraction of binaries and multiple systems in the Galaxy are certainly a good indicator that gravitational interactions are taking place (Abt, 1983).

These two theories of high mass star formation are not mutually exclusive. It is possible that both processes can be contributing to the formation of massive stars. At this stage, there is not sufficient information to determine which scenario is correct, or if both are present, which is dominant.

1.1.2 Evolutionary sequence

The proposed evolutionary sequence for massive star formation starts with dense clumps of radius $\sim$ 1 pc and mass $\sim 10^4 M_\odot$ (Hofner et al., 2000) forming within a giant molecular cloud. These clumps collapse to dense cores with diameters $\lesssim$ 0.1 pc, densities $\gtrsim 10^7$ cm^{-3} and temperatures $\gtrsim$ 100 K (Olmi et al., 1993; Kurtz et al., 2000). These hot cores can contain more than one massive star (Cesaroni et al., 1994). Ultracompact (UC) H II regions are formed at some point early in the evolution of the massive star. The UC H II regions will gradually lose their compactness due to increased pressure from heating and photo-dissociation, causing the surrounding gas and dust to expand (Wood & Churchwell, 1989b). The lifetimes of the different phases and the exact details of the transition from one phase to another are not precisely known at this stage.

1.2 Observational probes of high mass star formation

Radio continuum emission

Deeply embedded massive stars will produce ionized regions which are restricted in size by the surrounding molecular cloud. The more compact the region, the younger the star, since radiation pressure from the star will gradually cause the ionized region to expand. Searches for UC H II regions can help find embedded massive stars in an early evolutionary phase (Wood & Churchwell, 1989a). However, extremely young stars are unlikely to produce detectable H II regions (Walsh et al., 2002).

Infrared emission

The optical radiation from deeply embedded stars cannot pass directly through the surrounding molecular cloud. The emission is reprocessed towards longer wavelengths through successive absorption and re-emission by dust grains, until the edge of the cloud is finally reached. The dust cores have a spectral energy distribution that typically peaks around 100 μm and drops off rapidly towards shorter wavelengths (Chini et al., 1986; Churchwell et al., 1990), making the mid and far-infrared the best range in which to search for star formation cores. However, the dust cocoons of sources that are not very deeply embedded can be imaged in the near-infrared (Testi et al., 1998).

Directed searches of sources in the Infrared Astronomy Satellite (IRAS) Point Source Catalogue with the appropriate colours have been effective in locating regions of high mass star formation (Wood & Churchwell, 1989a). However, a significant fraction of high mass star formation candidates are not associated with an IRAS point source (Ellingsen et al., 1996). This may be due to the poor resolution of IRAS, which resulted in many point sources along the Galactic plane being omitted from the catalogue because of confusion. The Midcourse Space Experiment (MSX) catalogues offer a better chance of locating high mass star forming regions because of the better resolution but it is still not sufficient to resolve the individual sources in clusters. In addition, new developments in ground-based instrumentation in the mid-infrared are making it possible to detect individual cores towards sources with high optical depth (De Buizer et al., 2000; Persi et al., 2003).

The shock excited lines of Fe II, H_2 and the Brackett series of hydrogen transitions are of use in tracing shocks and outflows in these regions (Bachiller et al., 1994; De Buizer, 2003).

Sub-mm and mm emission

A number of transitions for molecules such as CO, CS, NH_3 (Langer et al., 2000, and references therein), as well as thermal dust emission, can be imaged in star formation regions using sub-mm arrays. These transitions have been extremely useful for mapping molecular outflows from hot cores (Shepherd & Churchwell, 1996; Cesaroni et al., 1997), but the resolution available is not sufficient to resolve the stars or any circumstellar discs at the centre of high-mass star formation cores. Spectroscopy of the molecular lines can also be used to determine the conditions in the star formation region, eg. composition of the cloud, density and temperature.

Masers in star formation regions

The primary species of masers seen towards star formation regions are water, hydroxyl (Forster & Caswell, 1999) and methanol (Menten, 2002).

Water masers are typically found in shock fronts, usually in outflows but also possibly in ionization shock fronts from stellar winds (Torrelles et al., 1997). However, water masers by themselves are not a sufficient indicator of high mass stars, since many instances of water masers have been found in outflows from lower mass stars (Furaya et al., 2003).

Hydroxyl masers appear to be closely related to water masers (Forster & Caswell, 1989). However, the maser species are not always spatially coinci-

dent, implying that they are not excited by the same conditions, but may well be associated with the same embedded source. The high rate of detection of hydroxyl masers towards UC H II regions in early observations appeared to indicate that hydroxyl masers were closely associated with UC H II regions. However, high angular resolution observations indicate that only about 50% of hydroxyl masers can be associated reliably with a detectable UC H II region (Forster & Caswell, 2000). The low detection rate of UC H II regions could be explained if hydroxyl masers are also associated with protostellar objects which are too young to have a detectable H II region. In addition, recent observations by Argon et al. (2003) indicate that there may be a class of hydroxyl masers closely associated with outflows and water masers, so there may be two classes of hydroxyl masers in star formation regions.

Methanol is a particularly rich molecule to study since it has literally hundreds of transitions, many of which are capable of masing (Menten et al., 1986a,b; Zeng & Lou, 1990; Cragg et al., 2001). The masers found in star formation regions have been divided into two classes by Batrla et al. (1987). Class I masers do not appear to be associated with compact infrared sources, H II regions, water masers or hydroxyl masers. On the other hand, Class II methanol masers appear to be situated close to hydroxyl masers (Caswell et al., 1995c) and UC H II regions (Walsh et al., 1998).

Two widespread and powerful class II methanol maser transitions are the 12.2 GHz $2_0 - 3_{-1}E$ and 6.7 GHz $5_1 - 6_0A^+$ lines. The two species of masers appear to be spatially coincident in many cases (Minier et al., 2001) and are believed to be excited by a common mechanism (Cragg et al., 2001). These masers are commonly believed to be closely associated with high mass protostars, but the exact location of the masers relative to the star is still unknown. High-resolution imaging has shown that some sources have maser spots in linear or arc-like structures with velocity gradients characteristic of Keplerian rotation (Norris et al., 1998), implying that the masers may be in circumstellar discs, but there are many sources which do not have such structure (Walsh et al., 1998). It is speculated that some sources may be associated with outflows or expanding H II regions (Minier et al., 2002a). To confuse the issue even further, a large number of masers have been found not to be associated with any of the usual signposts of high mass star formation (Ellingsen et al., 1996; van der Walt et al., 2003). This may imply that the methanol masers are also associated with lower mass stars ($M \lesssim 10$ $M_\odot$), or that they occur at such an early evolutionary stage that the protostar has not produced a detectable H II region. A recent survey by Minier et al. (2003) suggests that 6.7 GHz methanol masers are at least not associated with low mass objects ($M \lesssim 3$ $M_\odot$). Thus the methanol masers may be the best probes of the earliest stages of high mass star formation.

1.3 Thesis outline

There have been more than 500 6.7 GHz methanol maser sources detected since the intial discovery by Menten (1991) of this powerful maser line (eg surveys by Gaylard & MacLeod, 1993; Ellingsen et al., 1996; Caswell, 1996; van der Walt et al., 1996; Slysh et al., 1999, and references therein), giving a large database of high-mass star formation candidates. Water maser studies have enabled researchers to monitor outflows in star formation regions (Hunter et al., 1994). Can methanol masers likewise be used as a probe of the conditions around high mass protostars? The maser components are typically very small, of the order of a few tens of AU's across (Minier et al., 2002b), and can thus be used to probe changes in extremely small regions.

The 6.7 GHz methanol masers appear to display a significant level of variability (Caswell et al., 1995a), while the 12.2 GHz masers are not reported to be strongly variable except in isolated cases (MacLeod & Gaylard, 1993; Moscadelli & Catarzi, 1996).

The 6.7 and 12.2 GHz masers appear to display a significant level of variability (MacLeod & Gaylard, 1993; Caswell et al., 1995a; Moscadelli & Catarzi, 1996). Caswell et al. (1995a) report that the percentage changes at 12.2 GHz are, in general, significantly larger than at 6.7 GHz, which they interpret as possibly indicating a lower level of saturation in the 12.2 GHz transition. Observations of G351.78-0.54 at 6.7 GHz show rapid, high amplitude variations on a time-scale of weeks when the maser is in an active phase (MacLeod & Gaylard, 1996). On the other hand, other masers appear to be unvarying over the same time-scales. How widespread is methanol maser variability, what are the characteristics of the variability, and how can this information be used to further our understanding of high mass star formation? For example, if masers undergo periodic variations, this could be construed as evidence of orbital motion around the (proto)star. Random variations could be used to assess the degree of turbulence in the region of the masers. Water masers entrained in outflows show changes in their peak velocity over several years (Liljeström et al., 1989; Brand et al., 2003). Can similar velocity drifts be detected in methanol masers? Such considerations could yield vital clues to the nature of the methanol masers, but regular monitoring of a large sample of masers had not been undertaken.

Since all of these issues cannot be dealt with in a single thesis, I will focus on a few aspects. The main portion of this thesis is devoted to monitoring a sample of 6.7 GHz methanol masers. But first, in chapter 2, I take a closer look at the near-infrared environment of the masers and examine the relation between the positions of the methanol masers and other signposts of star formation. In chapter 3 I give a summary of the methanol maser monitoring programme

and the general results. A particularly exciting result has been the discovery of a number of masers which undergo periodic variations. Chapter 4 gives a more detailed examination of these sources. One of the periodic sources was imaged during a flare using the VLBA at 12.2 GHz and this work is presented in chapter 5. The summary of results and a discussion of future work is given in chapter 6.

Chapter 2

Near-infrared imaging

The following chapter is based on a paper by Goedhart et al. (2002)

2.1 Introduction

Although other workers have imaged massive star formation regions, the emphasis has not been on methanol masers. However, some of the water maser sources imaged by Testi et al. (1994, 1998) have 6.7-GHz methanol maser sources associated with them. Osterloh et al. (1997) imaged 31 cold southern *IRAS* sources at H and K′. None of those studies considered the position of methanol masers relative to near-infrared (NIR) objects in each region. Walsh et al. (1999) imaged 25 methanol maser sources at J, H, K and L bands with a limiting magnitude of 14 at all bands under conditions that may not have been photometric. Their astrometry had uncertainties ranging from 2 to 4 ″.

In this chapter, NIR images of the regions surrounding twelve 6.7 GHz methanol maser sites are presented. These sources were selected from the list of methanol masers being monitored for variability at the Hartebeesthoek Radio Astronomy Observatory. Seven of the sources presented here are not known to have been imaged previously at NIR wavelengths. The large field of view used enables astrometry accurate to 0.5″ and gives an indication of whether the field around the methanol masers differs from other areas. The aim is to find out whether any NIR sources can be associated with the methanol masers, as well as to see if there is anything unusual about the region in which the masers are being produced. The relation of the methanol masers to NIR objects, H II regions and other maser species is examined.

The details of the observations and reductions will be given in Section 2. In

Table 2.1: Central wavelengths of filters

filter	I	J	H	K
λ (μm)	0.90	1.22	1.65	2.18

Section 3 the results are presented. The sources are discussed in detail in Section 4 and the findings are discussed in Section 5. The summary is presented in Section 6.

2.2 Observations and data reduction

The observations were made using the OSIRIS camera on the 1.5 m telescope at Cerro Tololo Inter-American Observatory on the nights of 1999 July 29 to August 1. The camera used a 1024x1024 HgCdTe detector with a plate scale of 0.46″/pixel and a central illuminated area corresponding to 266″ at a focus of f/13.5.

Images were made at I, J, H and K bands. Table 2.1 gives the wavelengths of the filters. Eight co-adds of three seconds each were used for each exposure. The shortest possible exposure time for the co-adds was selected to try to avoid saturating the detector. Four dithered images each were taken at I, J and H bands and eight images were made at K band for each object. In cases where the fields were difficult to identify, additional images at I band were taken with the telescope centred on nearby bright stars – normally HST guide stars – in such a way that there was overlap with the on-source image. Standard stars from the list of faint standards of Persson et al. (1998) were observed at regular intervals. The detection limits at J, H and K were found to be a maximum of 16^{th} magnitude. However, as will be shown later, the sensitivity limit may have varied in individual fields. In some images the faintest object detected at H or K band was 14.5 magnitudes.

The data reductions were done using IRAF. The detector being used on OSIRIS at that time had a bias discontinuity across the quadrants of the detector which could not be subtracted completely using the overscan area, or removed using dome flats. The bias appeared to vary slowly with time. To address this, sky fields were constructed by median averaging the standard star fields observed before and after the programme field. The field which cleanly subtracted the bias was then adopted as the sky field. The averaged sky fields for the night were used to make a flat field. This resulted in a very clean image with most of the bias removed. The final composite images were made using the SQMOS and NIRCOMBINE tasks in the NOAO SQIID package.

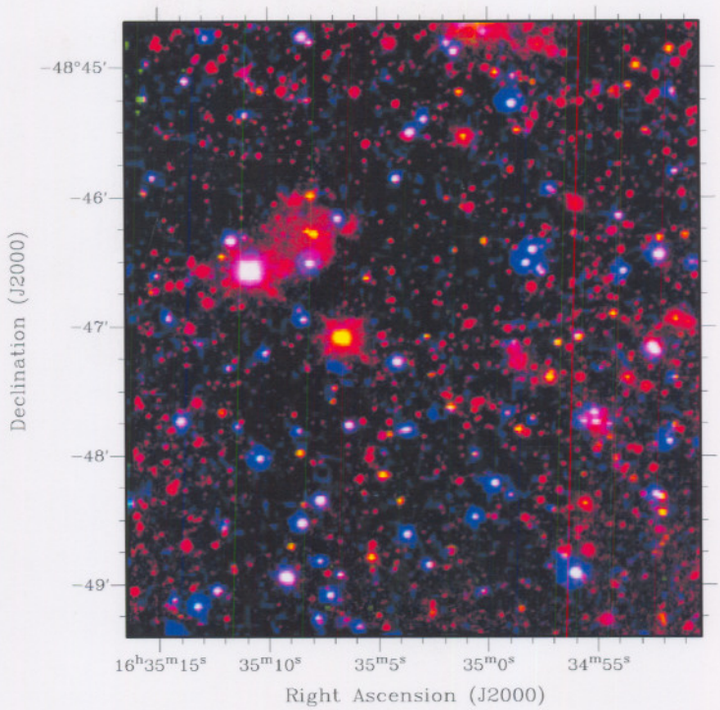

Figure 2.1: Three-colour composite image showing overlap between optical and infrared sources for G336.01–0.82. The blue frame is the Digitized Sky Survey field, the green frame is the I band image and the red frame is the K band image.

The solution of the image world coordinate system was found using images from the Digitized Sky Survey (DSS) as reference fields. The I band images were invaluable in identifying NIR counterparts to some of the faint optical stars. In every case, it was possible to find stars visible in all bands and register the images directly to the DSS image, which ensured that no cumulative errors occurred from finding solutions in a stepwise manner. Figure 2.1 shows the overlap in sources at V, I and K bands for a typical field. Due to the crowded nature of the infrared fields in the vicinity of the methanol masers, an accurate coordinate transform was vital for comparing the NIR environment to the methanol maser positions. Typically, at least 15 reference stars spaced around the entire field were used to obtain the coordinate transform. The rms error of the WCS solution was of the order of $0.5''$ to $0.7''$. This level of positional uncertainty is of the same order as the absolute positional uncertainty of the methanol maser spots, so it is possible to compare maser positions and NIR objects in a meaningful manner at this level, unless there are multiple stars less than $0.5''$ from each other.

The IRAF DAOPHOT package was used to obtain photometry of the sources.

Table 2.2: J, H and K band magnitudes and flux densities of infrared objects close to the methanol maser positions

#	Methanol source	RA (J2000)	Dec (J2000)	J Mag.	F_J mJy	H Mag.	F_H mJy	K Mag.	F_K mJy
1	G10.33–0.17 B	18 09 01.632	–20 05 07.25	–	–	–	–	10.93	28.14
2	G10.33–0.17 C	18 08 55.723	–20 05 57.37	–	–	12.76	8.46	11.26	20.76
3	G12.91–0.26	18 14 39.595	–17 52 01.38	14.58	2.67	12.55	10.29	8.79	202.00
4	G45.07+0.13 #1	19 13 22.089	10 50 55.59	–	–	–	–	10.10	60.43
5	G45.07+0.13 #2	19 13 21.876	10 50 50.36	–	–	–	–	10.52	41.04
6	G52.67–1.09 #1	19 32 36.091	16 57 40.02	–	–	13.24	5.44	10.83	30.85
7	G52.67–1.09 #2	19 32 36.182	16 57 32.30	–	–	15.15	0.94	12.70	5.51
8	G328.81+0.63	15 55 48.571	–52 43 11.46	–	–	–	–	10.91	28.66
9	G337.92–0.46	16 41 06.111	–47 06 58.29	–	–	12.60	9.82	10.71	34.45
10	G339.62–0.12	16 46 06.101	–45 36 41.58	–	–	12.18	14.46	9.67	89.79
11	G351.78–0.54	17 26 42.910	–36 09 13.39	–	–	–	–	11.17	22.56

It was found that some of the K band sources near methanol masers were not point sources i.e. their profile did not match that of the point spread function found using field stars on the same image. Therefore fluxes obtained using DAOPHOT and the point spread function may be underestimated. It was decided to estimate the fluxes of these sources using simple aperture photometry techniques instead.

2.3 Results

The general trend observed here is for the environment of the methanol masers to be very crowded. This is not surprising since it is well known that massive stars tend to form in clusters. These sources are situated along the Galactic plane, hence there are many unrelated stars adding to the crowded fields. At this time, observational evidence suggests that the methanol masers trace objects in a very early evolutionary phase (Walsh et al., 1999; Minier et al., 2001), therefore we may expect that the sources will be deeply embedded and highly reddened as a result. Deeply embedded sources would have steep spectral energy distributions (SEDs) decreasing towards shorter wavelengths (Goedhart et al., 2000). If the optical depth of the cloud is high, the embedded source may only be detectable at K band, if all. By contrast, main sequence stars would have a SED that decreases toward longer wavelengths and would therefore appear bluer than an embedded star. Visual examination of the distribution of stars with different colours in the field around the methanol masers shows that stars with blue colours or slightly reddened main-sequence stars are distributed fairly uniformly over the image. This suggests that these are foreground stars and stars that are reddened by normal interstellar extinction. These stars can therefore be safely disregarded in the following analysis.

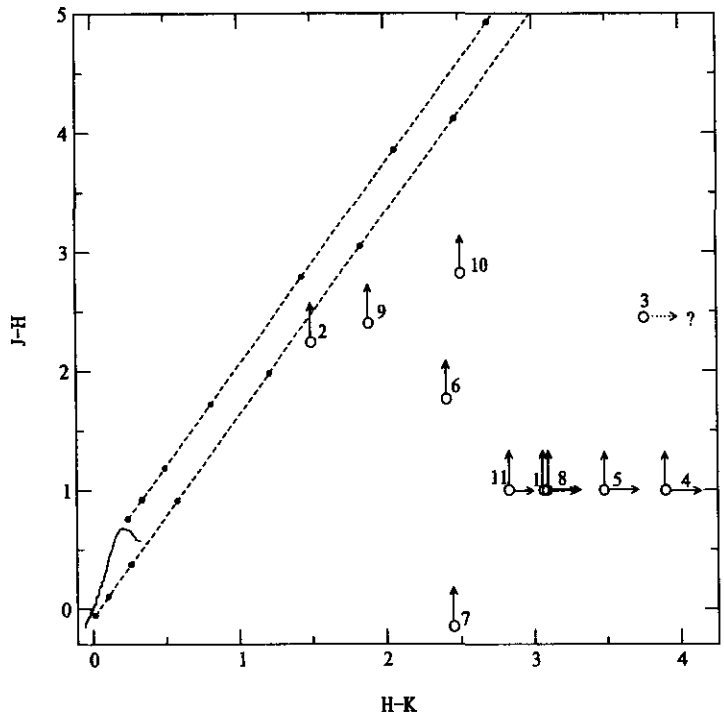

Figure 2.2: H-K vs J-K diagram of the stars possibly associated with methanol masers. The solid line shows the colours of the unreddened main-sequence stars. The dashed lines indicate the reddening band, within which reddened main-sequence stars should lie. Filled circles are placed at intervals of one magnitude of extinction along the reddening vectors. The open circles are enumerated according to the source numbers given in Table 2. The arrows indicate that the colours plotted are lower limits. Objects 1, 4, 5, 8 and 11 have a K band magnitude alone. Upper limits of 16 magnitudes at J and 15 magnitudes at H are assumed. Object 3 may have been saturated at K band.

The positions, magnitudes and flux densities[1] of objects likely to be deeply embedded sources, within 10″ of the methanol masers, are listed in Table 2.2. Figure 2.2 shows the position of these sources on a J-H vs H-K two-colour diagram. The only source visible at all three bands is G12.91–0.26, which has an infrared excess. Such an infrared excess can be expected from sources surrounded by hot dust. It is not possible to tell whether the other sources are simply deeply embedded or whether they have an infrared excess since J magnitudes are not available. The majority of these sources have H-K > 1.5. Assuming that the sources do not have an infrared excess, this implies that the extinction due to dust is greater than five magnitudes. In the more extreme cases where H-K > 3 the extinction would be greater than seven magnitudes.

[1]A description of the method used to obtain the zero points for the LCO system is given in Appendix A.

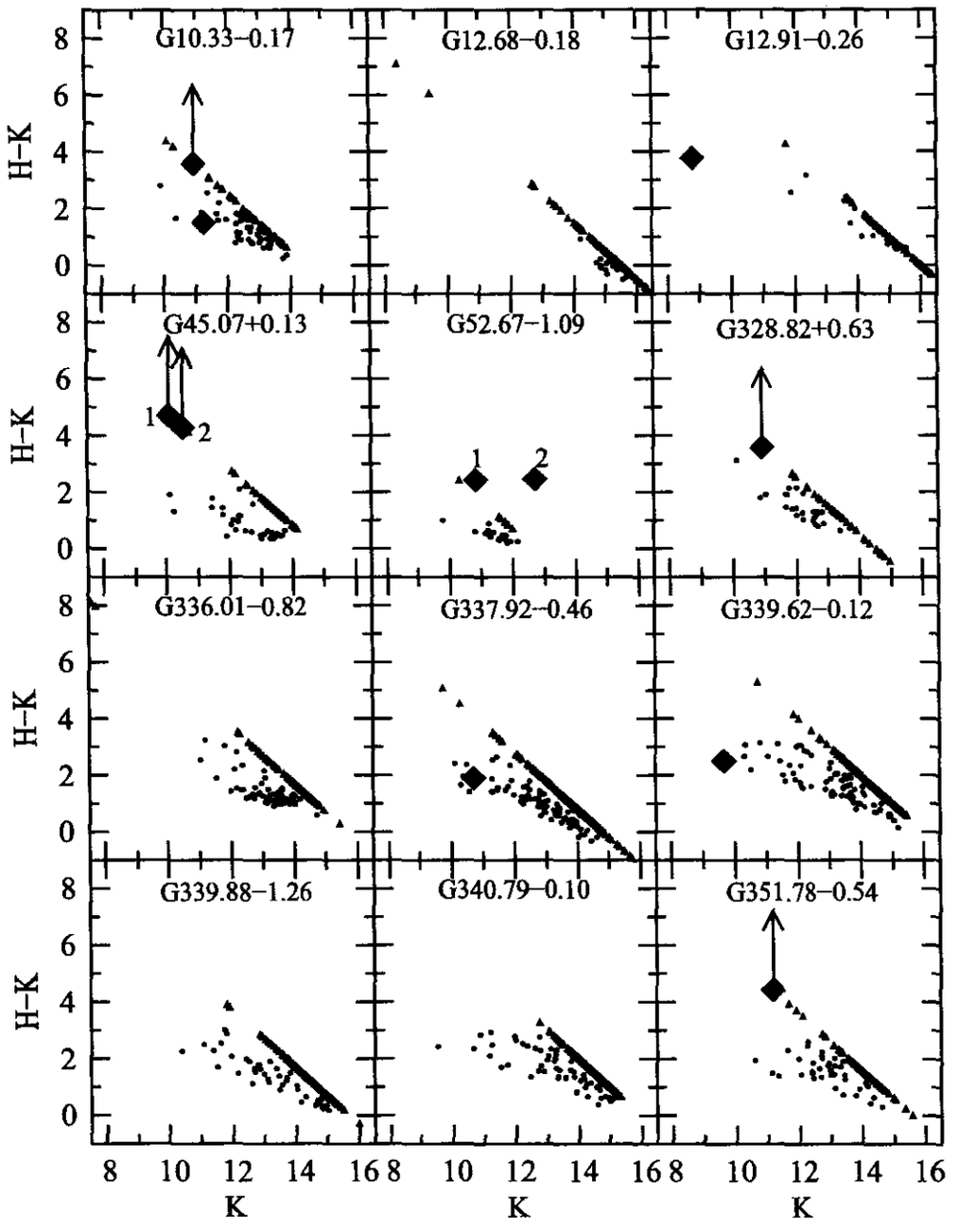

Figure 2.3: K vs H-K diagram showing sources in all the fields imaged. Only sources detectable at H and K only (filled circles) or K only (filled triangles) are shown. The sources possibly associated with methanol masers are indicated by filled diamonds. The filled triangles and diamonds with arrows indicate that the value plotted is a lower limit for the H-K colour.

How common are such sources in the fields imaged? Figure 2.3 shows plots of the K magnitude against H-K colour in each field imaged for all sources visible at H and K bands only. A two-colour diagram was not used because it was found that the observed colours of some very bright sources placed these stars above the reddening band in a J-H vs H-K diagram. Such colours are unrealistic (Lada & Adams, 1992), indicating a possible observational problem. Investigation found that these sources were typically very bright and showed evidence of "blooming". This problem was not found for fainter sources visible only at H and K bands. In order to exclude sources with such saturation effects when examining the entire field, K vs H-K diagrams for sources which were only detected at H and K bands are used. This does not significantly affect our analysis since the majority of the saturated stars belong to the group which has been excluded, as discussed above. It can be seen that the sources listed in Table 2.2 are typically among the brightest of the K band sources. This makes it less probable that these objects are just associated with the methanol maser by chance. The sources with measurable H-K colours appear to fall below a line on the diagram which defines the limiting magnitude at H. The limiting magnitudes for each image were determined by inspection and ranged from 14.5 to 16. They did not appear to be dependent on airmass. It is possibly an effect of the time variable bias mentioned earlier.

Three-colour composite images[2] are presented in Figures 2.4 to 2.15. The blue frames are from J band, the green frames are H band and the red ones are K band. Although only the area immediately around the masers is discussed in detail in this paper, the full 266″ fields are presented since they may be of use as finding charts to other workers. Examination of the large field also gives an indication of the stellar environment, eg the probability of confusion in the area around the maser source can be determined. Enlarged images of the area of interest around each methanol maser group are also presented. The position of known H II regions (○), water masers (∗), 6.7 GHz methanol masers (+) and hydroxyl masers (×) are marked on the images. The ellipses show the IRAS error box in the cases where there is an IRAS point source in the field of view. The white contours are the Midcourse Space Experiment (MSX) A-band (8 μm) intensities (Price et al., 2001). The MSX survey has a spatial resolution of 18″.

Table 2.3 lists the positions of the observed radio emitters and the reference to the paper reporting the most accurate position. Where multiple maser spots are present, the centroid position for each group is tabulated. Kinematic distances for the maser sources are calculated using the Galactic rotation curve derived from Wouterloot & Brand (1989) and are given in Table 2.4. Table 2.5 gives the separations between the other objects in the field and the methanol masers, using the near kinematic distance. In the following sections the area

[2]The RGB images and contour overlays were produced using the KARMA package (Gooch, 1996).

Table 2.3: Positions of radio sources and references. Single dish observations are marked with an *. The centroid position is given in cases where multiple maser spot positions were mapped. Key to references: 1. Becker et al. (1994); 2. Griffith et al. (1994); 3. Kuchar & Clark (1997); 4. Fürst et al. (1990); 5. Brand et al. (1994); 6. Walsh et al. (1998); 7. Lada et al. (1981); 8. Caswell et al. (1995b); 9. Forster & Caswell (1989); 10. Bieging et al. (1978); 11. Phillips C.J., private communication; 12. Hofner & Churchwell (1996); 13. Testi et al. (1999); 14. van der Walt et al. (1996); 15. Palumbo et al. (1994); 16. Caswell (1998); 17. Wright et al. (1994); 18. Scalise & Braz (1980); 19. Batchelor et al. (1980); 20. Ellingsen et al. (1996); 21. Phillips et al. (1998); 22. Argon et al. (2000); 23. Norris et al. (1993); 24. Hughes & MacLeod (1993);

Name	Type of source	RA (J2000)	Dec (J2000)	Pos. unc. $''$	Freq. GHz	Ref.
G10.33–0.17	H II region	18 09 01.419	–20 04 30.64	2	5	1
	H II region	18 09 00.323	–20 05 08.42	2	5	1
	H II region	18 08 55.900	–20 05 54.94	2	5	1
	H II region	18 08 58.699	–20 05 21.98	8	4.85	2
	H II region	18 08 58.315	–20 05 15.27	< 20	4.85	3
	H II region	18 08 59.000	–20 05 45.00	10*	2.7	4
	Water maser	18 08 55.927	–20 05 53.45	20*	22	5
	Methanol maser C	18 08 55.545	–20 05 57.96	1	6.7	6
	Methanol maser A	18 08 59.988	–20 03 35.56	1	6.7	6
	Methanol maser B	18 09 01.453	–20 05 08.00	1	6.7	6
G12.68–0.18	Water maser	18 13 54.754	–18 01 46.49	0.2	22	7
	Methanol maser	18 13 55.110	–18 01 34.56	10*	6.7	8
	Hydroxyl maser	18 13 54.871	–18 01 45.16	0.5	1.665	9
	H II region	18 13 56.900	–18 00 47.00	10*	8.6	10
G12.91–0.26	Methanol maser	18 13 54.754	–18 01 41.41	1	6.7	6
	Water maser	18 14 39.490	–17 51 59.95	1	22	9
	Hydroxyl maser	18 14 40.250	–17 52 00.07	1	1.665	9
	H II region	18 14 28.920	–17 53 08.10	10*	8.6	10
G45.07+0.13	Methanol maser	19 13 22.130	+10 50 53.92	1	6.7	11
	Water maser	19 13 22.102	+10 50 53.09	<1	22	12
	Hydroxyl maser	19 13 22.034	+10 50 53.81	1	1.665	9
	UC H II region	19 13 21.869	+10 50 48.98	<1	4.9/8.5	13
	UC H II region	19 13 22.080	+10 50 53.20	<1	4.9/8.5	13
G52.67–1.09	Methanol maser	19 32 35.280	+16 57 33.37	60*	6.7	14
	Water maser	19 32 31.670	+16 57 33.20	10*	22	5
G328.81+0.63	Methanol maser	15 55 48.432	–52 43 06.11	1	6.7	6
	Hydroxyl maser	15 55 48.550	–52 43 05.59	1	1.665 /1.667	16
	H II region	15 55 48.600	–52 43 08.00	6	4.85	17
G336.01–0.82	Methanol maser	16 35 09.299	–48 46 47.00	1	6.7	6
	Hydroxyl maser	16 35 09.350	–48 46 47.10	1	1.665 /1.667	16
	H II region	16 35 05.299	–48 46 12.00	6	4.85	17
G337.91–0.46	Methanol maser	16 41 06.052	–47 07 01.98	1	6.7	6
	Hydroxyl maser	16 41 10.430	–47 08 03.08	1	1.665 /1.667	16
	Hydroxyl maser	16 41 06.701	–47 07 02.39	1	1.665 /1.667	16
	Water maser	16 41 08.642	–47 07 55.78	20*	22	18
	H II region	16 41 10.601	–47 07 14.99	6	4.85	17
G339.62–0.12	Methanol maser	16 46 05.978	–45 36 43.43	1	6.7	6
	Hydroxyl maser	16 46 06.031	–45 36 43.70	1	1.665 /1.667	16
	Water maser	16 46 06.866	–45 36 58.18	10*	22	19
G339.88–1.26	Methanol maser	16 52 04.653	–46 08 33.50	1	6.7	6
	Hydroxyl maser	16 52 04.713	–46 08 30.69	1	1.665	9
	Water maser	16 52 04.637	–46 08 35.16	1	22	9
	UC H II region	16 52 01.682	–46 08 34.40	1	8.5	20
G340.79–0.10	Methanol maser	16 50 14.823	–44 42 26.82	1	6.7	21
	Hydroxyl maser	16 50 14.846	–44 42 22.93	1	1.665 /1.667	16
	UC H II region	16 50 14.784	–44 42 21.28	7	8.4	22
G351.78–0.54	Methanol maser	17 26 42.677	–36 09 17.78	1	6.7	23
	Hydroxyl maser	17 26 42.516	–36 09 18.22	1	1.665 /1.667	16
	Water maser	17 26 42.329	–36 09 16.38	1	22	9
	UC H II region	17 26 43.459	–36 09 15.80	1	8.64	6
	UC H II region	17 26 42.500	–36 09 17.00	<1	5	23
	UC H II region	17 26 42.460	–36 09 17.60	<1	5	24

Table 2.4: Kinematic distances to methanol maser sources. Molecular line velocities are not available for sources marked with an *. In these cases the maser velocity is used. Otherwise the velocities used are the CS(2–1) line velocities (Bronfman et al., 1996).

Object	Adopted velocity $km.s^{-1}$	Near distance kpc	Far distance kpc
G10.33–0.17	13.1	2.2	14.5
G12.68–0.18*	55.5	4.9	11.6
G12.91–0.26	36.6	3.9	12.6
G45.07+0.13	59.0	5.1	6.9
G52.67–1.09	59.7	5.1	5.2
G328.81+0.63	–42.3	3.0	11.5
G336.01–0.82	–48.3	3.6	12.0
G337.92–0.46*	–38.5	3.1	12.6
G339.62–0.12	–33.2	2.9	13.0
G339.88–1.26*	–31.6	2.8	13.1
G340.79–0.10*	–105.0	6.0	10.1
G351.78–0.54	–3.4	0.9	16.0

around each methanol maser site is examined in detail.

Table 2.5: Distances between methanol masers and other objects in the fields. The methanol maser identity is listed in column 1. The angular separation between field objects and the methanol maser and its uncertainty, are given in columns 3 and 4. In columns 5 and 6 the projected separation and uncertainty based on the near kinematic distances of the methanol masers are given.

Methanol maser	Object	A. sep $''$	σ $''$	P. sep kAU	σ kAU
G10.33–0.17 A	H II region	59	2	129	4
	H II region	93	2	204	4
	H II region	151	2	332	4
	H II region	102	8	225	18
	H II region	132	20	290	44
	H II region	130	10	286	22
	Water maser	149	20	328	44
	K band A	4	1	10	2
	K band B	94	1	208	2
	K band C	154	1	339	2
	G10.33–0.17 B	95	1	208	2
	G10.33–0.17 C	155	1	342	2
G10.33–0.17 B	H II region	37	2	82	4
	H II region	16	2	35	4

continued on next page

Distances between methanol masers and other objects in the fields.

continued from previous page

Methanol maser	Object	A. sep ″	σ ″	P. sep kAU	σ kAU
	H II region	91	2	201	4
	H II region	45	8	99	18
	H II region	79	20	174	44
	H II region	51	10	111	22
	Water maser	90	20	198	44
	K band A	98	1	216	2
	K band B	3	1	6	2
	K band C	95	1	208	2
	G10.33–0.17 A	95	1	208	2
	G10.33–0.17 C	97	1	214	2
G10.33–0.17 C	H II region	120	2	265	4
	H II region	84	2	184	4
	H II region	6	2	13	4
	H II region	58	8	127	18
	H II region	24	20	52	44
	H II region	50	10	111	22
	Water maser	7	20	15	44
	K band A	160	1	352	2
	K band B	100	1	219	2
	K band C	3	1	6	2
	G10.33–0.17 A	155	1	342	2
	G10.33–0.17 B	97	1	214	2
G12.68–0.18	Water maser	13	10	53	49
	Hydroxyl maser	38	10	188	49
	H II region	51	10	240	49
G12.91–0.26	Hydroxyl maser	10	1	40	4
	Water maser	1	1	2	4
	H II region	69	10	268	39
	K band object	2	1	6	4
G45.07+0.13	Water maser	1	1	5	5
	Hydroxyl maser	1	1	7	5
	H II region	1	1	5	5
	K band object	2	1	9	5
	K band object	5	1	26	5
G52.67–1.09	Water maser	52	60	264	306
	K band object	13	60	68	306
	K band object	13	60	66	306
G328.81+0.63	H II region	2	6	7	18
	Hydroxyl maser	1	1	4	3
	K band object	5	1	16	3

continued on next page

Distances between methanol masers and other objects in the fields.

continued from previous page

Methanol maser	Object	A. sep ″	σ ″	P. sep kAU	σ kAU
G336.01–0.82	Hydroxyl maser	1	1	2	4
	H II region	53	6	190	22
	K band object	0.5	1	2	4
G337.92–0.46	Hydroxyl maser	7	1	22	3
	H II region	48	6	149	19
	Water maser	60	20	186	62
	K band object	4	1	12	3
G339.62–0.12	Water maser	17	20	51	58
	Hydroxyl maser	1	1	2	3
	K band object	2	1	7	3
G339.88–1.26	Hydroxyl maser	3	1	8	3
	Water maser	2	1	5	3
	H II region	2	1	5	3
	K band object	2	1	6	3
G340.79–0.10	H II region	6	1	33	24
	Hydroxyl maser	4	1	23	6
G351.78–0.54	Hydroxyl maser	2	1	2	1
	Water maser	4	1	4	1
	H II region	10	1	9	1
	K band object	5	1	5	1
	H II region	2	1	2	1
	H II region	3	1	2	1

2.4 Notes on individual sources

2.4.1 G10.33–0.17

In this field, four separate groups of maser spots occur (Figure 2.4). Unfortunately one of the groups lies just outside the camera's field of view due to a small drift in the telescope centring. Although the spot groups have similar velocities, they have a significant spatial separation ($\sim$ 100″, see Table 2.5). Using a kinematic distance of 2.2 kpc, the greatest separation (projected on the plane of the sky) between the maser sites is of the order of 1.5 pc. This implies that the different spot groups are being powered by different embedded stars, but they probably belong to the same molecular cloud. The MSX images show an arc of emission, with unresolved sources visible at two of the three

GHz methanol masers with + and hydroxyl masers with ×. b. Area around methanol maser G10.33-0.17 A. c. Area around methanol maser G10.33-0.17 B. c. Area around water maser, methanol maser G10.33-0.17 C and H II region.

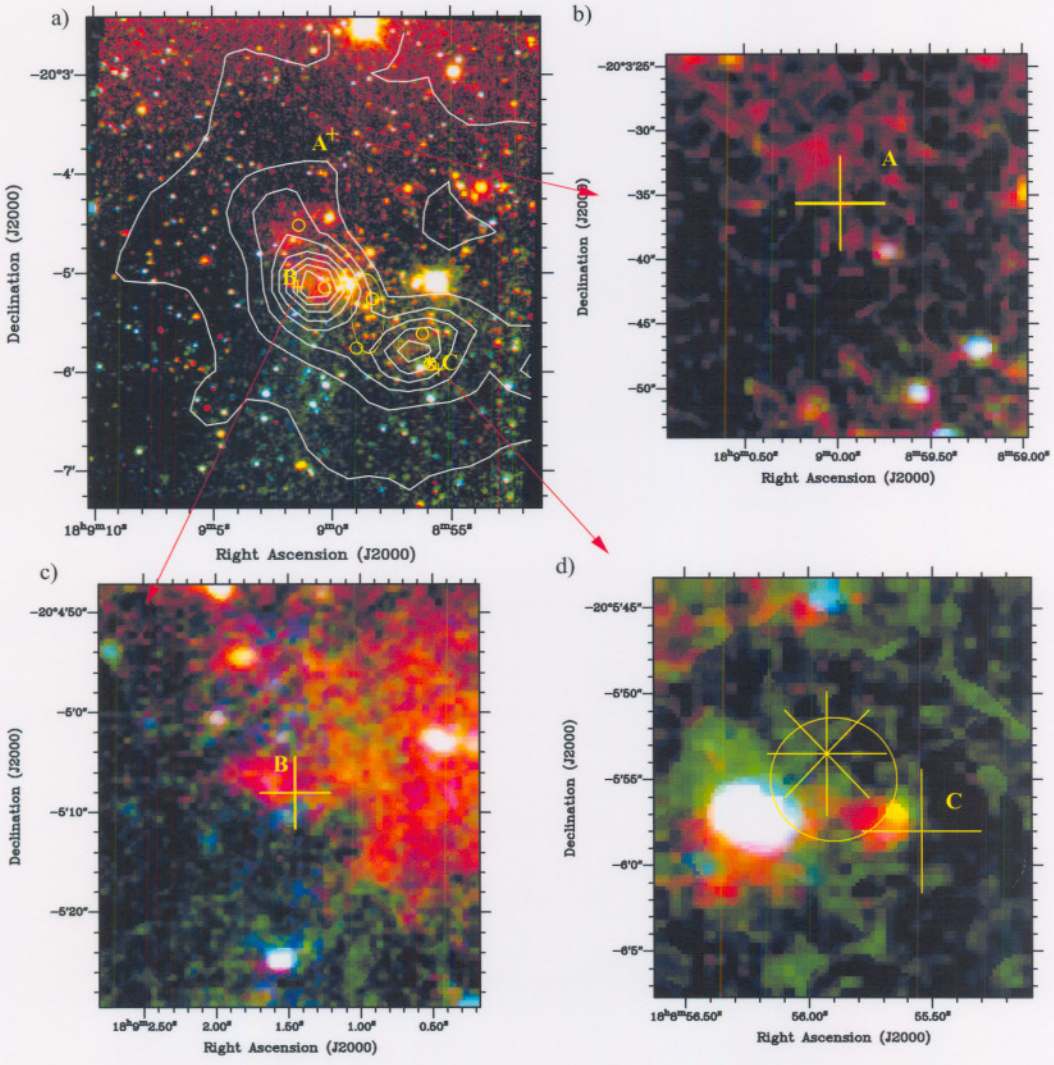

Figure 2.4: a. Three-colour composite image of the full field around G10.33-0.17. The known H II regions are marked with ○, water masers with ∗, 6.7 GHz methanol masers with + and hydroxyl masers with ×. b. Area around methanol maser G10.33-0.17 A. c. Area around methanol maser G10.33-0.17 B. c. Area around water maser, methanol maser G10.33-0.17 C and H II region.

maser sites. A sensitive survey at 8.4 GHz by van der Walt et al. (2003) shows the same arc of emission, which they speculate may be part of an expanding shell from an evolved H II region in the area.

The maser site in the northern part of the field (referred to as G10.33–0.17 A, Figure 2.4b) is in a dark region of the cloud. There are no bright K-band objects, H II regions or other maser species in this area. There is very faint diffuse emission at K-band 4″ to the north of the methanol maser position. This object is too faint to get a reliable magnitude estimate. There is no point source visible in the MSX images although the diffuse emission at A band does extend to this site.

The central group of maser spots (G10.33–0.17 B, Figure 2.4c) appears to lie near an embedded cluster with stars in different evolutionary stages. The maser cluster is 3″ east of a bright, extended K-band object. Examination of the K vs H-K diagram shows that this object is much brighter than most of the other K-band objects in the field. There is diffuse K band emission in this area. An MSX point source appears to be centred on this cluster.

A reddened object lies 2″ east of the maser group in the south of the field (G10.33–0.17 C, Figure 2.4d). This source appears to be brighter at K band than most other sources in the field with the same H-K colour.

None of the maser spots lie within the IRAS error ellipse (IRAS 18060–2005). Since IRAS has an inferior resolution to that of the MSX satellite, the position reported in the IRAS PSC is probably the average position of the two MIR sources resolved by MSX.

2.4.2 G12.68–0.18 (W33B)

This field does not show much activity in the near-infrared (Figure 2.5). There are no apparent NIR sources that could be associated with the methanol maser – the nearest reddened sources are 13″ away from the maser position. Although there is no diffuse K band emission in this field, there are an unusual number of K band objects visible, indicating a possible cluster of embedded stars. There are water masers 13″ away from the methanol maser position. A line of hydroxyl masers 38″ away are presumably too distant to be excited by the same star as the methanol masers. While no IRAS point source is reported here, there is an MSX point source centred on the area between the masers. Haschick & Ho (1983) suggested that the W33 complex consists of successive waves of massive star formation. They found extended radio emission across the entire complex, while Bieging et al. (1978) found several compact H II regions clustered within 1 pc of each other.

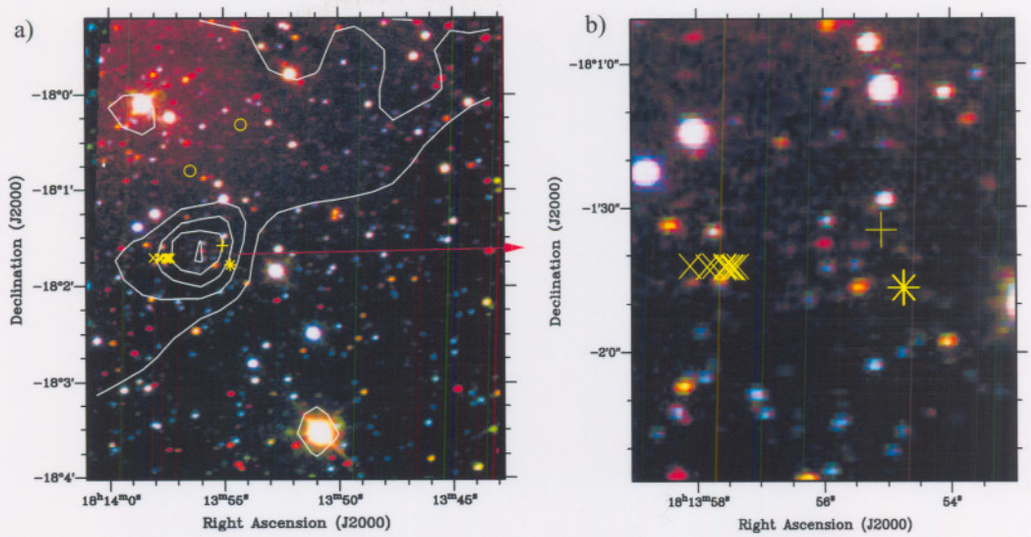

Figure 2.5: a. Three-colour composite image of the full field around G12.68-0.18. The known H II regions are marked with ∘, water masers with ∗, 6.7 GHz methanol masers with + and hydroxyl masers with ×. b. Area around methanol maser

2.4.3 G12.91–0.26 (W33A)

All the objects of interest are centred around one NIR source which is visible at J, H and K bands (Figure 2.6). This source does not conform to the point spread function calculated for the field. Compared to the H-K colour and K magnitude of other sources in this field, this source is very unusual, being the brightest object at K band and having H-K = 3.8. Since it is so bright, it is necessary to consider whether the saturation problem found with other bright stars is affecting the results. The J and H band magnitudes are too low for there to have been a saturation problem but the K band magnitude may have been affected. If the K band flux is greater, this will move the source further to the left in the K vs H-K diagram. Therefore, even if there are saturation effects, the source is different from others in the field.

The methanol maser position falls within the error ellipse of IRAS 18117–1753. The MSX images show a point source centred on the methanol maser position. The water and some of the hydroxyl masers coincide with the methanol maser position. The masers are in a region of the cloud with extended K-band emission. It is not clear whether this emission is solely due to continuum dust emission since there are only very faint traces of the nebulosity in the H band image and none in the J band image. The emission is elongated and there are two smaller arcs on either side, suggestive of bow shocks. Imaging this area in the shocked molecular hydrogen and Brγ emission bands could determine whether shocks are present. Careful examination of the area at H band shows

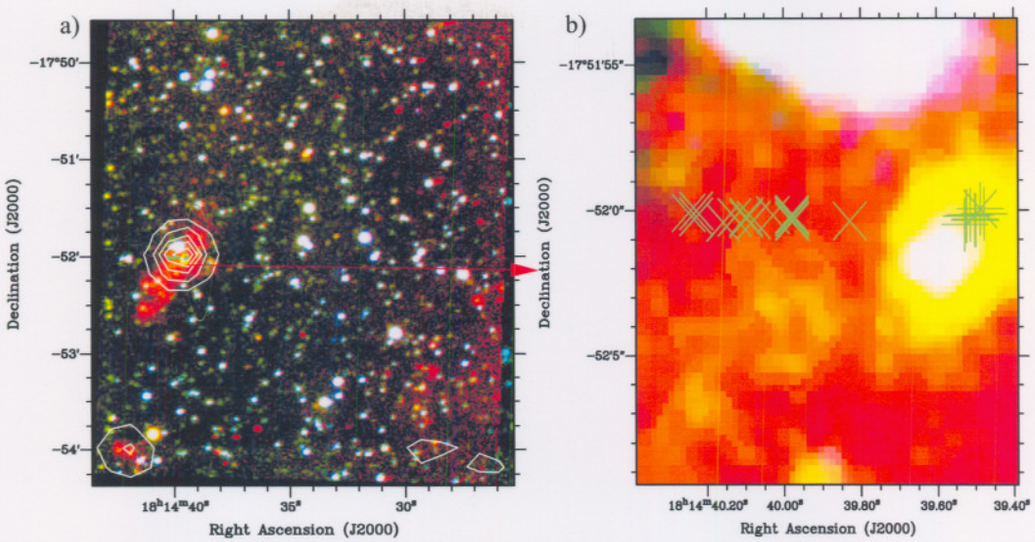

Figure 2.6: a. Three-colour composite image of the full field around G12.91-0.26. The known H II regions are marked with ∘, water masers with ∗, 6.7 GHz methanol masers with + and hydroxyl masers with ×. b. Area around methanol maser

the presence of other sources in this region. There would appear to be an embedded cluster here, which is consistent with the views of Haschick & Ho (1983) as discussed in the section above.

2.4.4 G45.07+0.13

The UC H II region, water masers, hydroxyl masers and methanol maser (position given by Chris Phillips, priv. comm.) are clustered on an extended, bright K-band source, which is located in the centre of the error ellipse of IRAS 19110+1045 (Figure 2.7). An MSX point source is visible at this position. This source is also known to have a face-on bipolar outflow centred in the H II region (Hunter et al., 1997). The very strong K band emission may be due in part to shocked H_2 emission from the outflow.

Another faint K band object 10″ to the south-west (source #5 in Table 2.2) is coincident with a UC H II region (Testi et al., 1999) but has no masers associated with it. These two sources are the brightest K band objects in the field.

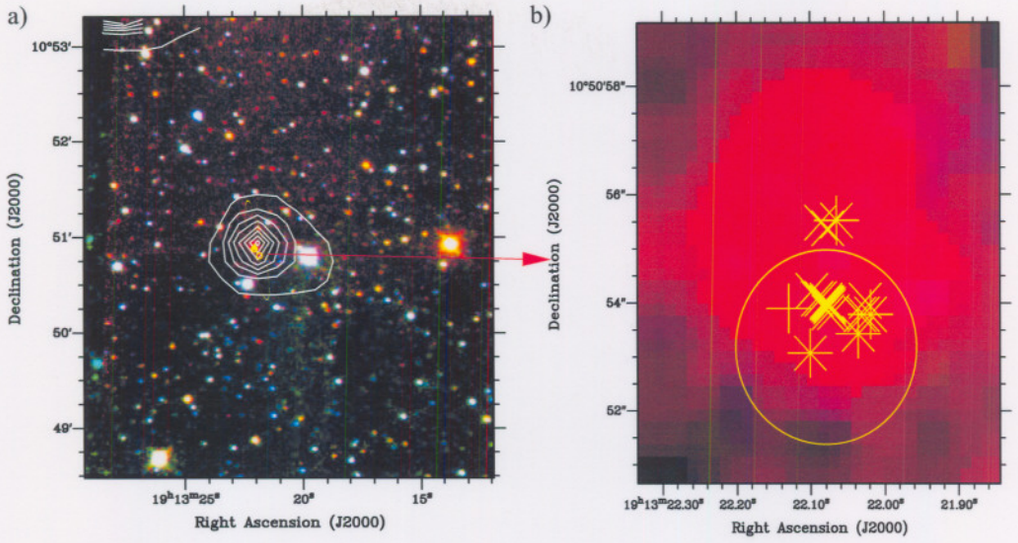

Figure 2.7: a. Three-colour composite image of the full field around G45.07+0.13. The known H II regions are marked with ○, water masers with ∗, 6.7 GHz methanol masers with + and hydroxyl masers with ×. b. Area around methanol maser

2.4.5 G52.67–1.09

The methanol maser position is poorly known since the source position has not been observed with an interferometer. An observation of the maser at Effelsberg (Walsh, priv. comm.) confirms that the position given is accurate to within 1′. At this level of accuracy, the methanol maser appears to be coincident with the IRAS point source position (IRAS 19303+1651, Figure 2.8). Observations of the water maser position using the Medicina telescope (Brand et al., 1994) indicate that the water maser is offset to the west of the IRAS position by less than half the Medicina beamwidth of 52″ (Brand, priv comm.). There are two very faint MSX A band sources visible on either side of the IRAS ellipse. There are two highly reddened NIR sources (labelled '1' and '2' in Figure 2.8b) 13″ from the maser position. They appear to have H-K colours very different from those of other sources with similar K magnitudes. However, until the maser positions are known with higher accuracy, it is not possible to identify potential NIR counterparts to the masers.

2.4.6 G328.81+0.63

This source has also been imaged at H and K′ by Osterloh et al. (1997). No water masers were detected in this area (Caswell & Haynes, 1983). A very bright NIR source is visible 5″ to the north of the methanol maser position

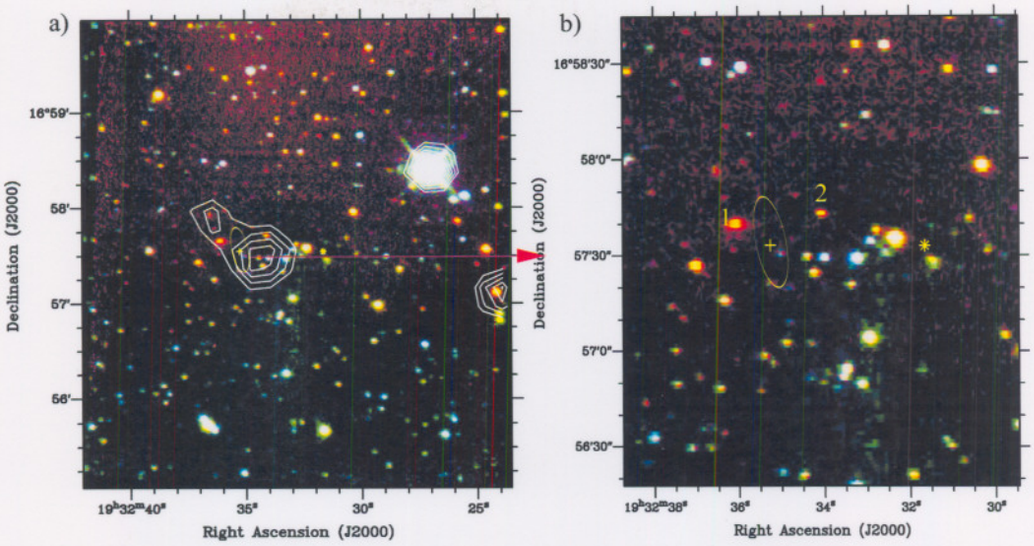

Figure 2.8: a. Three-colour composite image of the full field around G52.67-1.09. The known H II regions are marked with ○, water masers with ∗, 6.7 GHz methanol masers with + and hydroxyl masers with ×. b. Area around methanol maser. The yellow numerals indicate the sources for which photometry is given in Table 2.

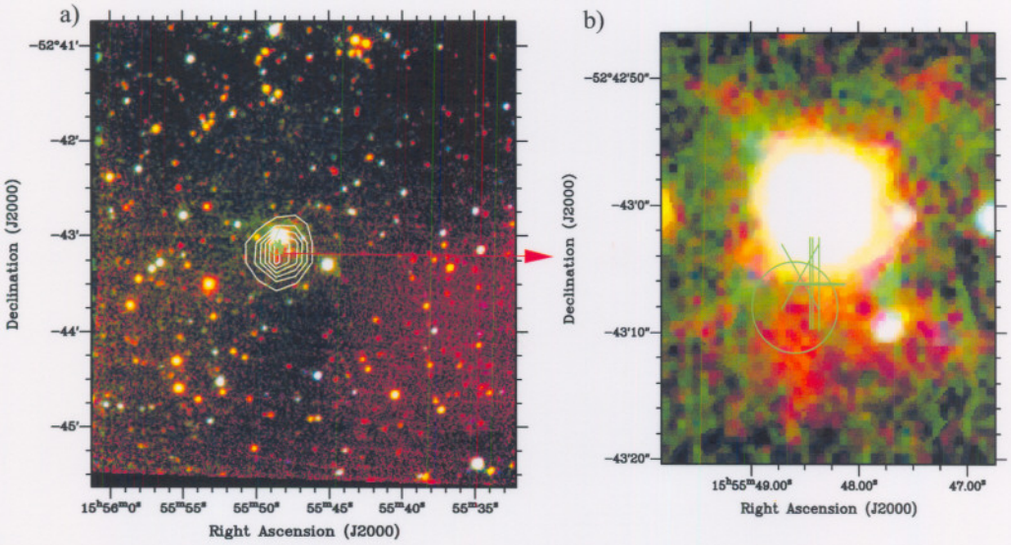

Figure 2.9: a. Three-colour composite image of the full field around G328.81+0.63. The known H II regions are marked with ○, water masers with ∗, 6.7 GHz methanol masers with + and hydroxyl masers with ×. b. Area around methanol maser

(Figure 2.9). This is most likely an unrelated source since its spectral energy distribution follows that of a reddened foreground star. A fainter source closer to the maser position is almost lost in the glare from the bright source. This source can be seen more clearly in the K band image of Osterloh et al. (1997). The magnitude of the K-band object 5″ south of the maser position is given, but this must be regarded as an upper limit since there is contamination from the bright source. An UC H II region is located 2″ to the south of the maser position. It seems that there is a compact embedded cluster here. The error ellipse of IRAS 15520–5234 is centred on the maser positions. The MSX survey shows an unresolved source centred on this position. De Buizer et al. (2002b) have imaged this field at mid-infrared wavelengths. They did not see the bright foreground star and so were able to see six embedded stars at 18 μm. They found that the main group of methanol masers coincided with a mid-infrared source. It is not clear whether this source is visible at the NIR. Walsh et al. (2001) imaged a larger field at 20 μm and obtained similar results.

2.4.7 G336.01–0.82

The error ellipse of IRAS 16313–4840 is centred on an area containing diffuse emission (Figure 2.10). The emission from an MSX point source peaks at the IRAS position. The methanol maser is 30″ away and outside of the IRAS error ellipse, therefore it is not associated with the IRAS source. There are no water masers in this region (Scalise et al., 1989). The hydroxyl maser coincides with the methanol masers. A very faint K band object appears at this position, but it may be an artifact of the diffraction spikes from a bright source to the northeast. Walsh et al. (1999) did not have a problem with diffraction spikes in their images and they did not see any NIR source at the methanol maser site.

2.4.8 G337.92–0.46

The error ellipse of IRAS 16374–4701 is centred on a bright cluster of sources approximately 23″ away from the methanol maser position (Figure 2.11). There is extended diffuse emission at K and H band. The methanol masers and a hydroxyl maser are 7″ apart and lie on either side of a faint extended reddened source. The K vs H-K colour of this source is not significantly different from several other sources in the field. The only compact H II region observed in the area is 40″ to the east of the methanol maser position. There is another centre of activity to the south with a water maser about 15″ away from an extended bright K band source and another hydroxyl maser on the edge of the extended source. The MSX images show an area with extended

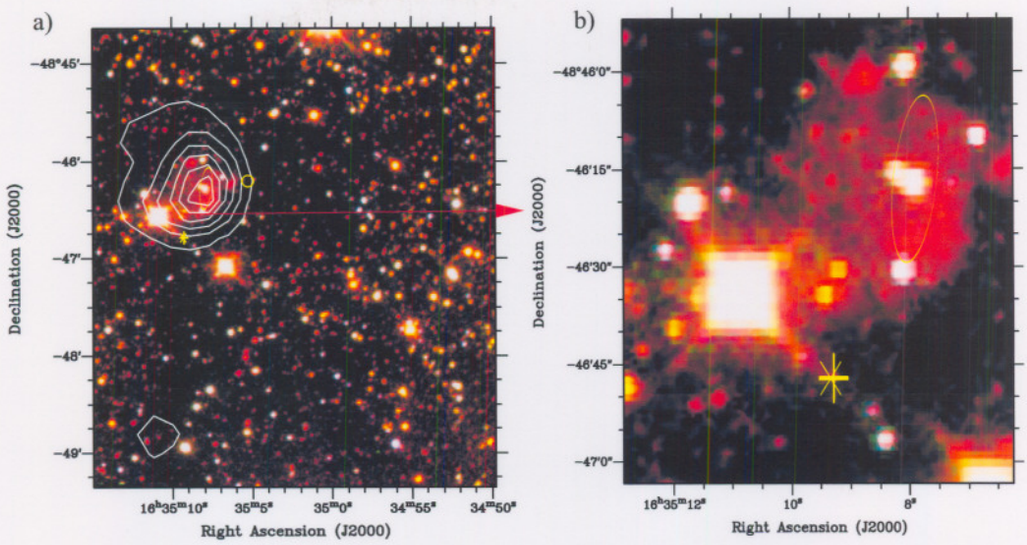

Figure 2.10: a. Three-colour composite image of the full field around G336.01-0.82. The known H II regions are marked with ∘, water masers with ∗, 6.7 GHz methanol masers with + and hydroxyl masers with ×. b. Area around methanol maser

emission at all bands. The mid-infrared emisssion is most intense at the IRAS position but it appears that there are multiple unresolved sources.

2.4.9 G339.62–0.12

The methanol and hydroxyl masers overlap in position and are at the edge of a bright NIR source (visible at K and H bands) with extended K band emission (Figure 2.12). Compared to other sources in the field with similar H-K colour, this source is the brightest at K band. The water maser does not appear to be close to any reddened objects but its position is obtained from single dish observations (Batchelor et al., 1980), therefore the position is not as accurate as from an interferometer. All the masers fall within the error ellipse of IRAS 16424–4531. The peak emission of the MSX point source corresponds to the position of the NIR source.

2.4.10 G339.88–1.26

The methanol maser is in a very crowded area with a lot of diffuse K band emission. It is just outside of the error ellipse of IRAS 16484–4603 (Figure 2.13). Extended emission at all MSX bands is seen in this area. A bright source is visible in all three bands at the methanol maser position but careful examina-

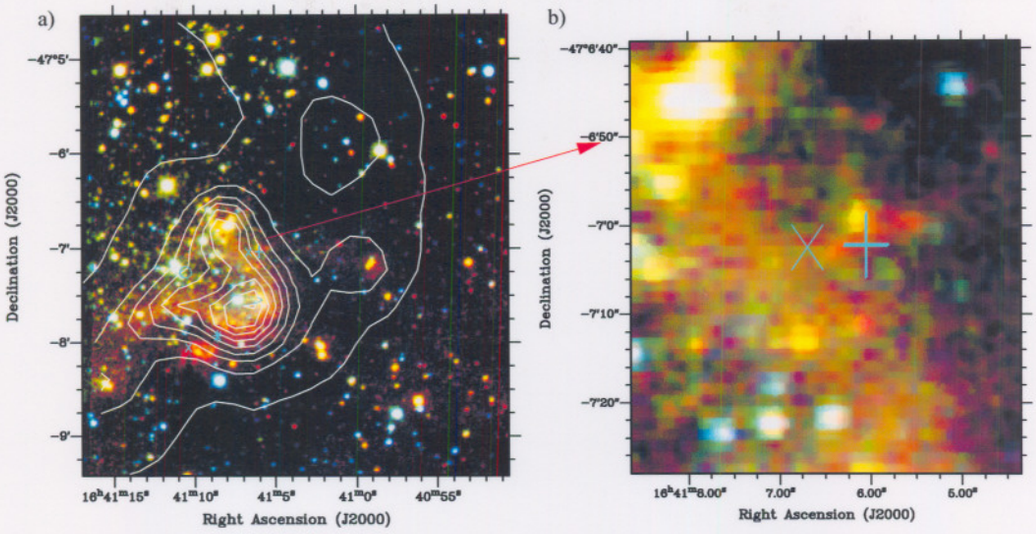

Figure 2.11: a. Three-colour composite image of the full field around G337.92-0.46. The known H II regions are marked with ∘, water masers with ∗, 6.7 GHz methanol masers with + and hydroxyl masers with ×. b. Area around methanol maser

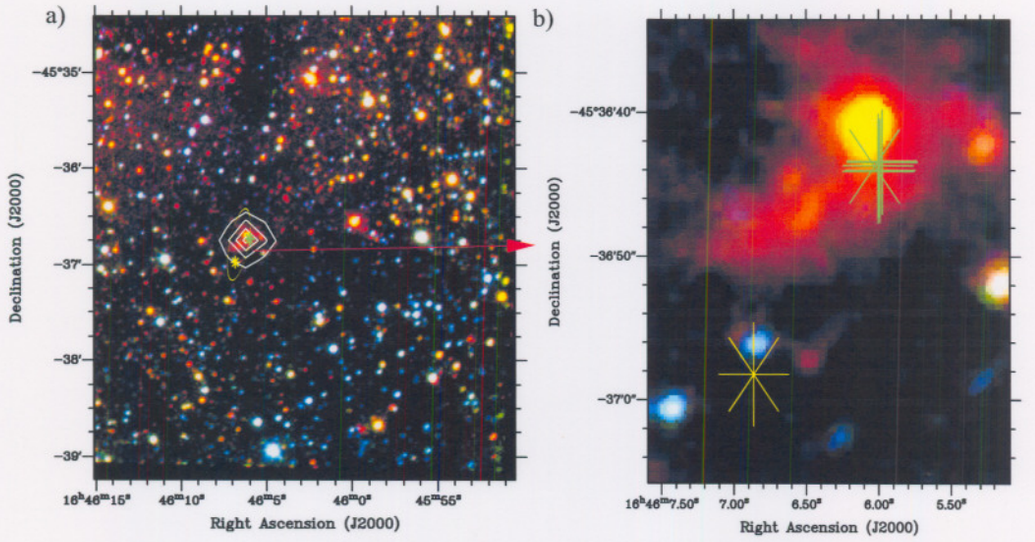

Figure 2.12: a. Three-colour composite image of the full field around G339.62-0.12. The known H II regions are marked with ∘, water masers with ∗, 6.7 GHz methanol masers with + and hydroxyl masers with ×. b. Area around methanol maser

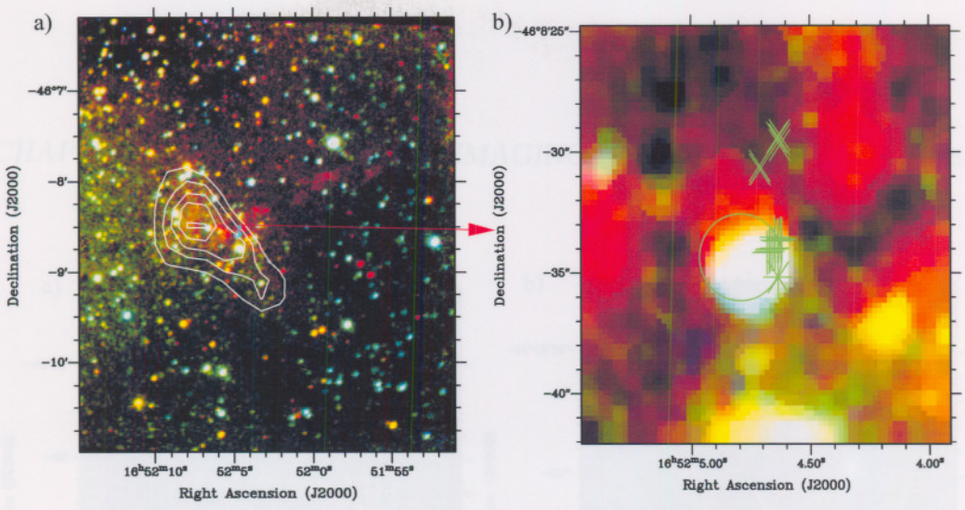

Figure 2.13: a. Three-colour composite image of the full field around G339.88-1.26. The known H II regions are marked with ○, water masers with ∗, 6.7 GHz methanol masers with + and hydroxyl masers with ×. b. Area around methanol maser

tion of the colour composite image shows a red arc north of the bright star. This is most likely an embedded K-band source which is partially obscured by the bright star in front of it. It was not possible to obtain accurate photometry of these two sources because of confusion. Neither source is a point source, so it was not possible to use the standard method of fitting a point-spread function and subtracting off the emission from the brighter source first.

De Buizer et al. (2002a) have imaged this source at mid-infrared wavelengths, where the bright foreground source is not visible. They observed an elongated source following the same alignment as the methanol masers. Walsh et al. (1999) found an elongated object at L band at this position. An UC H II region appears to be centred on the bright NIR source (note that there is an error in the table reporting the position in Ellingsen et al. (1996)). The hydroxyl and methanol masers lie on the other side of the NIR source. There is a water maser 4″ south of the K band source.

2.4.11 G340.79–0.10

The H II region, hydroxyl masers and methanol masers are situated in a region well away from the IRAS 16466-4437 (Figure 2.14). The only infrared sources visible within 15″ have blue colours similar to that of other field stars in the region. Walsh et al. (1999) also did not detect any reddened objects here. The IRAS error ellipse is on the edge of an MSX source. However, examination of

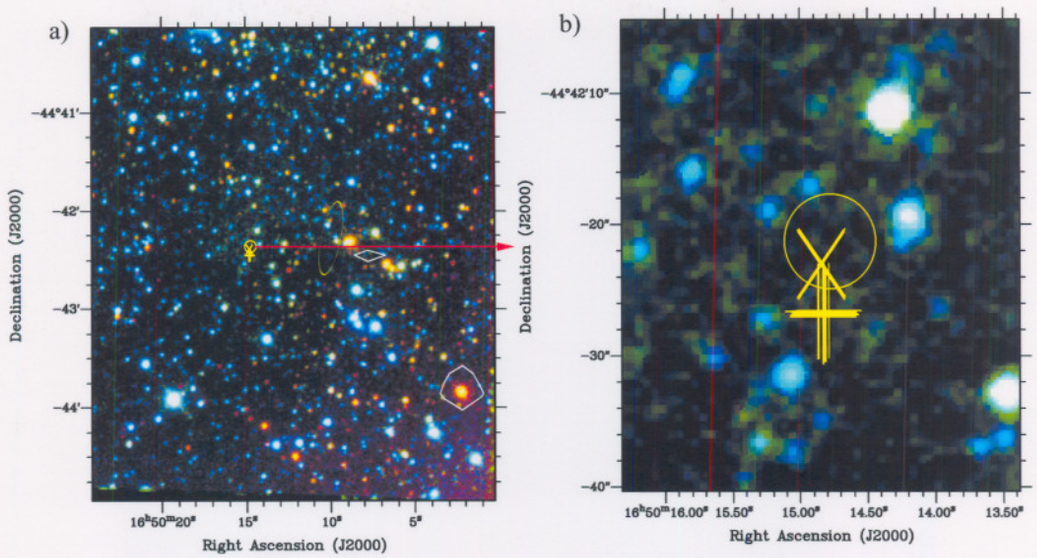

Figure 2.14: a. Three-colour composite image of the full field around G340.79-0.10. The known H II regions are marked with ∘, water masers with ∗, 6.7 GHz methanol masers with + and hydroxyl masers with ×. b. Area around methanol maser

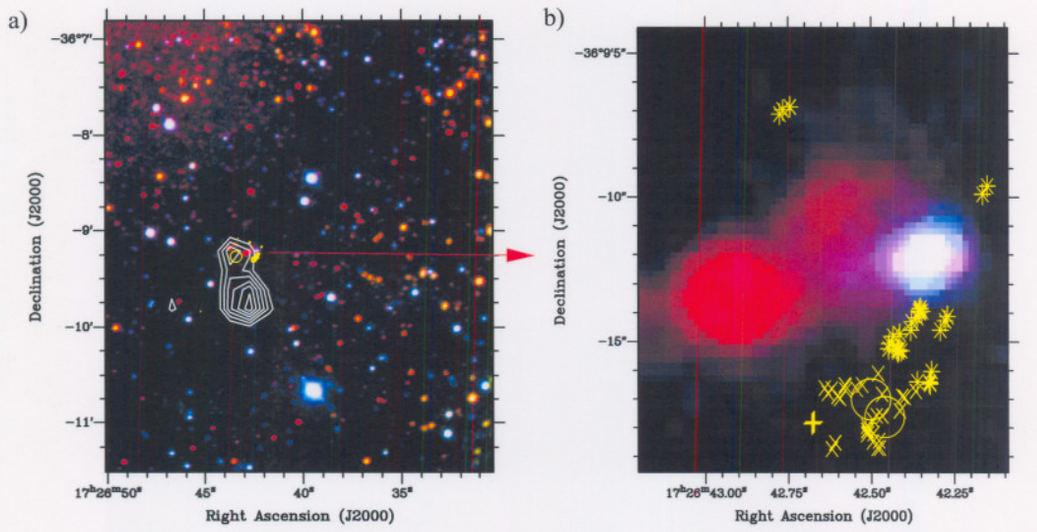

Figure 2.15: a. Three-colour composite image of the full field around G351.78-0.54. The known H II regions are marked with ∘, water masers with ∗, 6.7 GHz methanol masers with + and hydroxyl masers with ×. b. Area around methanol maser

the larger MSX field shows that the masers and H II region are at the edge of a dark region at A band. Egan et al. (1998) suggest that these regions are areas of absorption seen against the infrared-bright background of the Galactic plane. These regions are possibly extremely dense, cold dust clouds (Carey et al., 1998).

2.4.12 G351.78–0.54

The methanol, water and hydroxyl masers are offset from the position of IRAS 17233–3606 (Figure 2.15). The active star formation region appears to be in an area with high dust extinction since the source density is much lower than in other parts of the field. The MSX images show two unresolved point sources near, but not coincident with, the methanol masers. A dark filament in the MSX A band can be seen in this area. The position of the filament is consistent with the absence of reddened sources in that part of the field. There are two bright NIR sources with some diffuse emission close to the methanol maser position. The eastern source is only visible in K band while the western source has a bluer colour, making it unlikely to be a source in an early evolutionary stage. There is faint nebulosity at K band between the two NIR sources. Walsh et al. (1999) found that the eastern source has an L band counterpart. There are many groups of water masers, north-west of two UC H II regions. The hydroxyl masers are coincident with the H II regions while the methanol masers lie 2″ east of them. The large number of water and hydroxyl masers near these H II regions seem to indicate that there may be other stars even more deeply embedded than the sources that are detected in the NIR.

2.5 Discussion

2.5.1 Association of methanol masers with near-infrared objects

Care has to be taken when deciding if the infrared objects seen near the position of the methanol masers have any causal relationship to the masers. Only stars whose colours are characteristic of deeply embedded objects have been selected. However, it is possible that the object which is pumping the methanol maser is even more deeply embedded or in the hot core stage, in which case we would only be able to detect it at mid-infrared wavelengths. This possibility cannot be eliminated until the fields are imaged with high resolution in the mid-infrared as well.

An upper limit has to be set on the distances that objects can be from each other and still be related to the same star. The largest radius of the spherical UC H II regions mapped by Kurtz et al. (1994) is approximately 8 kAU, while the smallest radius reported is 0.2 kAU. A recent mid-infrared image of the site of an UC H II region (De Buizer et al., 2002b) shows a hot molecular core with a physical diameter of just over 7 kAU. If these distances are used as an indicator of the sphere of influence of a newly formed massive star, we can assume that methanol masers more than 8 kAU from the star are not associated with it. The projected distance has to be calculated for each object since this is dependent on the distance.

The sources listed in Table 2.2 satisfy the colour and distance criteria but they may be chance associations with other embedded stars in the star formation region. In the majority of the cases, the infrared source closest to the methanol maser is among the brightest K band objects in the entire field. This increases the probability that the association is not purely by chance. The unusually high K band flux density could be due to line emission from shocked molecular hydrogen at 2.122 μm. This can only be verified by doing narrow band imaging or spectroscopy. Some of the sources (G10.33–0.17B, G12.91–0.26, G45.07+0.13 and G339.62–0.12) do not follow the point spread function derived using DAOPHOT on other field stars. The nature of these objects is not clear at the resolution obtained in this work. There may be multiple unresolved sources or the object may have a non-spherical morphology, possibly as a result of the presence of outflows or a circumstellar disk.

One way to check for a causal relationship between the NIR object and the maser would be to monitor the infrared radiation from the star while monitoring the methanol maser. If the maser is being pumped by the infrared radiation from the star, we would expect to see a correlation between the variations in intensity of the objects.

2.5.2 Relation of methanol masers to other star formation tracers

The position of H II regions, hydroxyl masers and water masers can tell us more about the environment of the methanol masers. The existence of an H II region is a sure indicator of the presence of a high-mass ionizing star. Hydroxyl masers are found at the edges of compact H II regions (Garay et al., 1985), and are a good indicator of the presence of a high mass star even when the H II region may not be detectable. Water masers are found in shocks associated with high velocity outflows. However, water masers are associated with both high- and low-mass star formation and may be found some distance from the star driving the outflow, making it difficult to verify the association without

actually mapping the outflows.

We can assume, as discussed in the previous section, that objects with a separation of more than 8 kAU are not likely to be causally related. Table 2.4 shows the distances used to calculate the projected separations between the methanol maser source and other objects (Table 2.5). These separations are a lower value only, since we are using the near kinematic distance and we do not know the distance between the objects along the line of sight. In this discussion, the methanol maser is used as the reference point, rather than the possible NIR counterparts since it is not certain that these stars are related to the methanol maser. Sources are assumed to be related if the separation is less than 8 kAU (taking into account the uncertainties in the positions).

Figure 2.16 shows the relation between the methanol maser sources and other radio sources. All of the sources in this sample, except for G52.67–1.09, have been targeted by searches for compact H II regions, water masers and hydroxyl masers. Only G10.33–0.17 A, G10.33–0.17 B and G337.92–0.46 have no detectable compact H II regions (confirmed for G10.33–0.17 by a recent VLA observation by van der Walt et al. (2003)) or other maser species associated with them. Since G12.68–0.18 and G12.91–0.26 are in the extended H II region complex W33 (Bieging et al., 1978), it is possible that the higher noise levels make it difficult to detect weak compact H II regions. The majority of the methanol maser sources are close to compact H II regions or hydroxyl masers, indicating the presence of a massive star. There are no methanol maser sources associated with an H II region without the presence of other maser species, which is consistant with the hypothesis that the methanol masers are associated with an early evolutionary phase of the star.

2.5.3 MSX and IRAS sources

In the past, many researchers have used IRAS colours as selection criteria to find methanol masers or H II regions. Yet not all methanol masers appear to be associated with IRAS sources (Ellingsen et al., 1996). In our sample, eight out of 14 methanol maser sites are not within the IRAS error ellipse. However, far-infrared sources may be excluded from the IRAS point source catalogue because of confusion in densely populated areas. The higher resolution MSX survey gives a better incidence of methanol masers found within the contours of an MSX point source.

In comparison with IRAS, only two methanol masers (G10.33–0.17A and G340.79–0.10) are not coincident with MSX sources. In many cases it is clear that the IRAS PSC is simply selecting the area of brightest infrared emission or

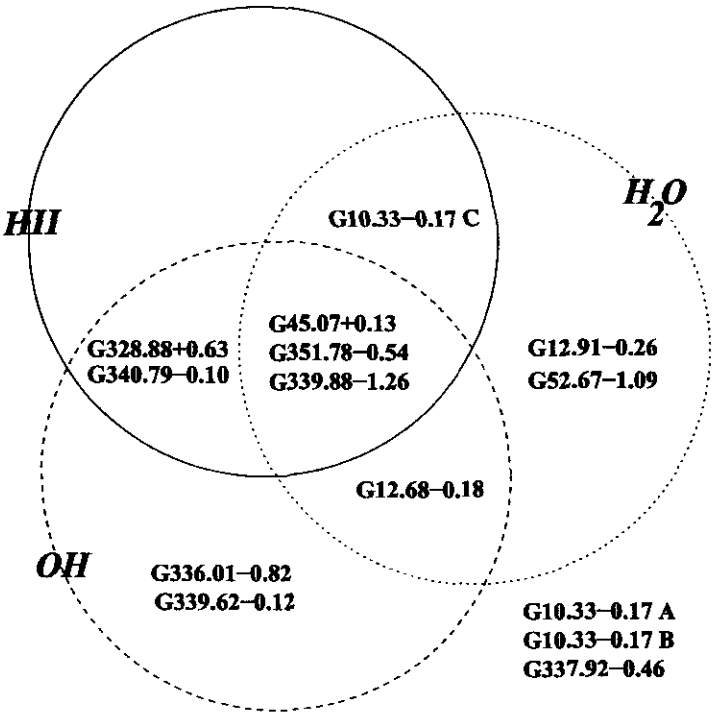

Figure 2.16: Venn diagram showing the association of methanol maser sources with other radio sources. The sources placed outside the circles are not associated with any other type of radio source.

is unable to distinguish between multiple sources. The MSX survey specifically targeted areas that IRAS marked as confused, as well as the entire Galactic plane. Therefore the MSX survey is a better tool to use when searching for potential infrared counterparts to methanol masers. However, the resolution and positional accuracy of MSX makes it impossible to identify the individual stars which are exciting the masers.

2.6 Summary

Twelve fields around methanol maser sources in the I, J, H and K bands have been imaged. Seven of the methanol masers sites are within 8 kAU of a near-infrared source with colours characteristic of a deeply embedded star. In many cases these sources are amongst the brightest K band sources in the field. Some of these sources are not point sources.

The crowded nature of the star formation regions makes it difficult to be certain that the star exciting the methanol masers has been identified. High

resolution observations at longer wavelengths are needed to identify objects which may be more deeply embedded. Monitoring the infrared source and the methanol masers to check for correlations in variability may be a way to test the association of the sources.

Chapter 3

6.7-GHz methanol maser monitoring at HartRAO

3.1 Introduction

A number of methanol masers have been found to be variable at 6.7 GHz (Caswell et al., 1995a; MacLeod & Gaylard, 1996) and 12.2 GHz (Moscadelli & Catarzi, 1996; MacLeod & Gaylard, 1993). The variability of the masers can be used to examine changing conditions in the star formation region. The study by Caswell et al. (1995a) followed the variability of a small sample of masers for a short time, with intervals between observations of the order of three months. However, observations of G351.78–0.54 show rapid variations on a time-scale of weeks when the maser is in an active phase (MacLeod & Gaylard, 1996). On the other hand, other masers appear to be non-varying over the same time-scales. Regular monitoring of a large sample of methanol masers will be able to give us an idea of how common methanol maser variability is and the typical time-scales of such. This data can ultimately be used to test maser models. Variations in maser intensity could be as a result of turbulent motions in the cloud with subsequent changes in maser path length, shocks, changes in the intrinsic brightness of the star, or partial quenching of the maser region. Some of the variations may be extrinsic to the maser source, eg interstellar scintillation. Thus, if methanol masers are sensitive to changes in their environment, they can be a powerful probe of changing conditions at small angular scales.

A programme to monitor the variability of 6.7 GHz methanol masers was started in January 1999. This chapter will cover the data obtained until September 2002. The details of the observing and calibrations are given in Section 2. The details of the source selection are given in Section 3. Section

Table 3.1: Observing parameters for large and small velocity range sources

Rest frequency (MHz)	6668.518	
System temperature (K)	50	
Half Power Beamwidth (°)	0.133	
Number of channels	256	
Bandwidth (MHz)	0.64	0.32
Velocity range ($km.s^{-1}$)	28	14
Correlator resolution ($km.s^{-1}$)	0.112	0.056

4 gives a short overview of the results and the behaviour of each source is discussed. The large data set precludes hard-copy plots of the times-series. Instead, the plots can be accessed from an html index on the attached CD-ROM. The results are summarised in Section 5.

3.2 Observations

The monitoring programme used the 26-m telescope at HartRAO. All observations were made using left circular polarisation. The sources were observed at intervals of 1–2 weeks,with observations at 2–3 day intervals when a source was seen to be varying rapidly. The observing parameters are summarised in Table 3.1. Two different bandwidths were used. The 0.32 MHz bandwidth gives a better velocity resolution, but does not have as large a velocity range as the 0.64 MHz bandwidth. Some of the sources cover a large velocity range and therefore have to be observed at 0.64 MHz bandwidth.

Pointing corrections were calculated by taking observations offset by half a beamwidth to the north, south, east and west of the source position. The pointing corrections at 6.7 GHz are on average less than 5%, therefore it is not a dominant factor in the calibrations at 6.7 GHz.

Since April 2000 the telescope surface (perforated aluminium) has been progressively upgraded with new high-accuracy solid panels. The point source sensitivity (PSS) of the telescope was regularly measured by observing 3C123, 3C218 and 3C274. Prior to the upgrade the PSS was found to be 15.7 $Jy.K^{-1}$ at 6.7 GHz, based on the Ott et al. (1994) flux density scale. During the upgrade period regular calibrations were made using precision Dicke radiometry at 4.9- and 8.6 GHz. Changes relative to the pre-upgrade values for the PSS at 6.7 GHz were obtained by interpolating the PSS measured at these two wavelengths. The corrections obtained are believed to be accurate to 5% or better.

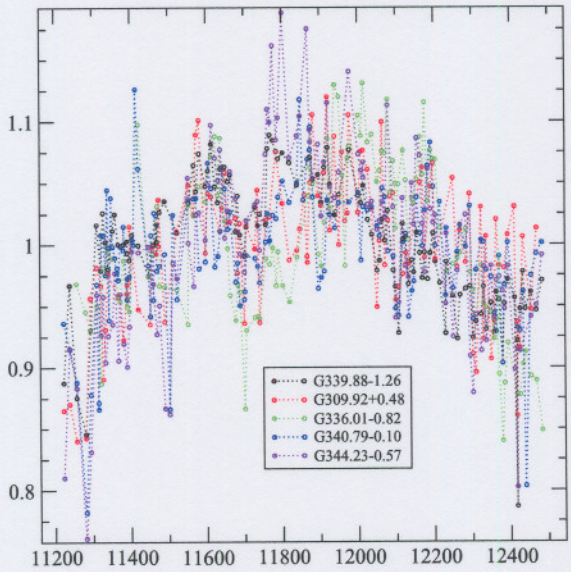

Figure 3.1: Normalised time-series for sources showing strongly correlated variations.

The validity of the corrections was tested by applying them to other varying sources in the monitoring sample. The strongest peaks in the sources G339.88–1.26, G309.92+0.48, G336.01–0.82, G340.79–0.10 and G344.23–0.57 appear to show very little variation but do show common features at the 5% level in their time-series (Figure 3.1). Cross-correlation of the time-series shows that the variations are indeed common to all five time-series (Figure 3.2). The common variations can be characterised by a slow second-order variation probably caused by uncalibrated system changes, as well as stronger fluctuations with a time-scale of about 3 months. These effects have not been corrected for but, since they are common to all the sources, they do not affect the statistical analysis and they are kept in mind during examination of the maser behaviour. The large sample size as well as the presence of independently varying features towards the same source provides an effective means of cross-checking the amplitude calibration. Figure 3.3 shows the time-series of two features in G337.92–0.46, showing a highly variable feature in contrast to one showing no variation to within the noise.

3.3 Source selection

The initial source list mainly consisted of sources listed as variable by Caswell et al. (1995a) or van der Walt et al. (1996). G351.78–0.54 had been monitored on a regular basis from 1993 to 1995 by MacLeod & Gaylard (1996) and was

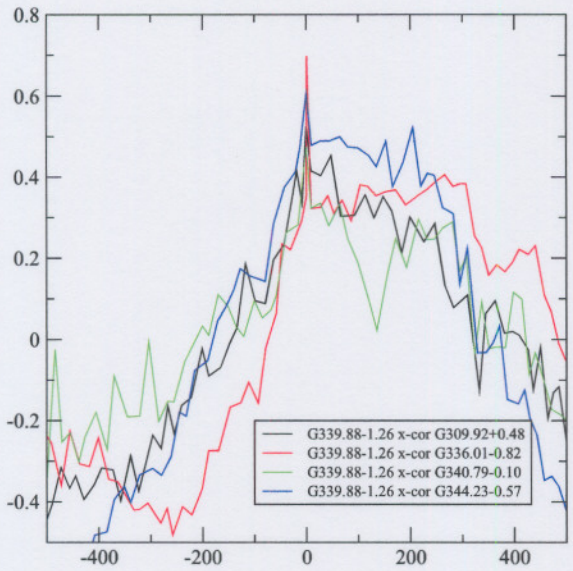

Figure 3.2: Cross-correlation of the time-series of dominant feature in G339.88–1.26 with time-series from other sources showing similar variations.

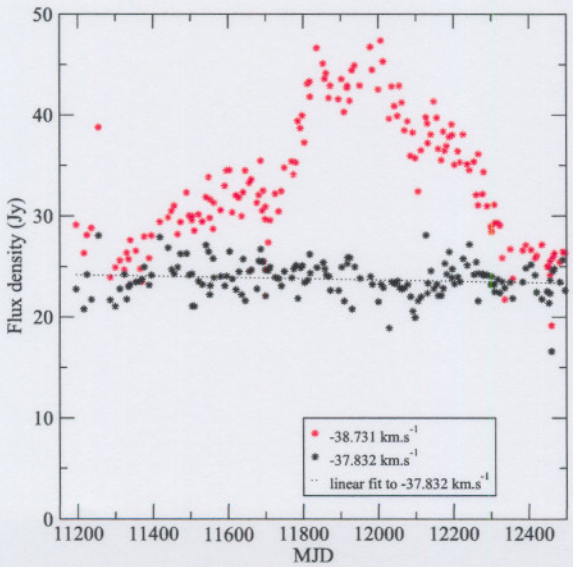

Figure 3.3: Time-series of two maser features in G337.92–0.46.

found to be highly variable on time-scales of a few months. Other sources were selected because comparision of the flux densities reported by Caswell et al. (1995b) and those reported by Menten (1991) showed that the peak flux densities had changed. Sources reported to be variable at 12.2 GHz (Moscadelli & Catarzi, 1996) were also selected. Some sources were dropped after the initial test observations because they were too weak or because of confusion with a neighbouring source. The final source list is given in Table 3.2.

Table 3.2: List of sources monitored at 6.7 GHz. The V_{lsr} on which the bandwidth was centred is given.

Source	RA (B1950)	Dec (B1950)	V_{lsr}
174.20–0.08	05 : 27 : 32.4	33 : 45 : 52.0	2.5
213.71–12.60	06 : 05 : 21.7	–06 : 22 : 28.0	11.0
189.03+0.79	06 : 05 : 40.9	21 : 31 : 37.6	11.0
188.95+0.89	06 : 05 : 53.5	21 : 39 : 02.0	10.0
192.60–0.05	06 : 09 : 59.1	18 : 00 : 10.0	3.5
196.45–1.68	06 : 11 : 47.1	13 : 50 : 34.0	14.0
287.36+0.64	10 : 46 : 03.4	–58 : 10 : 58.0	–2.0
291.27–0.71	11 : 09 : 44.7	–61 : 02 : 17.2	–26.9
294.52–1.62	11 : 33 : 15.0	–62 : 58 : 13.0	–11.5
298.26+0.74	12 : 09 : 08.4	–61 : 29 : 37.5	–30.0
305.21+0.21	13 : 08 : 01.7	–62 : 18 : 45.3	–38.0
308.92+0.12	13 : 39 : 37.0	–61 : 53 : 44.0	–54.0
309.92+0.48	13 : 47 : 11.9	–61 : 20 : 18.8	–59.0
312.11+0.26	14 : 05 : 02.2	–60 : 58 : 48.0	–50.0
316.64–0.09	14 : 40 : 31.6	–59 : 42 : 40.0	–19.5
318.95–0.2	14 : 57 : 03.8	–58 : 47 : 01.2	–35.0
320.23–0.29	15 : 06 : 00.5	–58 : 14 : 14.0	–64.5
322.16+0.64	15 : 14 : 45.7	–56 : 27 : 28.0	–58.5
323.77–0.21	15 : 27 : 49.8	–56 : 20 : 15.0	–50.5
328.81+0.63	15 : 52 : 00.3	–52 : 34 : 22.2	–44.5
328.24–0.55	15 : 54 : 06.1	–53 : 50 : 47.0	–39.0
331.28–0.19	16 : 07 : 37.9	–51 : 34 : 12.2	–82.5
331.13–0.24	16 : 07 : 10.8	–51 : 42 : 29.0	–86.5
335.55–0.31	16 : 27 : 11.3	–48 : 39 : 28.0	–114.5
337.92–0.46	16 : 37 : 25.0	–47 : 01 : 21.0	–38.5
338.93–0.06	16 : 39 : 36.5	–46 : 00 : 05.0	–43.0
339.62–0.12	16 : 42 : 26.5	–45 : 31 : 18.0	–34.5
336.99–0.03	16 : 31 : 51.9	–47 : 25 : 03.0	–121.5
336.01–0.82	16 : 31 : 21.8	–48 : 40 : 51.0	–47.0
340.79–0.10	16 : 46 : 38.4	–44 : 37 : 18.5	–100.0
339.88–1.26	16 : 48 : 24.8	–46 : 03 : 33.9	–36.0
344.23–0.57	17 : 00 : 35.0	–42 : 14 : 29.0	–24.5

continued on next page

continued from previous page

Source	RA (B1950)	Dec (B1950)	V_{lsr}
345.50+0.35	17 : 00 : 54.2	–40 : 40 : 18.0	–17.0
345.00–0.22	17 : 01 : 38.5	–41 : 24 : 59.0	–26.0
351.42+0.64	17 : 17 : 32.3	–35 : 44 : 04.0	–7.0
351.58–0.35	17 : 22 : 03.2	–36 : 10 : 09.0	–93.5
351.78–0.54	17 : 23 : 20.7	–36 : 06 : 45.4	1.5
354.61+0.47	17 : 26 : 59.8	–33 : 11 : 34.0	–20.0
359.61–0.24	17 : 42 : 27.2	–29 : 22 : 18.0	20.5
9.62+0.2	18 : 03 : 15.9	–20 : 31 : 52.9	2.5
10.47+0.03	18 : 05 : 40.5	–19 : 52 : 23.0	69.0
10.33–0.17	18 : 06 : 06.7	–20 : 05 : 34.0	10.5
12.89+0.49	18 : 08 : 56.4	–17 : 32 : 14.0	35.0
12.68–0.18	18 : 10 : 59.3	–18 : 02 : 40.0	55.5
12.91–0.26	18 : 11 : 44.2	–17 : 52 : 58.0	38.0
23.01–0.41	18 : 31 : 56.7	–09 : 03 : 18.0	77.0
23.44–0.18	18 : 31 : 55.3	–08 : 34 : 01.0	103.5
35.20–1.74	18 : 59 : 13.1	01 : 09 : 07.0	43.0
45.07+0.13	19 : 11 : 00.5	10 : 45 : 41.0	58.5
52.668–1.09	19 : 30 : 20.2	16 : 51 : 04.0	66.0
59.78+0.06	19 : 41 : 03.6	23 : 36 : 51.0	25.0
78.12+3.63	20 : 12 : 40.0	41 : 04 : 20.0	–6.0
W75N	20 : 36 : 50.4	42 : 27 : 23.0	6.5

3.4 Overview of results

3.4.1 Variability index

Each maser spectrum consists of a number of peaks, corresponding to emission from maser spots at different velocities. Velocity channels at the maximum intensity for each peak were selected for the following analysis. Since the relation of the spatial structure of the maser to the velocity structure is not known, it was decided not to average the channels in each peak in order to minimise the chance of combining data from multiple maser spots.

While it is easy to judge the degree of variability of a source by eye, a more objective method is needed to deal with a large number of sources. The following formula for a variability index is an adaptation of that developed by

Stetson (1996) for automated searches for Cepheid variables:

$$I = \frac{\sum_{i=1}^{N} (m(t_i) - \bar{m})^2 - \sum_{i=1}^{N} (n(t_i) - \bar{n})^2}{\bar{m}}$$

where N is the total number of observations, $m(t_i)$ is the observed intensity at a given velocity channel, $n(t_i)$ is the intensity at a noise channel (the noise time-series channel is any channel in the spectrum in which there is no maser emission) and $\bar{m}$ and $\bar{n}$ are the average intensities. The variability index is normalised by dividing by the average maser flux density, which is taken over the entire time-series. Thus, a non-varying maser will have an index tending towards zero. Note that the index can go negative for sources with a poor signal-to-noise ratio (S/N). Therefore the average flux density as well as the S/N has to be taken into account when interpreting the variability index.

Figure 3.4 shows a histogram of the variability indices for all the maser peaks. The ranges corresponding to descriptions such as 'highly variable' and 'significantly variable' are difficult to define but for ease of discussion divisions have been selected after visual examination of the data set. Sources with an index below one are deemed not significantly variable over the time range analysed. Table 3.3 gives a list of the most variable maser peaks ie those with a variability index greater than three[1]. The entries are sorted in order of decreasing variability index. The average rms noise is given as well as the average uncertainty σ_m for each maser peak taking into account the rms noise as well as calibration error. This is given by

$$\sigma_m = \sqrt{{\sigma_{rms}}^2 + \left(\frac{\delta T_{sys}}{T_{sys}} * T_m\right)^2}$$

where T_{sys} is the average system temperature, δT_{sys} is the uncertainty in the system temperature, T_m is the antenna temperature at the maser peak and σ_{rms} is the rms noise. The rms noise is calculated using the radiometer equation:

$$\sigma_{rms} = \frac{K * T_{sys}}{\sqrt{\Delta\nu * \tau * f}}$$

where K is the correlator quantisation factor ($K = 1.235$ for the HartRAO correlator), $\Delta\nu$ is the bandwidth per channel in Hz, τ is the total integration time, $f = 1$ if the observations were position-switched and $f = 2$ if the observations were frequency-switched.

The most variable maser feature in the sample is an otherwise insignificant feature in NGC6334F (Figure 3.5). This peak increased from below the detection limit of 1.5 Jy to 270 Jy in two months. It stayed at this level for a month and then gradually subsided to below the detection limit over the next 10 months.

[1]The full set of calculations are on the CD-ROM.

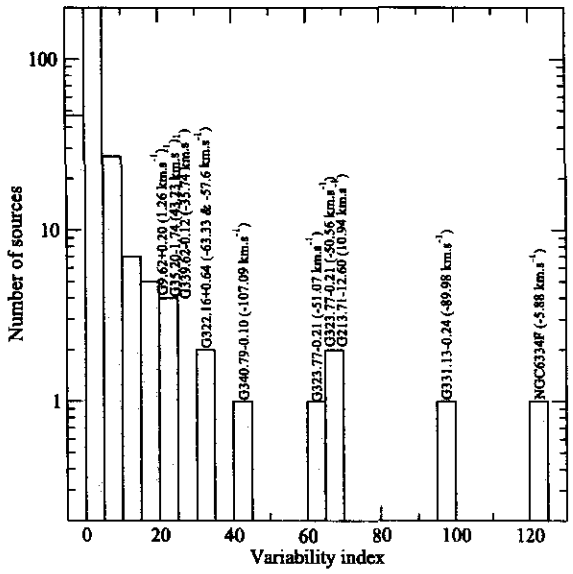

Figure 3.4: Histogram of the variability indices. The most variable sources are identified on the histogram.

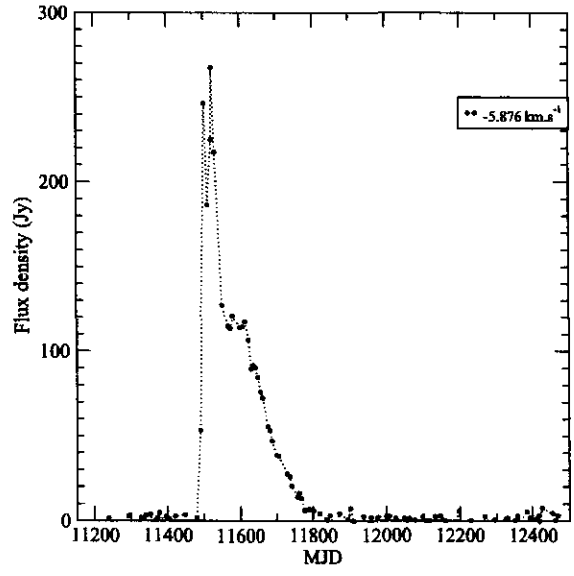

Figure 3.5: Time-series of the –5.786 km.s^{-1} feature in NGC6334F. This feature has the highest variability index in the sample.

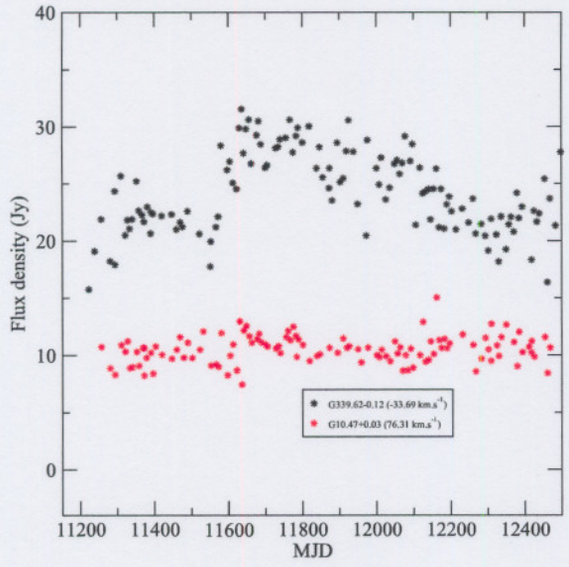

Figure 3.6: Time-series of a moderately variable feature in G339.62–0.12 (I=2.98) and a non-varying feature in G10.47+0.03 (I=-0.04).

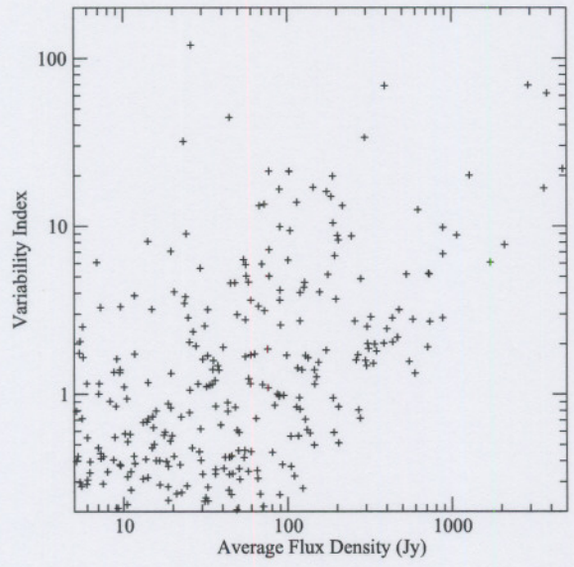

Figure 3.7: Variability index plotted against average flux density. Note that the scales are logarithmic.

As a comparision, Figure 3.6 shows the time-series of a non-varying maser and that of one which is moderately variable.

There does not appear to be any link between the average flux density of a maser peak and its degree of variability, as can be seen in Figure 3.7. Sources with an average flux density below 5 Jy are generally too weak to monitor for variability above the noise.

Table 3.3: List of most variable maser peaks 6.7 GHz.

Source	maser velocity ($km.s^{-1}$)	noise channel ($km.s^{-1}$)	ave flux density (Jy)	σ_m (Jy)	rms noise (Jy)	S/N	variability index
NGC6334F	-5.88	-12.96	25.89	0.83	0.56	31	120.09
G331.13-0.24	-89.98	-88.41	2.51	0.31	0.30	8	98.04
G323.77-0.21	-50.56	-52.47	2928.78	94.22	0.91	31	69.22
G213.71-12.60	10.94	8.19	392.00	12.07	0.98	32	68.69
G323.77-0.21	-51.07	-52.47	3800.25	122.25	0.91	31	61.89
G340.79-0.10	-107.09	-112.03	44.26	1.12	0.37	40	44.43
G322.16+0.64	-63.33	-58.84	296.00	7.02	0.60	42	33.65
G322.16+0.64	-57.60	-58.84	23.25	0.81	0.60	29	31.96
G9.62+0.20	1.26	-2.95	4719.96	143.66	1.08	33	21.92
G35.20-1.74	43.23	37.72	77.05	1.86	0.52	41	21.23
G339.62-0.12	-35.74	-41.02	102.18	2.53	0.54	40	21.20
G323.77-0.21	-49.55	-52.47	1278.87	41.15	0.91	31	20.08
G322.16+0.64	-64.01	-58.84	188.48	4.50	0.60	42	19.83
G345.00-0.22	-22.52	-19.48	143.42	3.30	0.31	43	17.01
NGC6334F	-10.37	-12.96	3633.06	85.01	0.56	43	16.84
G345.00-0.22	-22.97	-19.48	89.22	2.07	0.31	43	16.59
G351.78-0.54	1.28	-1.31	172.89	4.00	0.68	43	16.08
W75N	4.03	1.72	184.16	5.98	1.36	31	15.00
G322.16+0.64	-56.37	-58.84	113.90	2.76	0.60	41	13.87
G345.00-0.22	-26.79	-19.48	72.06	1.68	0.31	43	13.51
G322.16+0.64	-56.81	-58.84	67.31	1.70	0.60	40	13.24
G323.77-0.21	-53.09	-52.47	216.04	7.01	0.91	31	13.23
W75N	7.12	1.72	621.93	19.70	1.36	32	12.52
G351.78-0.54	1.73	-1.31	189.44	4.37	0.68	43	10.44
G322.16+0.64	-54.57	-58.84	89.74	2.21	0.60	41	9.92
G323.77-0.21	-49.10	-52.47	882.81	28.41	0.91	31	9.82
G12.68-0.18	59.83	48.98	103.68	2.69	1.02	39	9.40
G345.00-0.22	-30.38	-19.48	24.15	0.63	0.31	38	9.00
G323.77-0.21	-48.54	-52.47	1070.63	34.45	0.91	31	8.83
G345.50+0.35	-17.67	-23.63	201.13	4.47	0.31	45	8.79
G35.20-1.74	44.69	37.72	245.29	5.71	0.52	43	8.72

continued on next page

continued from previous page

Source	maser velocity ($km.s^{-1}$)	noise channel ($km.s^{-1}$)	ave flux density (Jy)	σ (Jy)	rms noise (Jy)	S/N	variability index
NGC6334F	-7.34	-12.96	203.77	4.80	0.56	42	8.25
G331.13-0.24	-85.60	-88.41	14.09	0.46	0.30	31	8.13
NGC6334F	-11.16	-12.96	2091.86	48.95	0.56	43	7.75
G213.71-12.60	10.49	8.19	77.08	2.56	0.98	30	7.24
G340.79-0.10	-106.64	-112.03	19.44	0.59	0.37	33	7.09
G35.20-1.74	42.44	37.72	881.96	20.46	0.52	43	6.83
G345.50+0.35	-14.30	-23.63	193.58	4.30	0.31	45	6.67
G359.61-0.24	22.75	14.99	53.82	1.24	0.46	44	6.32
G339.88-1.26	-33.08	-41.51	100.65	2.51	0.58	40	6.27
G339.88-1.26	-38.81	-41.51	1711.90	41.52	0.58	41	6.10
G331.13-0.24	-90.77	-88.41	6.87	0.35	0.30	20	6.08
G12.68-0.18	59.15	48.98	69.54	1.96	1.02	36	5.95
G345.50+0.35	-19.70	-23.63	55.58	1.27	0.31	44	5.90
G322.16+0.64	-60.07	-58.84	29.32	0.92	0.60	32	5.62
G339.88-1.26	-35.21	-41.51	718.85	17.44	0.58	41	5.22
G328.24-0.55	-44.73	-40.57	728.09	17.00	0.88	43	5.18
G323.77-0.21	-48.15	-52.47	528.03	17.01	0.91	31	5.17
G345.50+0.35	-14.53	-23.63	175.98	3.91	0.31	45	5.15
G345.00-0.22	-23.75	-19.48	56.00	1.32	0.31	42	5.04
G339.88-1.26	-32.29	-41.51	77.01	1.96	0.58	39	5.04
G322.16+0.64	-63.00	-58.84	278.43	6.61	0.60	42	4.86
G35.20-1.74	43.56	37.72	57.70	1.44	0.52	40	4.65
G345.50+0.35	-18.46	-23.63	126.71	2.82	0.31	45	4.62
G213.71-12.60	11.96	8.19	47.72	1.76	0.98	27	4.60
G78.12+3.63	-6.11	-10.61	44.88	1.15	0.54	39	4.58
G322.16+0.64	-62.10	-58.84	125.52	3.03	0.60	41	4.32
G345.50+0.35	-16.55	-23.63	89.82	2.01	0.31	45	4.16
G331.13-0.24	-84.25	-88.41	20.35	0.59	0.30	35	4.07
G345.50+0.35	-15.65	-23.63	156.52	3.48	0.31	45	4.05
G10.33-0.17	9.94	3.53	118.91	2.56	0.48	46	4.03
G340.79-0.10	-107.76	-112.03	11.67	0.46	0.37	25	3.87
G340.79-0.10	-108.43	-112.03	23.81	0.68	0.37	35	3.80
G328.24-0.55	-44.28	-40.57	196.69	4.67	0.88	42	3.68
G345.50+0.35	-16.66	-23.63	89.52	2.01	0.31	45	3.63
W75N	3.47	1.72	59.65	2.33	1.36	26	3.63
G359.61-0.24	19.94	14.99	23.50	0.68	0.46	34	3.48
G294.52-1.62	-8.92	-14.26	0.85	0.35	0.35	2	3.39
G174.20-0.08	1.66	-0.59	66.36	2.26	0.55	29	3.34
G10.33-0.17	4.99	3.53	9.58	0.52	0.48	18	3.32
G12.89+0.49	37.81	27.02	7.24	0.50	0.48	14	3.28

continued on next page

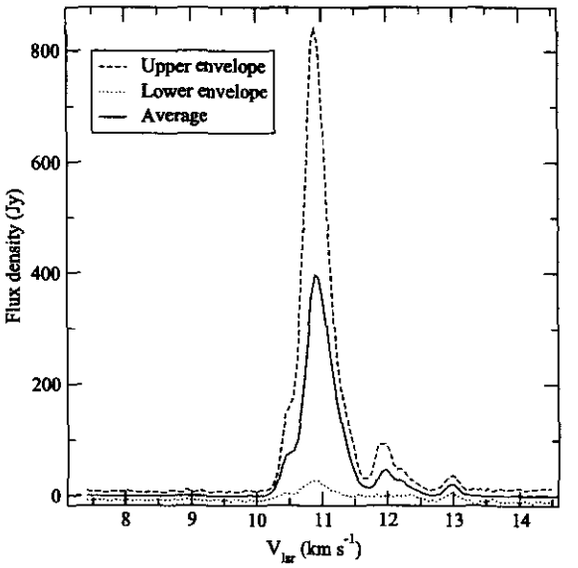

Figure 3.8: Range of variation in spectrum of G213.71-12.60.

continued from previous page

Source	maser velocity ($km.s^{-1}$)	noise channel ($km.s^{-1}$)	ave flux density (Jy)	σ (Jy)	rms noise (Jy)	S/N	variability index
G294.52-1.62	-11.90	-14.26	14.87	0.54	0.35	28	3.21
G339.62-0.12	-37.31	-41.02	32.57	0.96	0.54	34	3.19
G188.95+0.89	10.79	7.02	476.60	13.24	0.56	36	3.19
NGC6334F	-7.90	-12.96	72.28	1.78	0.56	41	3.14

3.4.2 Notes on individual sources

The average spectra with upper and lower envelopes for each source are given on the CD-ROM[2]. Upper and lower envelopes are calculated by finding the maxima and minima in the time-series at each velocity channel. They serve as a useful visual indication of the range of variability of a source.

G174.20–0.08
The peak at 1.657 $km.s^{-1}$ remained constant for several years before starting a steady decline. The peak at 4.017 $km.s^{-1}$ is also slightly variable. There is no significant activity from the other features.

[2]Open the file index.html in a web browser.

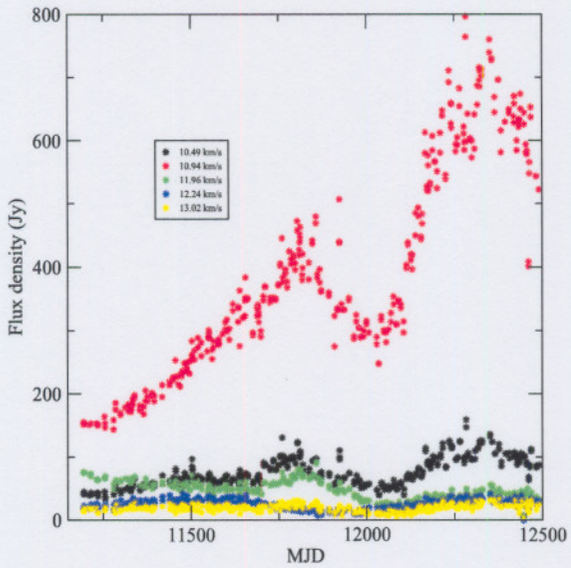

Figure 3.9: Time-series for selected velocity channels in G213.71-12.60.

G213.71–12.60
This source shows the most noticeable changes in spectral line profile. Figure 3.8 shows the range of variation of the features. The time-series for the dominant spectral features is shown in Figure 3.9. The 10.94 km.s^{-1} feature increased in intensity from 150 Jy to 800 Jy over three years. The 11.960 km.s^{-1} feature has been slowly decreasing in strength. There is no correlation between the behaviour in the two peaks. The spot maps of Minier et al. (2000) show a complex structure.

G188.95+0.89
All the features in this source vary simultaneously with a quasi-periodic variation of 391 days. The periodic behaviour will be discussed in detail in the next chapter. The masers spots have a linear arrangement, but the position-velocity distribution are not consistant with a Keplerian disk (Minier et al., 2000).

G189.03+0.79
This source is very weak and the changes in the time-series are dominated by the noise.

G192.60–0.05
The features at 4.624 and 5.411 km.s^{-1} are moderately variable. The flares last from a few months up to a year, with only a few weeks between flares. The spot maps of Minier et al. (2000) show a complex spot distribution.

G196.45–1.68
There appears to be a sinusoidal variation at all features, with a period of 668 days. This source will be discussed in detail in the next chapter.

G287.36+0.64
The weaker features are not variable to within the noise while the peak at -1.888 km.s^{-1} is slowly increasing in strength.

G291.27–071
The peak at -29.641 km.s^{-1} shows a monotonic decrease in intensity. The other features are not significantly variable.

G294.52–1.62
The peak at -11.900 km.s^{-1} is moderately variable. The maser at -8.921 km.s^{-1} flared above the detection limit for a few weeks.

G298.26+0.74
This source is very weak and not significantly variable to within the noise.

G305.21+0.21
The peak at -38.939 km.s^{-1} shows a gradual increase in intensity. The other features have a low variability index but also show a slow monotonic increase in intensity. The spot maps of Phillips et al. (1998) show a complex distribution.

G308.92+0.12
This source is not significantly variable. The maser spots have a complex distribution (Phillips et al., 1998).

G309.92+0.48
The feature at -59.787 km.s^{-1} showed a gradual increase in 1999 and subsequently started slowly decreasing in intensity. The other features are not significantly variable. The low-amplitude variations seen in all the maser features are due to errors in the amplitude calibration, as discussed previously. The maser spots are in a curve and show a linear velocity gradient (Phillips et al., 1998).

G312.11+0.26
This source is very weak but shows a quasi-periodic variation with a period of one year. This will be discussed in the next chapter.

G316.64–0.09
Some of the features show a quasi-periodic variation with a period of 448 days. This will be discussed in the next chapter. The maser spots have a complex morphology (Phillips et al., 1998).

G318.95–0.20
This source shows a weak variation with a period of one year. This will be discussed in the next chapter. The maser spots are in a curve but show no velocity gradient (Phillips et al., 1998).

G320.23–0.29
This source is moderately variable. The peaks at -62.259, -61.466 and -61.915 km.s^{-1} show simultaneous, sporadic flares. The other features are not variable to within the noise.

G322.16+0.64
This source is highly variable. The flares occur simultaneously at all the features, but the strength of the flares varies between different features.

G323.77–0.21
This source is highly variable. The variations occur simultaneously and with the same percentage amplitudes at all the features. One noteworthy flare occurred towards the end of year 2000, when the dominant feature flared from 4000 Jy to 5800 Jy and then decreased to its pre-flare levels. The flares can last from months to more than a year, with just a few weeks between flares. The maser spots are in a curve with a linear velocity gradient (Phillips et al., 1998).

G328.81+0.63
This source is not significantly variable. It has a linear spot distribution but no velocity gradient (Norris et al., 1998).

G328.24–0.55
This source is moderately variable. Some of the features show periodic variations with a period of 216 days. This source will be discussed in detail in the next chapter.

G331.13–0.24
This source is highly variable. There are two groups of maser features, each of which displays possible periodic flares with periods of 470 and 572 days respectively. The features at -91.558 and -91.771 km.s^{-1} are below the detection limit for almost 50% of the cycle. This source will be discussed further in the next chapter.

G331.28–0.19
Most of the features are not significantly variable, except for the feature at -85.091 km.s^{-1}, which has started gradually decreasing in intensity since year 2000. The spots have a complex morphology (Phillips et al., 1998).

355.55–0.31
This source is very weak and shows no variability to within the noise.

336.01–0.82
The features are not significantly variable, except for the feature at -53.406 km.s^{-1}, which has been decreasing in intensity since the year 2001.

G339.99–0.03
The main feature is not significantly variable. The other features are very weak and show no variation to within the noise.

G337.92–0.46
Most of the features are very weak and show no variation to within the noise. The peak at -38.731 km.s^{-1} increased from 20 Jy to 50 Jy and then decreased back to 20 Jy after about 1.5 years.

G338.92–0.06
This source is moderately variable. The -41.988 km.s^{-1} feature shows periodic variations with a period of 132 days. This will be discussed in detail in the next chapter.

G339.62–0.12
The majority of the peaks in this source are variable. A group of features show periodic flares with a period of 202 days. Other features show uncorrelated variations. The periodic behaviour will be discussed in the next chapter. The maser spots have a complex morphology (Walsh et al., 1998).

G339.88–1.26
Most of the peaks show simultaneous variations. As discussed earlier, the variations seen in this source are observed in other sources as well and are due to calibration time-series errors. The feature at -38.078 km.s^{-1} is increasing in intensity, while the feature at -32.291 km.s^{-1} is decreasing. A discrete correlation function of the two does not show any correlation. The maser spots have a linear distribution but do not show a velocity gradient (Norris et al., 1998).

G340.79-0.10
This source has a complex spectrum and most of the peaks are highly variable. Some of the features which are otherwise non-varying have a high frequency 'flicker' which correlates weakly with the variations seen in G339.88-1.26. The spot maps of Phillips et al. (1998) show a complex distribution.

G344.23–0.57
The two dominant features in this source are moderately variable. The variations are not correlated. The other features are very weak and show no

variation to within the noise. The maser spots are in a curve but show no velocity gradient (Walsh et al., 1998)

G345.50+0.35
This source is highly variable. The different features show the same pattern of flares but there is some time delay in the flares. The maser spots have a complex distribution (Walsh et al., 1998).

G345.00–0.22
A group of features are highly variable, with simultaneous flares. The other features are not significantly variable. The spatial distribution of the spots is complex, with two distinct groups of sources seen (Phillips et al., 1998). This grouping is consistent with the two different sets of variability behaviour.

NGC6334F
This source is highly variable. Not all of the features show simultaneous variations. The feature at -5.876 km.s^{-1} has the highest variability index in the entire sample. It is below the detection limit for most of the monitoring period. The maser spots are in a line, but a position-velocity diagram shows two lines with opposite slopes, implying the presence of two Keplerian discs with opposite rotations (Norris et al., 1998). Higher resolution maps will be necessary for further analysis since there is a high degree of blending in the spectral features but the existing spot maps only show a few features.

G351.58–0.35
This source is moderately variable. The maser spots have a complex distribution (Walsh et al., 1998).

G351.78–0.54
This source is highly variable. The two peaks show uncorrelated, cyclical behaviour with a characteristic time-scale of about three months. The flares in the peak at 1.21 km.s^{-1} show a delay in the progression of the flare across this peak. The flares start at the higher velocities, with the intensities at lower velocities gradually increasing. The rate at which the flare propagates through the maser feature varies from one flare to another. This behaviour was first reported by MacLeod & Gaylard (1996) and interpreted by them as being caused by a clumpy outflow passing behind an extended maser structure. The maps of Norris et al. (1998) show only two maser spots corresponding to the two velocity peaks. Higher resolution observations would need to be done in order to determine whether the maser features do in fact have an extended structure.

G354.61–0.47
This source is moderately variable, with simultaneous variations at those peaks which have a good S/N.

G359.61–0.24
This source is highly variable. There appear to be flares which occur simultaneously at all features but there are differences in the overall time-series for each peak.

G9.62+0.20
The strongest features in the spectrum show periodic flares with a period of 246 days. This source will be discussed in detail in the following chapters.

G10.47+0.03
This source is not significantly variable to within the noise. However, Menten (1991) reported a peak flux density of 823 Jy for observations carried out in 1991 and the observations of Caswell et al. (1995b) show a peak flux density of 61 Jy, while the peak flux density has stayed around 30 Jy for the duration of the HartRAO monitoring program.

G10.33–0.17
The dominant features show sporadic flares of varying intensities. There is a slight time delay between the flares at 10.725, 11.624 and 12.411 km.s^{-1}. The spot maps of Walsh et al. (1998) show two complexes.

G12.89+0.49
The dominant features show weakly correlated variations on a time-scale of a few weeks. This is similar to the behaviour seen in G340.79–0.10. The maser spots have a complex distribution (Walsh et al., 1998).

G12.68–0.18
All the maser peaks show cyclical, simultaneous variations with a time-scale of approximately 300 days. However, this source does not appear to be periodic.

G12.91–0.26
The two main features at 39.349 and 39.799 km.s^{-1} show simultaneous but moderate variations. The maser spots have a linear distribution but do not have a velocity gradient (Walsh et al., 1998).

G23.01–0.41
The dominant features at 74.193, 74.752 and 75.089 km.s^{-1} show simultaneous short-period flares, but show different long term trends.

G23.44–0.18
The peak at 102.938 km.s^{-1} shows slow variations with a time-scale of 2.5 years. The 96.644 km.s^{-1} feature shows a monotonic increase in intensity.

G35.20–1.74
Some of the peaks show simultaneous flares with a typical time-scale of ap-

proximately four months. The maps of Minier et al. (2000) show two groups of masers with linear structures but neither have a velocity gradient.

G45.07+0.13
This source is not significantly variable.

G52.67–1.09
This source is moderately variable – sometimes decreasing in intensity until it is below the detection limit, but the S/N is too low to analyse the timeseries.

G59.78+0.06
The single feature strong enough for variations to be seen above the noise level has been increasing monotonically in intensity.

W75N
All of the features show simultaneous irregularly spaced flares with differing amplitudes.

G78.12+3.63
This source is moderately variable but the S/N of the observations is too low to analyse the time-series.

3.4.3 Summary of results

There is no general trend observed in the sample. Dissimilar types of behaviour are seen in different sources, and various time-scales are observed:

- Some maser features show a steady increase in intensity eg G305.21+0.21, G287.36+0.64, G328.81+0.63 and G59.78+0.06
- Conversely, G291.27–0.71 shows a steady decrease in intensity.
- Many sources show rapid, low-amplitude changes in intensity, perhaps best described as 'flickering', eg the sources G35.20–1.74, G351.58–0.35 and G12.89+0.49.
- No changes except for the above-mentioned flickering were seen for several years in G174.20–0.08 and G339.88–1.26 until the main feature in G174.20–0.08 started decreasing in intensity, while two features in G339.88–1.26 have started changing in intensity.
- A number of sources appear to have periodic or cyclic variations eg G188.95+0.89, G196.45–1.68, G9.62+0.20, G12.68–0.18.

- The majority of sources are significantly variable but show no predictable pattern eg G213.71–12.60, G345.00–0.22, G10.33–0.17. Flares (high amplitude increases in intensity) tend to last between 2–4 months up to more than a year. The time between flares ranges from weeks to years.
- Visual inspection shows no velocity shifts in any of the maser features to within one spectral channel.

3.5 Discussion

Caswell et al. (1995a) stated that about 75 % of the maser features in their survey sample showed no significant variability and even the most variable features do not have very high amplitude variations. They speculated that this implies that the maser gain is not very dependent on changes in the path length. From the results of the HartRAO study, it is clear that methanol maser variability may be more widespread than initially thought; 61 % of the 436 maser features analysed have a variability index greater than one, indicating significant variability. As in the Caswell et al. (1995a) sample, the ratio of mininum to maximum amplitude for most sources is less than 2, but some sources show spectacular variations with more than a 30-fold increase in intensity (as in the case of G331.13-0.24), or more than 250 times (for NGC6334F).

This behaviour is very similar to that seen in hydroxyl masers. Hydroxyl masers in general show moderate but widespread variability (Smits, 2003), with some notable exceptions such as S269, where the intensity increased by more than 260 times (Clegg, 1992). There is little similarity to the behaviour of water masers, which show extremely strong outbursts with increases in flux density ranging from 40 % to more than 1840 % and have gradual changes in velocity (Brand et al., 2003; Hunter et al., 1994; Liljeström et al., 1989). Water maser spectra also tend to change completely over the years, with some features disappearing completely and new ones appearing. The only methanol maser source that shows this sort of change in its spectral profile is G213.71-12.60 (Mon R2). Interestingly, Smits (2003) reported spectacular flaring in the hydroxyl maser in this source, but there is apparently no correlation with the methanol maser variability (D.P. Smits, private communication in response to a query while the methanol maser was flaring). The source G351.78-0.54 also displays high but uncorrelated variability in the hydroxyl and methanol masers (MacLeod & Gaylard, 1996). The similarity between the hydroxyl and methanol maser behaviour is consistent with the masers arising in similar regions. However, the lack of correlated variations is significant, since it is believed that the masers are radiatively pumped by the same mechanism (Cragg et al., 2002). It could be that the variations are due to extremely localised

changes in path length or density, or there are changes in the level of the seed photons. There is also evidence that hydroxyl masers may be prone to radiative instabilities which lead to short term variations of the order of minutes or hours (Scappaticci & Watson, 1995; Xu et al., 2000), but such rapid variations have not been seen in any of the sources observed from horizon-to-horizon during gain-curve calibration at HartRAO.

The time-scales of variation may shed light on the processes affecting the masers. Short-lived random flares may be due to turbulence in the molecular cloud or changes in the stellar luminosity. It is even possible that the methanol masers also have radiative instabilities. However, it is unlikely that such variations would be correlated across different features, as is seen in many cases. Short-term correlated variations may be due to interstellar diffraction or refraction. However, interstellar scintillation can only occur when the size of the maser region is similar to the scale size of the density fluctuations in the interstellar medium. If the angular separation between maser spots is larger than the scale size, the variations due to interstellar scintillation would not be correlated between different maser spots.

Longer-lived flares, especially those which change the spectral features totally, as in G213.7–12.60, indicate a far greater disturbance of the medium. These may be caused by outflows or shockwaves passing through the masing region. Studies of maser variability also need to be combined with multi-wavelength observations designed to probe the structure of the cloud and find the location of the star exciting the masers. Are the variations linked with outflows? Studies of northern hemisphere sources indicate that outflows can indeed be found towards newly formed massive stars (Beuther et al., 2002). However, the majority of the sources in the HartRAO sample are far south and well out of reach of existing mm and sub-mm interferometers. Higher resolution images of the methanol masers are also necessary in order to understand the relation between the maser morphology and the variations seen.

Sometimes correlated variations across several different features can be seen combined with flares restricted to one feature. This indicates that there are changes taking place locally, such as turbulence, as well as more widespread changes. The correlated variations are likely to originate in changes in the radiation coming from the central region, since spatially separated features are unlikely to be affected in exactly the same way by local turbulence. These sort of variations should be considered in conjuction with high resolution spot maps of the masers.

In general, it can be concluded that methanol masers are significantly variable, and the absence of variability in the past is no guarantee that the source will remain so. The tendency of maser features to drop below the detection limit should also be taken into account when methanol maser surveys or searches are

carried out. An important result is the existance of sources undergoing what look to be periodic variations. To date, no other such variations have been reported in masers in star formation regions. The next chapter will examine these sources in detail.

Chapter 4

Investigation into possible periodic masers

4.1 Introduction

A source can be classified as periodic when it shows variations which repeat at a fixed interval. The first such source discovered during the monitoring programme was G9.62+0.20E, the brightest known 6.7 GHz methanol maser. This source shows strong, well-defined flares at both 6.7- and 12.2-GHz[1] at intervals of 246 days. The flare occurring in October 2000 was imaged using the VLBA at 12.2 GHz. These results will be discussed in a later chapter.

Periodic phenomena are extremely important in astronomy for a number of reasons. There are a limited number of mechanisms which can give rise to periodic variations eg stellar pulsations or orbital motion. The period and amplitude of the variations can then be used to infer the conditions around the embedded star. As indicated above, if it is possible to predict a flare well in advance, intensive observations can be planned to test various hypotheses.

There are a number of sources in the HartRAO sample which may be undergoing periodic variations. The time-series of these sources are analysed in this chapter. The method used to identify periodic masers is described in Section 2. The analysis of likely sources is presented in Section 3 while the possible periodic mechanisms are assessed in section 4. Finally, the conclusions are presented in Section 5.

[1]12.2 GHz monitoring observations and reductions were carried out by M.J. Gaylard

4.2 Identifying periodic masers

The time range of the data analysed in this chapter is from January 1999 to April 2003 (up to the death of our HP1000 control computer). The intervals between observations are irregular, ranging from less than a week to more than two weeks on a few rare occasions. Thus the Nyquist rate can be estimated at two weeks. The minimum period which can be confidently detected is therefore one month. At least two cycles are needed to detect a periodic signal, provided the cycles are very similar. If only two flares with very different profiles are seen, it is not possible to tell whether the maser is periodic/cyclic until a longer time-series is obtained. Therefore, an estimate of the maximum period which can be detected (but not confirmed) in the current data set is of the order of two years.

The data set was searched for periodicity using the following method. First, those features with a variability index high enough to indicate significant variations above the noise were examined by eye. A periodogram, using the discrete Fourier transform (DFT) algorithm of Scargle (1989), was generated for those time-series which appeared to have cyclical variations. A power spectrum was generated for the time-series if the DFT showed any peaks above, or even close to, the 99% confidence level. This is given by

$$z_0 = 4.6 + \ln(N)$$

where N is the number of frequencies searched and the false alarm probability is set to 1% (equation 20 in Scargle, 1982). The frequency range searched was from 0 cycles.yr^{-1} up to 15 cycles.yr^{-1} with 1000 bins, giving $z_0 = 11.5$. The power spectrum was calculated by finding the DFT of the auto-correlation function of the time-series. The autocorrelation function was calculated using the z-transformed discrete correlation function (ZDCF) procedure made available by Alexander (1997). Both the DFT and the power spectrum are shown in order to verify the presence of the period, since spurious peaks can be generated by noisy time-series. The power spectrum should indicate the peak power at a frequency which is also shown to be present in the DFT. The time-series were then folded modulo the period indicated by the power spectrum in order to assess how well the cycles repeat.

Each source will be discussed in detail. For simplicity, only the velocity channels with the peak flux density for each spectral feature are used in this analysis. The flux density across the entire spectral feature was not used since this increases the chance of including emission from other maser spots with similar velocities.

4.3 Notes on individual sources

4.3.1 G9.62+0.20E

The following section is based on a paper by Goedhart et al. (2003)

G9.62+0.20 is a complex of H II regions containing a number of massive young stars at different stages of their protostellar evolution (Hofner et al., 1996). Recent high resolution imaging has shown that the 12.2 GHz methanol masers (Minier et al., 2000) and the strongest of the 6.7 GHz methanol masers (Phillips et al., 1998) may be associated with an ultra-compact H II region (component E in Garay et al., 1993). The spectral index is also consistent with an ionized stellar wind around a young B0 star (Hofner & Churchwell, 1996).

This source shows strong flares at both 6.7- and 12.2-GHz with a period of 246 days. The average spectra of G9.62+0.20E at 6.7 GHz and 12.2 GHz are shown in Figure 4.1a. The features are labelled following the nomenclature adopted by Minier et al. (2002b) for their spot maps at 12.2 GHz. The dominant feature C is strongly variable at both frequencies. The weaker features at 12.2 GHz show no variation within the noise. No features other than those discussed below are seen to flare. Figure 4.1c shows the time-series of two velocity channels at both frequencies. Flares are seen simultaneously at 12.2 GHz and 6.7 GHz in the velocity range 1–2 km.s^{-1} (features A, B and C in Figure 4.1a). The variability appears to consist of a periodic component as well as random variations. The periodic flares can be distinguished from random variability by the following properties: (1) The amplitude of the flare is greater than that of the random variability. (2) The flare occurs simultaneously at 6.7 GHz and 12.2 GHz for features A, B and C.

The weaker feature at -0.14 km.s^{-1} is seen to flare up to 30 days after feature C reaches its maximum (Figure 4.2). It is possible that the corresponding -0.14 km.s^{-1} feature at 12.2 GHz also flares, but the low signal-to-noise ratio (S/N) of the observations at 12.2 GHz makes it impossible to detect any variability above the noise in the weaker features. Figure 4.1d shows the structure of the flares at feature C. The time-series is folded modulo 246 days. While the flares do not repeat exactly, they do follow a common pattern. The start of a flare is characterised by a slow increase in intensity, lasting for about three weeks. Prior to the peak of the flare the intensity increases rapidly, doubling within a week at 12.2 GHz. The duration of the maximum intensities is short – of the order of a week. The flare then slowly decays, with the minimum intensity reached about three months after the maximum. No shifts in the velocity of the features have been observed. An ephemeris for the start of the flare as

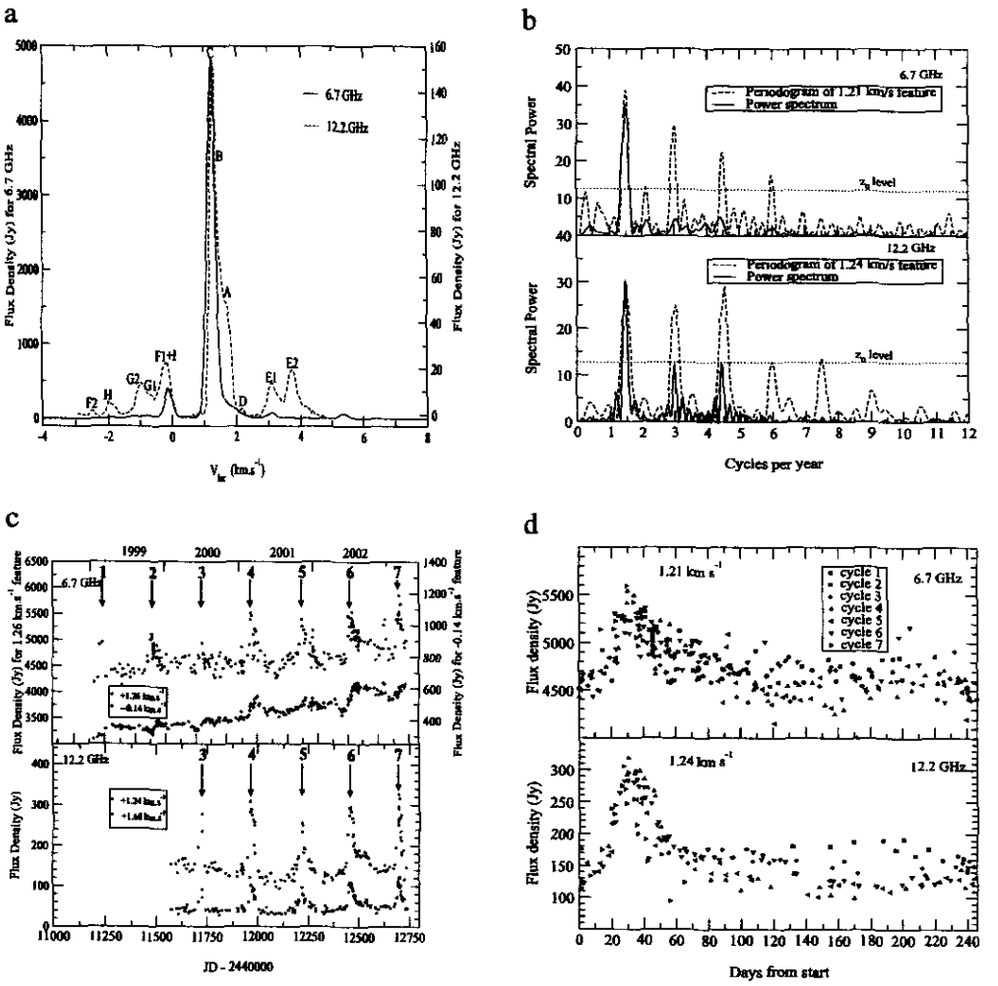

Figure 4.1: Time-series analysis of G9.62+0.20E. a. Time-averaged spectra of G9.62+0.20E. The solid line is the 6.7 GHz spectrum and the dashed line is the 12.2 GHz spectrum. b. Periodogram and power spectrum of the main velocity feature at 6.7 and 12.2 GHz. c. Time-series of various velocity channels. The upper panel shows the 6.7 GHz data for features C (peaking at 1.21 $km.s^{-1}$) and the combination of features F1 and I (peaking at -0.14 $m.s^{-1}$). The lower panel shows the 12.2 GHz data for feature C (peaking at 1.24$km.s^{-1}$) and feature A (peaking at 1.68 $km.s^{-1}$). The numerals indicate the major flares observed. d. The time-series is folded at intervals of 246 days from the start of monitoring. The top panel shows the 12.2 GHz data while the bottom panel shows the 6.7 GHz data.

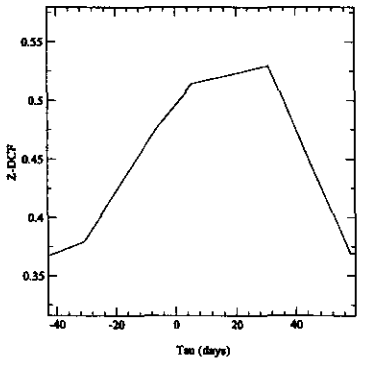

Figure 4.2: Cross-correlation between features at 1.26 km.s^{-1} and -0.14 km.s^{-1} for G9.62+0.20E.

shown in Figure 4.1d is

$$JD = 2451195 + 246 \times N$$

where $N = 6$ for the flare in February 2003.

4.3.2 G188.95+0.89

This maser source is found in the high mass star formation region also known as S252 or AFGL 5180. The UC H II region associated with the methanol masers is unresolved in the observations of Kurtz et al. (1994). The spot maps of Minier et al. (2000) show a linear morphology but there is no velocity gradient across the spots. The masers are coincident with the near-infrared source NIRS 1 (Tamura et al., 1991) which may be powering a bipolar outflow (Davis et al., 1998).

The averaged spectrum as well as upper and lower envelopes are shown in Figure 4.3a. This source appears to have quasi-periodic variations with a period of 391 days (Figure 4.3b). Figure 4.3c shows the time-series of the various maser features. The changes in flux density appear to occur simultaneously at all the features. The time-series for the variable peaks are folded modulo 391 days in Figure 4.3d. The variations are not sinusoidal, but look more like a cycloid since there is an abrupt increase in intensity after the minimum of the cycle is reached. Unlike G9.62+0.20E, the variations in intensity cannot be described as flares since they are not of high amplitude or short duration. Since the flux density is at a higher value for most of the cycle, it may be that the event of interest is in fact the *decrease* in intensity. An ephemeris for the times of minimum intensity is as follows:

$$JD = 2451589 + 391 \times N$$

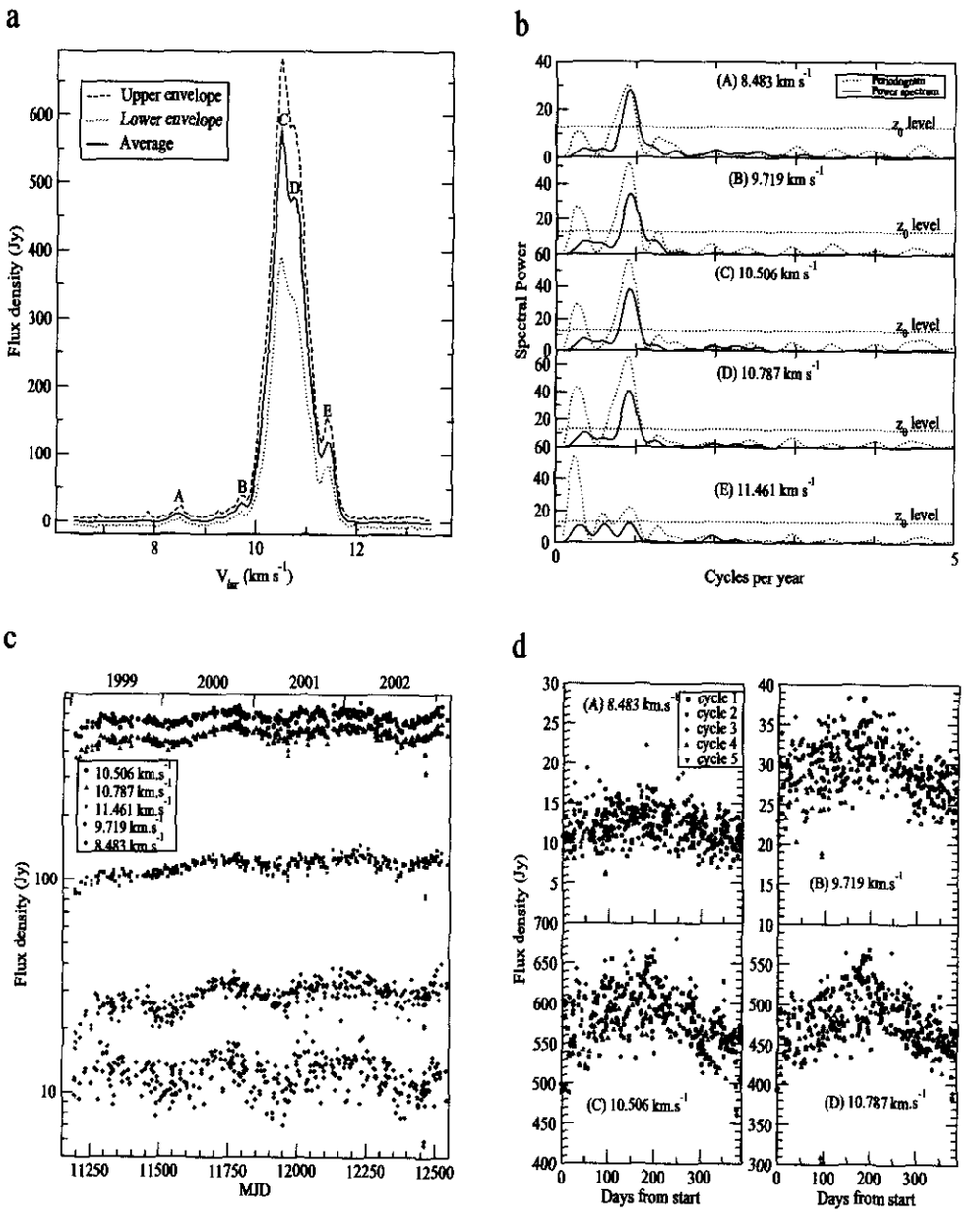

Figure 4.3: Time-series analysis of G188.95+0.89. a. Averaged spectrum and envelopes. b. Periodogram and power spectrum. c. Time-series for selected channels. d. Time-series folded modulo 391 days, after the linear trend was removed.

where $N = 3$ for May 2003.

4.3.3 G196.45-1.68

No UC H II region has been found at the location of the methanol masers (Kurtz et al., 1994) even though the methanol masers are found towards a molecular cloud and the evolved bipolar H II region S269 (Godbout et al., 1997). This source shows the typical triple-peaked spectral profile predicted for masers in a disc (Wallin et al., 1998). The averaged spectrum as well as upper and lower envelopes are shown in Figure 4.4a. Fourier analysis of the time-series (Figure 4.4b) indicates a long period variation of 668 days, so only slightly more than two cycles have been observed so far. However, the time-series of the most variable feature repeats very well (Figure 4.4d) and the power spectrum shows a strong signal. A longer time-series is necessary before the periodicity can be confirmed.

This is the only source in the sample for which it is possible to fit a sinusoid with a high correlation coefficient to the time-series (Figure 4.4c). The results of the fit to a curve of the form

$$A = a_0 \sin(2\pi\omega t + \phi\pi) + a_1 \tag{4.1}$$

are summarised in Table 4.1.

Interestingly, the weakest peak (feature C) shows the greatest degree of variation and gives the best fit to a sine curve. The data are somewhat noisy, but it seems as though there is a slight difference in phase in the sine fits. Figure 4.5 shows the results of a cross-correlation between the various features. Features A and B appear to vary simultaneously, while C lags by 8 days. Examination of the relation between the spatial distribution and the phase lags could lead to some insight into the propagation of the variation. Minier et al. (2000) have imaged this source using the VLBA. Unfortunately, the observations were done when the masers would have been at minimum intensity. In addition, feature C was almost totally resolved out (V. Minier, priv. comm), therefore observations with the shorter baselines of the EVN or MERLIN will have to be done in order to image the most variable feature.

An ephemeris for the times of maximum intensity is as follows:

$$JD = 2451644 + 668 \times N$$

where $N = 1$ for year 2002.

Insufficient cycles have been observed to be sure that this source is periodic, but the results seem quite promising.

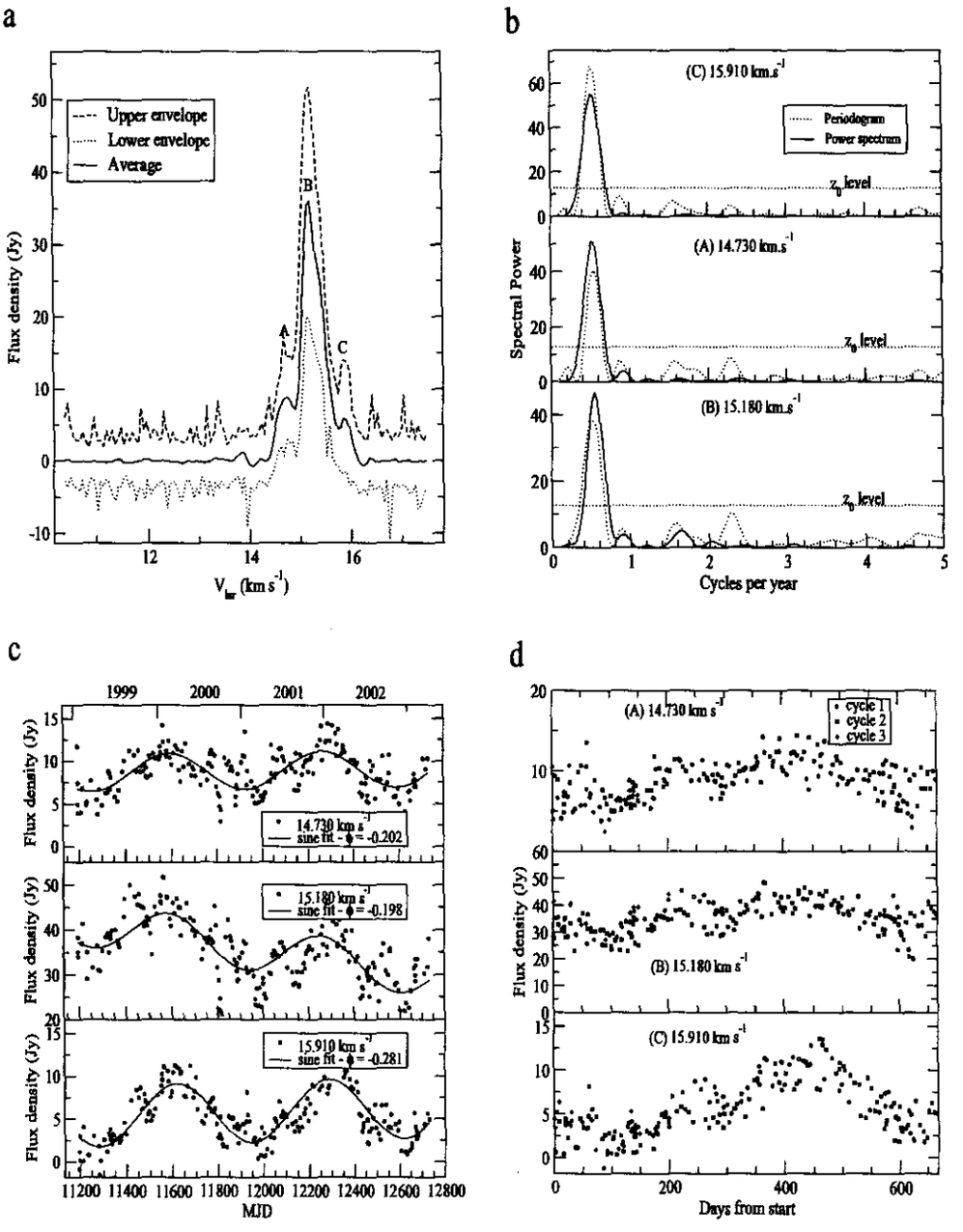

Figure 4.4: Time-series analysis of G196.45-1.68. a. Averaged spectrum and envelopes. b. Periodograms and power spectra. c. Sine-fit to time-series of selected channels. d.Time-series folded modulo 668 days after the linear trends were removed.

Table 4.1: Results of sinusoidal fit to light curves from G196.45-1.68

velocity ($km.s^{-1}$)	a_0 (Jy)	ϕ	cor. coeff.
14.730	2.2	-0.201	0.64
15.180	5.1	-0.198	0.73
15.910	3.6	-0.281	0.81

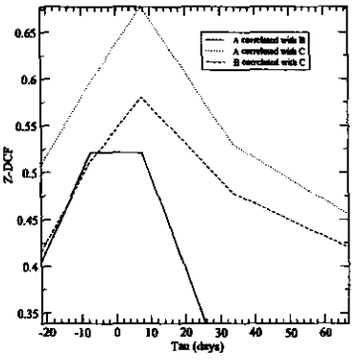

Figure 4.5: Cross-correlation between time-series for different features in G196.45-1.68

4.3.4 G312.11+0.26

The averaged spectrum as well as upper and lower envelopes are shown in Figure 4.6a. This source appears to have a low-amplitude variation of 365 days(Figure 4.6b). Feature D is the only maser with high enough S/N for the analysis to be reliable. The time-series (Figure 4.6) is very noisy and the coincidence with a one-year period makes this result suspect. The folded time-series (Figure 4.6d) shows that there is a large scatter in the variations from cycle to cycle. Fourier analysis of the pointing corrections as a function of time does not show any periodicity, neither is there any correlation between the variation in the maser features and the pointing corrections. Observational effects are unlikely to cause this periodic variability, otherwise we would see the same effect in other sources in the sample. Even so, the variation may not be intrinsic to the source eg refraction from a nearby interstellar cloud with noticeable parallax.

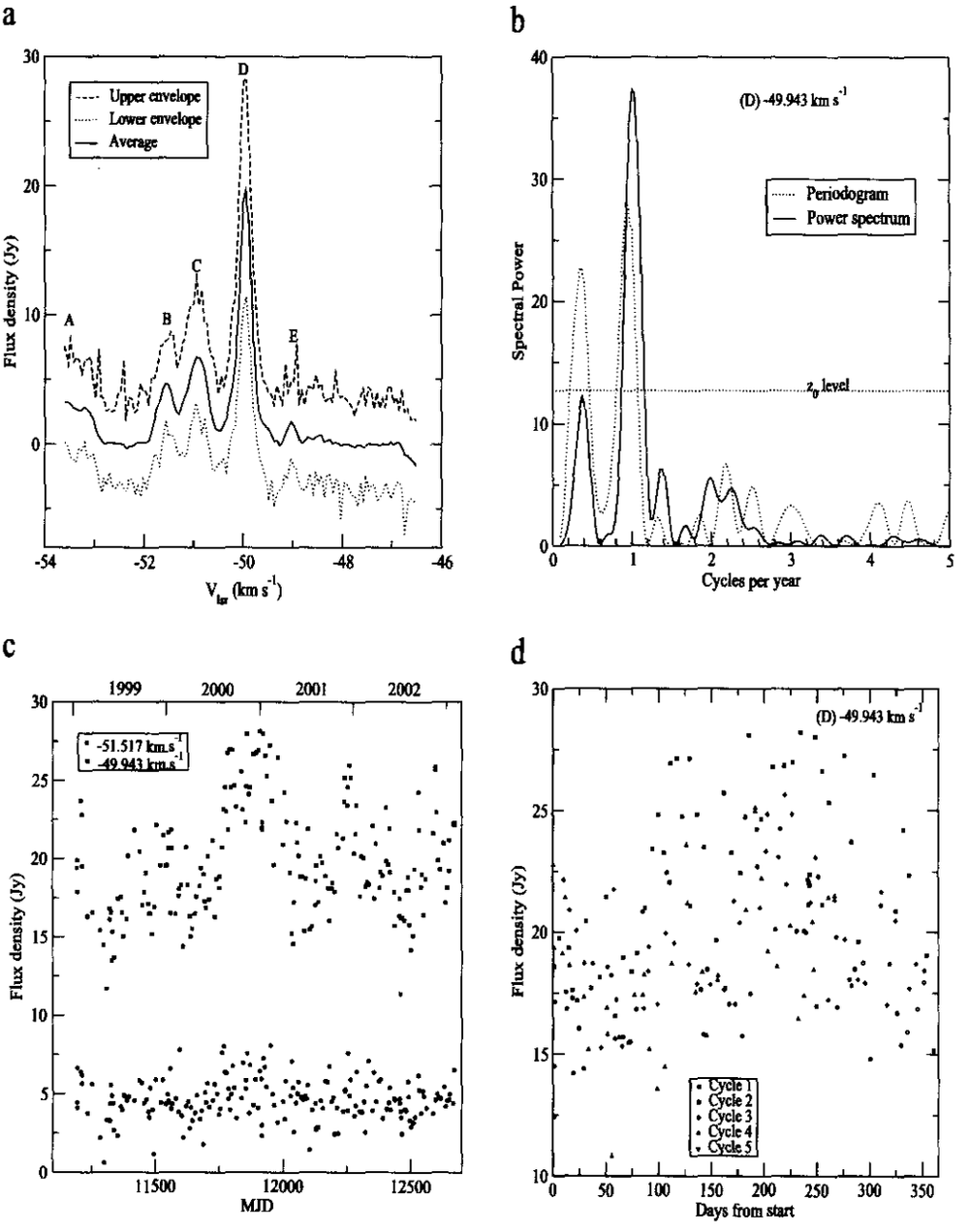

Figure 4.6: Time-series analysis of G312.11+0.26. a. Averaged spectrum and envelopes. b. Periodogram and power spectrum. c. Sine-fit to time-series of selected channels. d. Time-series folded modulo 365 days after the linear trend was removed.

4.3.5 G316.64-0.09

Phillips et al. (1998) found that this source has a complex, curved morphology with a velocity gradient across the maser spots but they did not detect any H II region.

The averaged spectrum as well as upper and lower envelopes are shown in Figure 4.7a. The features D, E, F, G and H show simultaneous quasi-periodic variations with a period of 448 days (Figures 4.7 b and c). The variations in feature H have the greatest amplitude, but the flares do not repeat exactly (top panel in Figure 4.7d). An initial analysis with data up to September 2002 indicated that the flares were possibly periodic, but additional data showed that the maser failed to flare as expected in the fourth cycle. Further monitoring of this source is advisable in order to see if any periodic behaviour persists beyond the fourth cycle.

4.3.6 318.95-0.20

The averaged spectrum as well as upper and lower envelopes are shown in Figure 4.8a. Like G312.11+0.26, this source shows a low amplitude variation with a period of 365 days (Figures 4.8 b and c). The variations occur simultaneously at all the features. The signal at 1 cycle per year is barely above the z_0 confidence level, whereas there is a strong signal in the power spectra for the other periodic sources discussed in this chapter. The case for periodicity in this source is not very convincing, therefore further monitoring observations will be necessary in order to confirm this.

4.3.7 G328.25-0.53

The spectrum shown in Figure 4.9a is in fact composed of two different sources: G328.24-0.55 and G328.25-0.53 (Caswell 1995). Phillips et al. (1998) found that these masers form two clusters on either side of an UC H II region. They speculate that this distribution could indicate the presence of shock fronts from a bipolar outflow, or the masers could be on either side of a thick disc. Fortunately there is a large velocity difference between the two clumps, so it is possible to monitor both sources in the HartRAO beam. The features D, E, F and G (G328.25-0.53) show simultaneous periodic variations with a period of 217 days (Figure 4.9b). Features D, E and G show weak flares apparently coincident with those in feature F (Figure 4.9c), but, since the amplitudes of the flares are very low and other trends dominate, the power spectrum does not show any peaks at 217 days. However, cross-correlation of the time-series

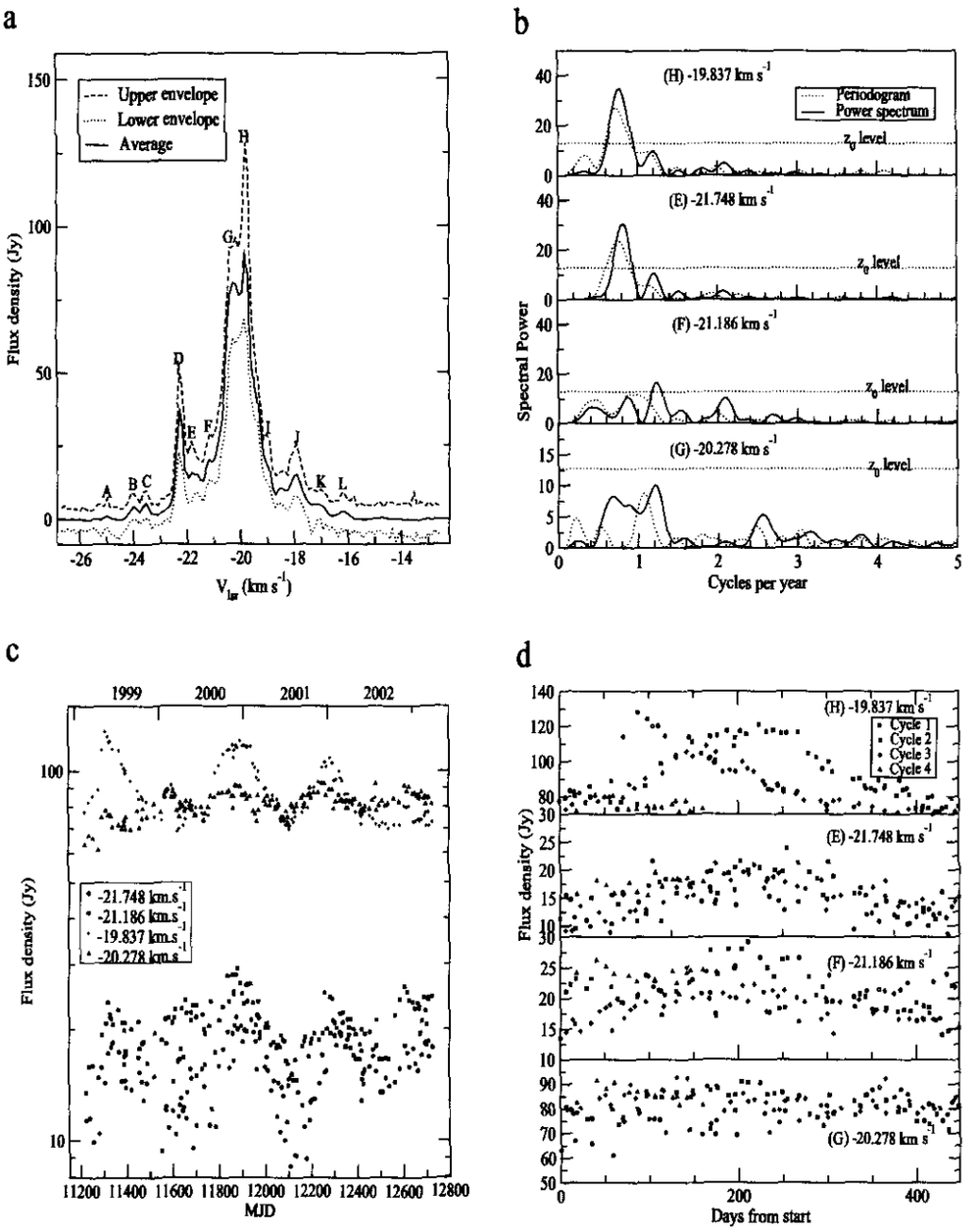

Figure 4.7: Time-series analysis of G316.64-0.09. a. Averaged spectrum and envelopes. b. Periodograms and power spectra. c. Time-series of selected channels. d. Time-series folded modulo 448 days.

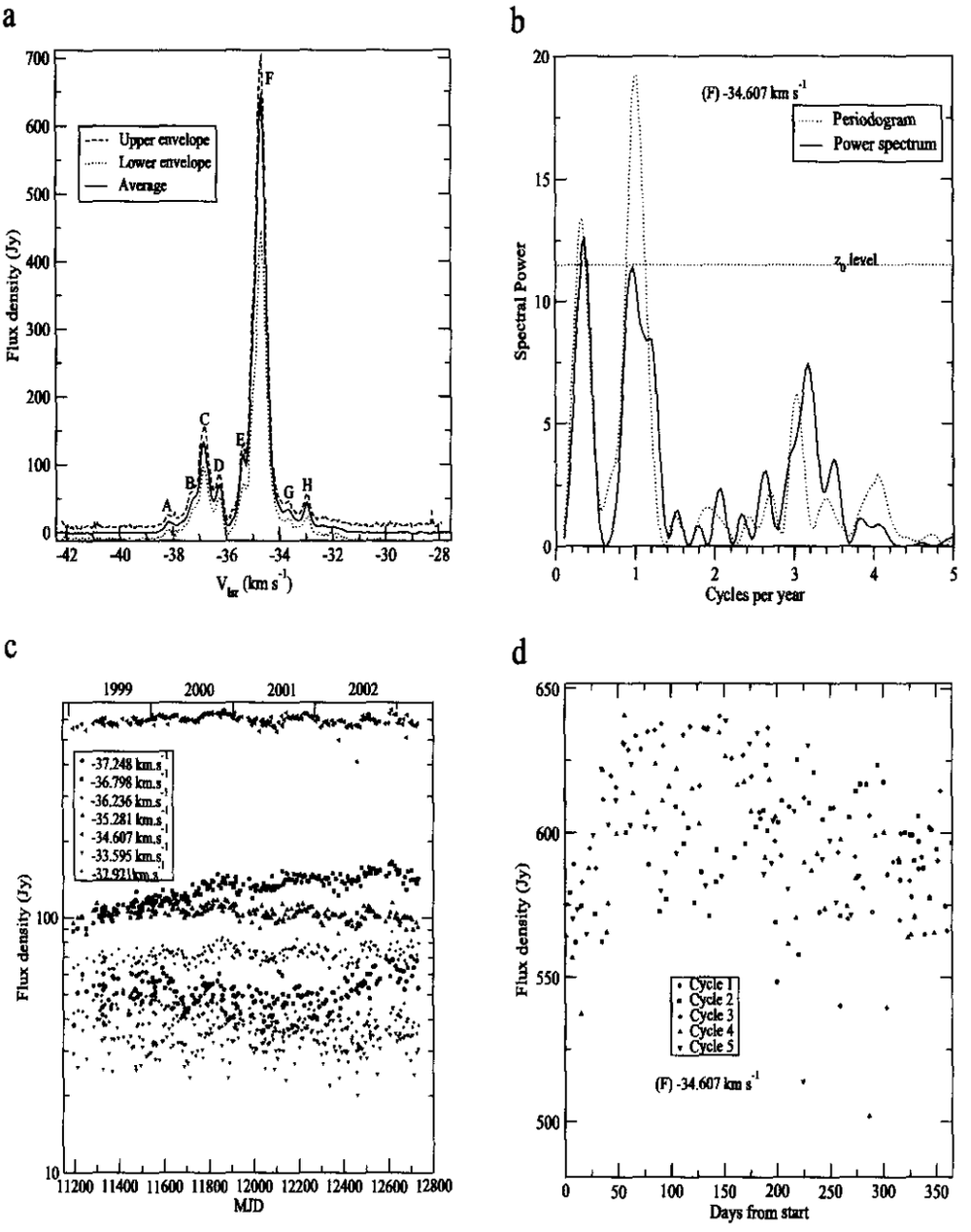

Figure 4.8: Time-series analysis of G318.95-0.20. a. Averaged spectrum and envelopes. b. Periodograms and power spectra. c. Time-series of selected channels. d. Time-series folded modulo 365 days.

of these features with that of F (Figure 4.10) shows a strong correlation with no delay. The variations of features in source G328.24-0.55 do not correlate with those in feature F, which suggests that if both maser groups are being pumped by the same star, the cause of the periodic variations is localised to the one clump of methanol masers. An ephemeris for the start of the flare is as follows:

$$JD = 2451153 + 217 \times N$$

where $N = 7$ for early in year 2003.

4.3.8 G331.13-0.24

The averaged spectrum as well as upper and lower envelopes are shown in Figure 4.11a. The feature C in this source is the second most variable in the entire sample, with a variability index of 98. The DFT (Figure 4.11b) indicates that there are two groups of masers showing two different periods of variation. Features A, B and C show flares at intervals of 470 days. Some of the features drop below the detection limit for most of the cycle. Features D, E and F have flares at intervals of 572 days. These features are stronger than those of the first group and stay above the detection limit for the entire cycle.

The spot maps of Phillips et al. (1998) show two linear groups of spots, which correspond to the grouping that we see in the periods. On this basis, the two groups of masers are treated as separate sources, designated G331.13-0.24A and G331.13-0.24B. An ephemeris for the start of the flare for G331.13-0.24A is as follows:

$$JD = 2451422 + 481 \times N$$

where $N = 2$ for year 2002.

An ephemeris for the start of the flare for G331.13-0.24B is:

$$JD = 2451459 + 572 \times N$$

where $N = 2$ for early in year 2002.

Further monitoring observations are necessary to confirm the periodicity in these sources, but the strong signal in the power spectra of the time-series is promising.

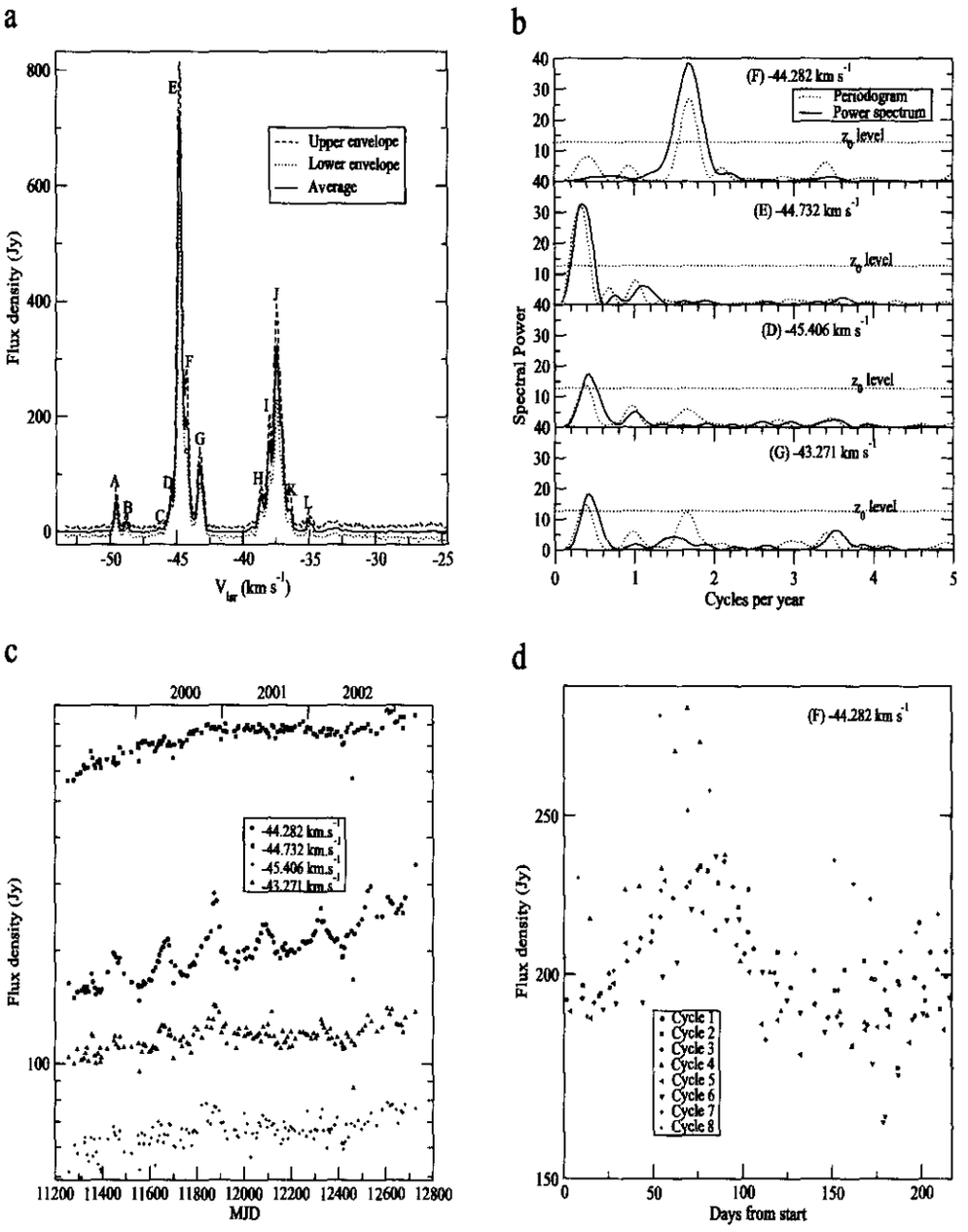

Figure 4.9: Time-series analysis of G328.25-0.53. a. Averaged spectrum and envelopes. b. Periodograms and power spectra. c. Time-series of selected channels. d. Time-series folded modulo 217 days.

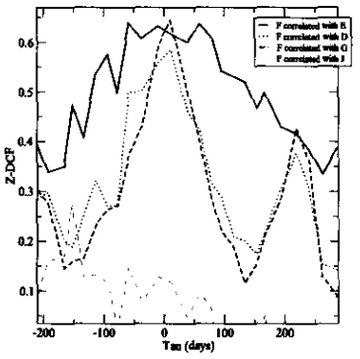

Figure 4.10: Cross-correlation between time-series for G328.24-0.55

4.3.9 G338.93-0.06

The averaged spectrum with upper and lower envelopes are shown in Figure 4.12a. The feature at -41.99 km.s^{-1} displays the shortest period variability in the sample with a period of 132 days(Figure 4.12b). The time-series for both peaks is shown in Figure 4.12c, along with a sinusiodal fit to the periodic time-series. The variations are not sinusoidal, but are very similar to those seen in G188.95+0.89 as can be seen in the folded time-series Figure 4.12d.

An ephemeris for the start of the flare for G338.93-0.06 is as follows:

$$JD = 2451144 + 132 \times N$$

where $N = 12$ for April 2003.

4.3.10 G339.62-0.12

The averaged spectrum as well as upper and lower envelopes are shown in Figure 4.13a. The features A, B, C, D and E have simultaneous flares with a period of 202 days (Figure 4.13b). Only the time-series of the periodic features are shown in Figure 4.13c in order to avoid the plot becoming too complicated. Feature E is below the detection limit most of the time, while F, G and H do not show periodic flares. Other, non-periodic, flares are seen simultaneously at D and E. Walsh et al. (1998) found that the maser spots lie in a curve but do not show a velocity gradient. An ephemeris for the start of the flare for G339.62-0.12 is as follows:

$$JD = 2451342 + 202 \times N$$

where $N = 6$ for year 2002.

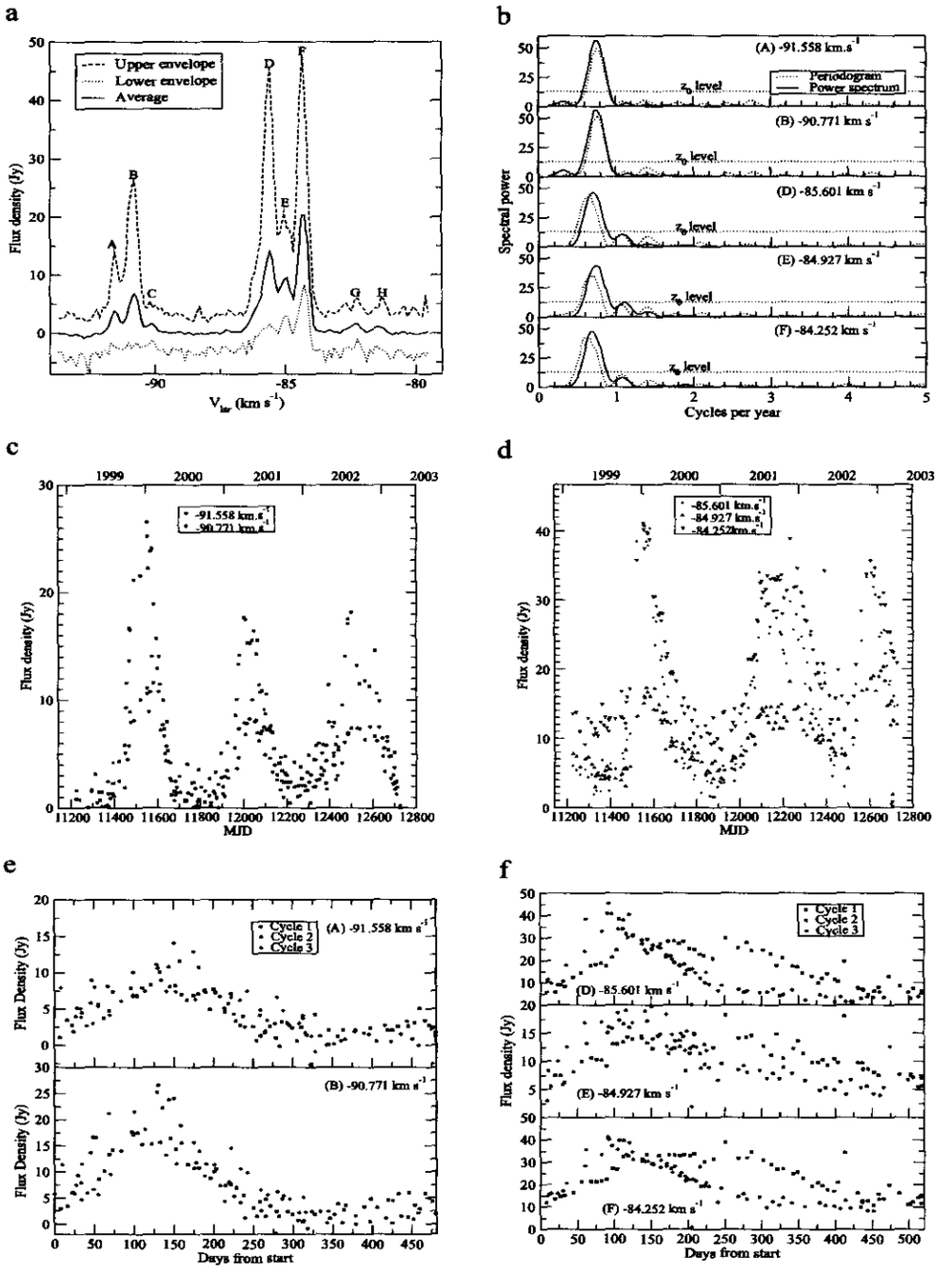

Figure 4.11: Time-series analysis of G331.13-0.24. a. Averaged spectrum and envelopes. b. Periodograms and power spectra. c. Time-series of channels at features A and B . d. Time-series of channels at featured D, E and F. e. Time-series folded modulo 481 days. f. Time-series folded modulo 521 days.

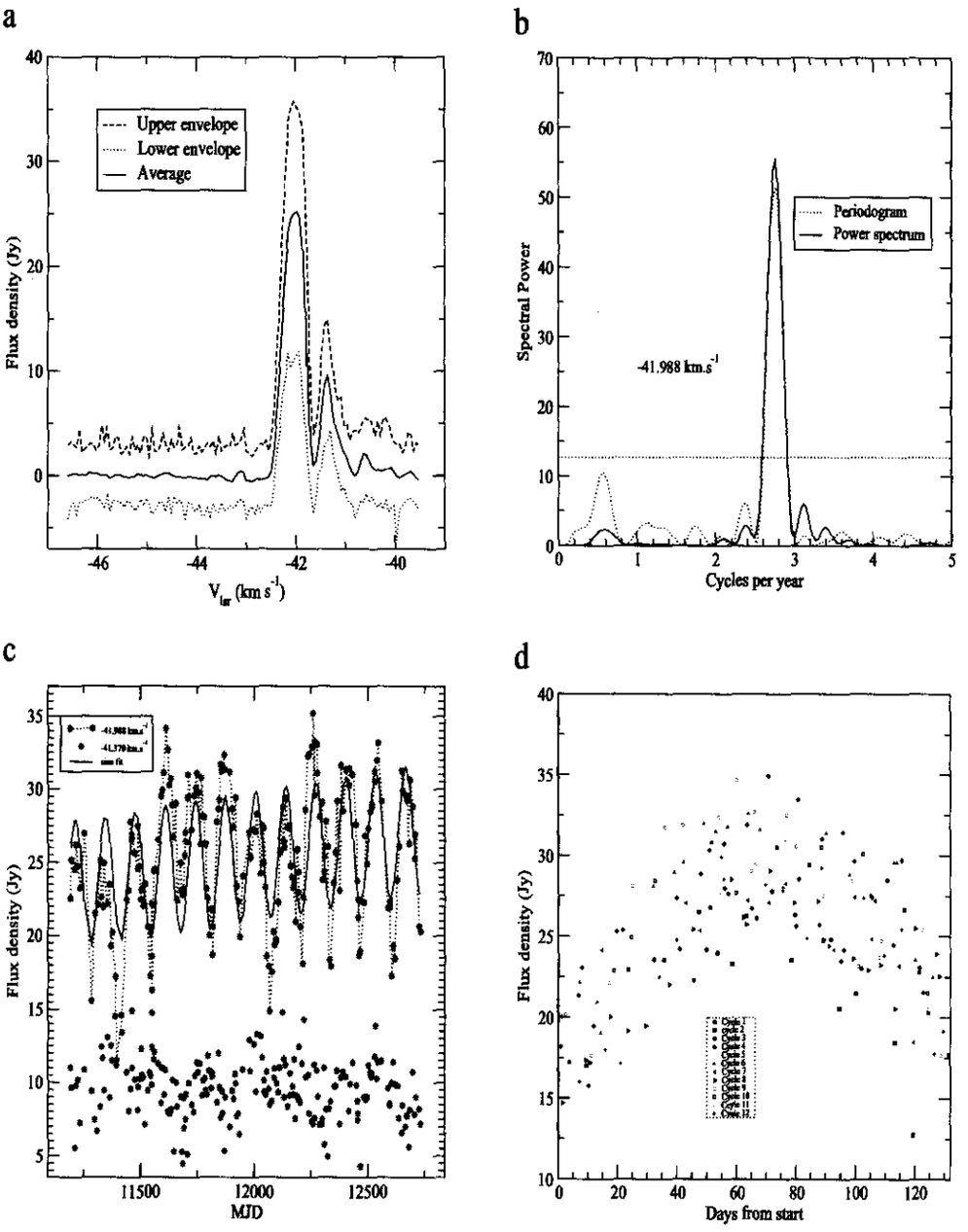

Figure 4.12: Time-series analysis of G338.93-0.06. a. Averaged spectrum and envelopes. b. Periodograms and power spectra. c. Time-series of selected channels. d. Time-series folded modulo 132 days.

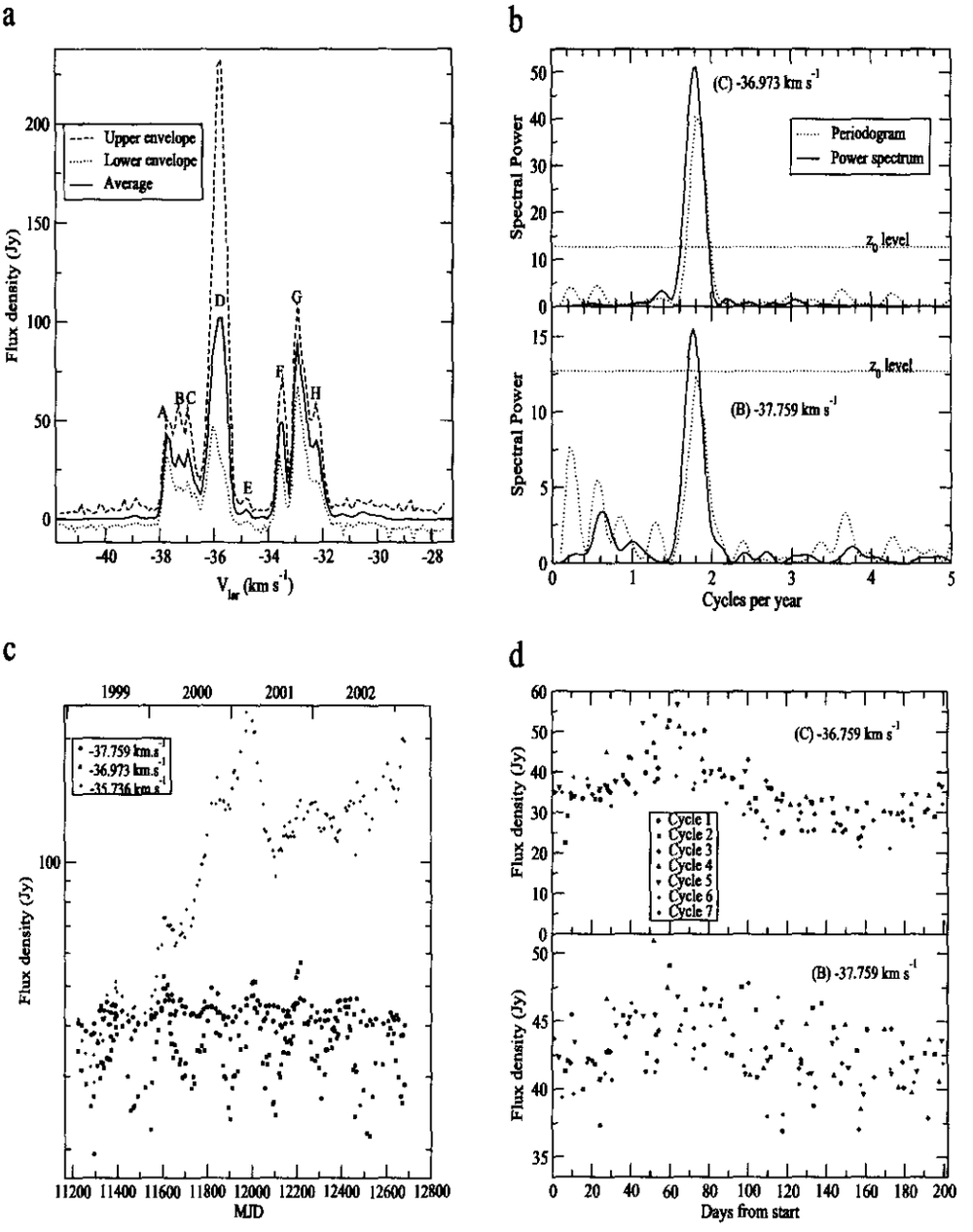

Figure 4.13: Time-series analysis of G339.62-0.12. a. Averaged spectrum and envelopes. b. Periodograms and power spectra. c. Time-series of selected channels. d. Time-series folded modulo 202 days.

Table 4.2: Possible periodic masers

Source	RA (B1950)	Dec (B1950)	Period (days)	cycles observed	σ_{res} (Jy)	σ_m (Jy)	$\frac{\sigma_{res}}{\sigma_m}$
G188.95+0.89	06:05:53.5	21:39:02.0	391	3.9	28.83	16.05	1.7
G196.45-1.68	06:11:47.1	13:50:34.0	668	2.3	1.56	0.41	3.8
G312.11+0.26	14:05:02.2	-60:58:48.0	365	4.0	3.02	0.63	4.8
G316.64-0.09	14:40:31.6	-59:42:40.0	448	3.4	11.97	2.27	5.3
G318.95-0.20	14:57:03.8	-58:47:01.2	365	4.2	21.52	14.08	1.5
G328.24-0.55	15:54:06.1	-53:50:47.0	217	6.7	14.58	4.67	3.1
G331.13-0.24 A	16:07:10.8	-51:42:29.0	481	3.1	2.83	0.35	8.1
G331.13-0.24 B	16:07:10.8	-51:42:29.0	520	2.8	5.93	0.46	12.9
G338.93-0.06	16:39:36.5	-46:00:05.0	132	11.6	2.91	0.76	3.8
G339.62-0.12	16:42:26.5	-45:31:18.0	202	7.2	4.10	1.17	3.5
G9.62+0.20E	18:03:15.9	-20:31:52.9	246	6.2	163.31	143.66	1.14

4.4 Summary and discussion

The cycles of variation do not appear to repeat exactly each time for any of the sources. Some of this variation may be due to calibration errors and noise, but it may be that the sources are only quasi-periodic or that there are other disturbances occurring independently of the periodic phenomena. The following calculations are a crude means of assessing the scatter from one cycle to another relative to the expected errors. Figure 4.14 shows the results of a 9^{th}-order polynomial fit to the folded time-series of each source. No assumptions about the shape of the waveform are made. The intent is simply to find an average curve such that the mean of the residuals is zero. The fitted curve as well as the residuals are shown. If the cycles repeat very closely, the standard deviation of the residuals should be close to the uncertainty σ_m calculated in the previous chapter. The results are summarised in Table 4.2. From this it would appear that the behaviour of G188.95+0.89, G318.95-0.20 and G9.62+0.20E repeats to less than twice the expected noise. The cycles in G338.93-0.06 also appear, on visual inspection, to repeat reasonably well, even though the scatter in the cycles is 3.8 times the expected error. Visual inspection of the folded time-series shows that the flares in G316.64-0.09, G331.13-0.24A and G331.13-0.24B do not follow the same pattern each time, even though it is clear that there is some sort of disturbance occurring at regular intervals.

4.4.1 Periodic mechanisms in star formation regions

The environment in which methanol masers are found is complex, with a number of factors that could affect the masers. The energy for pumping the masers must ultimately come from the central star(s). The central star may be surrounded by a rotating, inhomogenous accretion disc, which may also be trig-

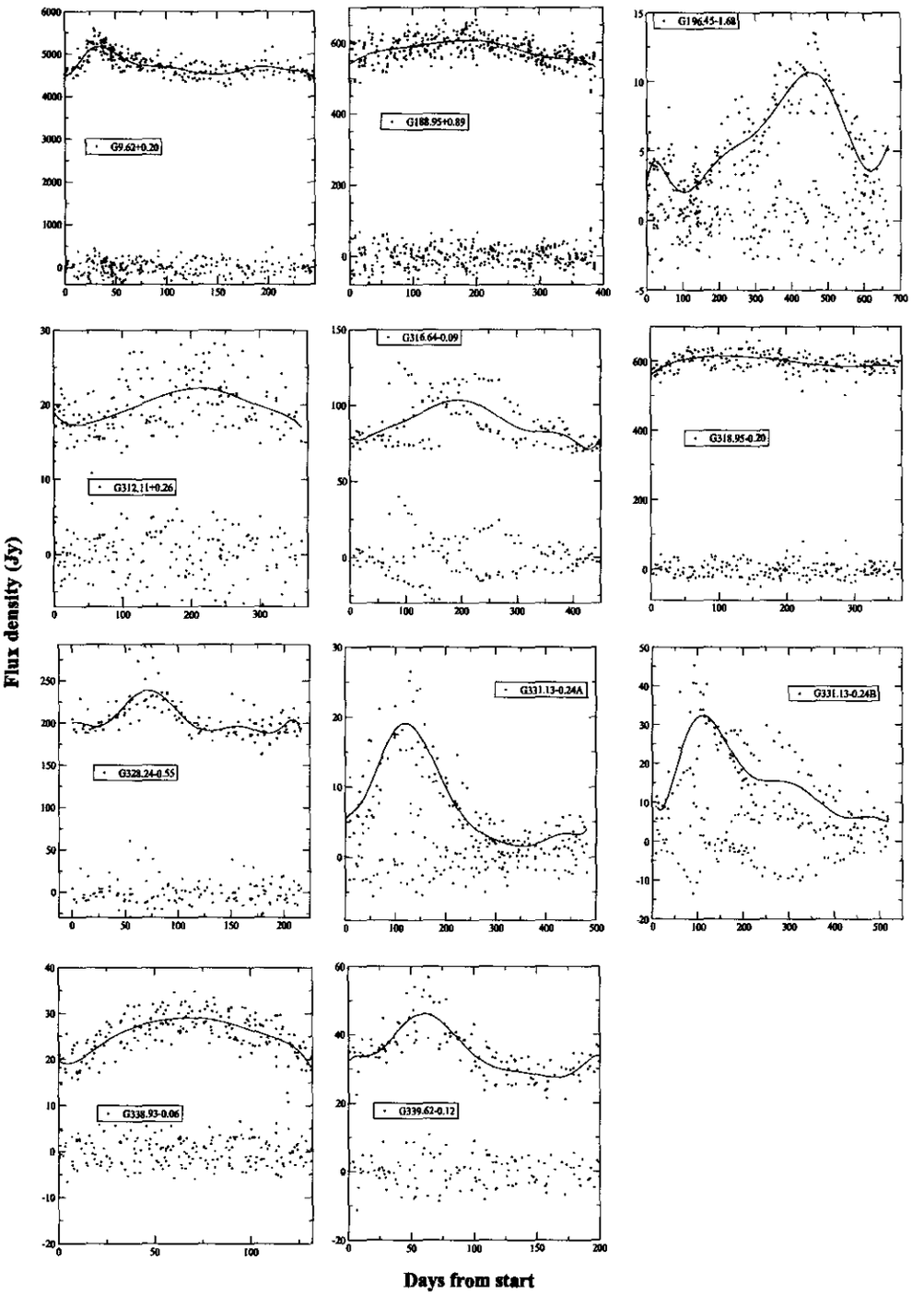

Figure 4.14: Polynomial fits to folded time-series of periodic masers. The black stars are the original data, the solid line is the fit and the red stars are the residuals of the fit.

gering outflows; the outflows may be sporadic, or the jets may be precessing. Massive stars have H II regions, which may be expanding. Shocks may exist at the interface between the H II region and the surrounding molecular cloud. These shocks could lead to the sudden release of methanol from ice on the surface of dust grains. In addition, the source of the seed photons for the masers may be variable. The interaction of all these elements may give rise to complex behaviour in the light curves of the methanol masers.

Pulsations intrinsic to central star

The most common cause of periodic variations in stars is due to pulsations caused by the κ (helium opacity) mechanism. The β Cephei instability strip affects O8 to B6 stars approaching and on, the ZAMS (Deng & Xiong, 2001). However, the periods of these stars are between 0.1 – 0.6 days, which is much less than any of the periodic variations seen in the methanol masers. Examination of the classes in the General Catalogue of Variable Stars (Kholopov et al., 1985) show that the only pulsating stars with the appropriate periods are Miras. These are evolved stars and therefore unlikely to be the cause of the variations.

Stellar rotation

Another cause of periodic variations in stars is rotation of the star, with non-uniform surface brightness. However, O and B type stars have extremely rapid rotational velocities – on the order of 400 km.s^{-1} (Lang, 1992), which gives rotational periods between 0.5 and 2 days. Again, these periods are far too short to be related to the variations in the masers.

FU Orionis-type outbursts

The young star FU Orionis is the prototype of a class of YSOs that experience episodic outbursts due to high disc accretion rates and instabilities in the disc accretion. The duration of these outbursts is of the order of decades and the interval between outbursts is believed to be thousands of years (Kenyon et al., 2000, and references therein). The time-scales involved here are far too great to present a feasible explanation of the methanol maser flares. However, the sources known thus far are low mass stars. It is possible that the mechanism may be accelerated in massive stars.

Disc-outflow systems

The numerical simulations of Yorke & Sonnhalter (2002) showed that massive stars can form from disc accretion collapse of molecular cloud clumps. The simulations of Durisen et al. (2001), Yorke & Sonnhalter (2002) and Ouyed et al. (2003) showed that the accretion disc developes a rotating spiral density pattern. The outflows themselves could cause variations with the appropriate periods; Ouyed et al. (2003) found that the outflow jets can develop a corkscrew structure or a wobbling motion. The rotation rate of the corkscrew is dependent on its distance from the origin, with the minimum rotation rate at approximately 85 days for a B0 star (the timestep t in the Ouyed et al. (2003) simulation is 0.53 days for a B0 star). The simulation does not extend out far enough from the origin to show the further evolution of the jet, but it seems likely that the helix of the jet will widen and slow down enough to have a rotation time-scale of a few hundred days. A change in the disc velocity profile at the boundary between the disc and jet leads to a precessing jet instead.

The methanol maser source G78.12+3.63 shows clear evidence of a disc-outflow system (Cesaroni et al., 1999) and G45.07+0.13 has a face-on bipolar outflow (Hunter et al., 1997). However, neither of these sources show any periodic variations. In fact, G45.07+0.13 does not show any variations at all to within the noise. This could be explained by the highly directional nature of masers: if the variations are arising in the seed photons and these are propagating from the disc perpendicular to the line of sight, no variations are seen. This explanation does not work in the case of G78.12+3.63 since its outflow lies almost in the plane of the sky, but it is offset by a significant distance from the molecular core driving the outflow (Minier et al., 2001) and may therefore be associated with a different source.

Binary systems

More than 50 % of optically visible stars of types O9 to M appear to have companions (Abt, 1979; Halbwachs, 1983; Abt, 1983). Poveda et al. (1982) showed that the incidence of binary and multiple systems may be closer to 100 % once observational limitations have been taken into account. A recent study of the multiplicity in Herbig-Haro sources gives a binary frequency between 79% and 86%, with half of the systems higher order multiples (Reipurth, 2000). Simulations of accretion and collisions in stellar clusters (Bonnell & Bate, 2002) indicate that binary systems can form through three-body interactions. In addition, it is known that high mass stars tend to form in clusters (Clarke et al., 2000). Therefore there is a strong possibility that the central star exciting the masers could have a companion. The calculations of Reipurth (2000) indicate that in the case of multiple systems in low mass stars, the orbital companion

Table 4.3: Keplerian orbital radii for objects orbiting a B0 star with the specified periods.

Source	Period (days)	semi-major axis (AU)
G188.95+0.89	391	2.71
G196.45-1.68	668	3.88
G316.64-0.09	448	2.97
G328.24-0.55	217	1.83
G331.13-0.24 A	481	3.10
G331.13-0.24 B	520	3.28
G338.93-0.06	132	1.32
G339.62-0.12	202	1.75
G9.62-0.20	246	1.99

could modulate the accretion flow, leading to periodic or quasi-periodic mass ejections in the outflow. Thus an unstable orbital system could drive quasi-periodic variations.

The spectral types for most of the sources discussed in this chapter are not known with a high degree of certainty. G9.62+0.20 is is one of the better-studied star formation regions, with the observations of Hofner et al. (1996) indicating the central star exciting the methanol masers is likely to be a B0 star. Using this as a guide-line for the typical stellar mass of the central star, and assuming that the orbiting companion is much less massive, the Keplerian orbits for an object orbiting a 17.5 $M_{\odot}$ star are tabulated in Table 4.3. The semi-major axes derived cover the range 1–4 AU. Since the radius scales as the cube-root of the mass of the central star, even a 10-fold increase in stellar mass would only double the calculated orbital radius. Therefore the observed periods imply very closely orbiting binaries. These orbits could also apply to clumps in a rotating accretion disc. Orbiting clumps that gradually dispersed could explain the behaviour seen in G316.64-0.09, where the amplitude of the flares decreased with each cycle.

4.5 Conclusions

Eight candidates with a strong probability of being intrinsically periodic have been found. Deviations from strict periodicity can be explained by stochastic variations in the maser environment. This appears to be the first reported incidence of periodic masers in star formation regions. Another candidate, G316.64–0.09, may be quasi-periodic. Further observations are neces-

sary to confirm the periodicity in the cases of G196.45-1.68, G316.64-0.09 and G331.13-0.24. Two sources, G312.11+0.26 and G318.95–0.20, have a weak 365 day modulation, which may be due to a parallax effect where the radiation is refracted by a nearby interstellar cloud.

Since the cycles repeat very well, the integrity of the maser region is maintained. Thus destructive events, such as shocks passing through the maser region, can be ruled out. The most likely scenario causing the periodicity appears to be a binary system and/or a disc-outflow system. The other possibilities for periodic variations do not have the appropriate time-scales. It is not possible to pin-point the exact cause of the variations with the existing data.

The results of a project to image the masers in G9.62+0.20E during the course of a flare will be presented in the next chapter.

Chapter 5

VLBA imaging of G9.62+0.20E during a flare

5.1 Introduction

As was discussed in the previous chapter, a number of masers in the HartRAO monitoring sample have been found to undergo periodic flares. The source G9.62+0.20E has strong flares at both 6.7- and 12.2 GHz. There appears to be a time delay in the flare across different features but the velocity overlap of some maser spots means that the spectral line observations cannot give us much information on the spatial propagation of the flare. Since this source is reasonably strong at 12.2 GHz and the flares are even more pronounced than at 6.7 GHz, the VLBA was judged to be the ideal instrument for imaging the maser components during a flare. Seven observations were done during the period of October to December 2001.

The observations and reduction method will be described in Section 2. The results are presented in Section 3 and discussed in Section 4. The conclusions are presented in Section 5.

5.2 Observations

The aim of the observations was to image the methanol masers in G9.62+0.20E and study the impact of the flare on the milliarcsecond structure of the masing regions. Due to the high demand on the VLBA, it was not possible to request a large number of closely spaced observations. Therefore the requested observing

Table 5.1: Timing of the VLBA observations

Observation	Date	Day of cycle
A	11-10-2001	14
B	18-10-2001	21
C	22-10-2001	25
D	30-10-2001	33
E	07-11-2001	41
F	21-11-2001	55
G	07-12-2001	71
H	09-12-2001	73

dates were carefully selected in order to sample as much of the different phases of the flare as possible without asking for an excessive amount of time on the VLBA. The epochs were selected such that the rapid rise of the flare at feature C was covered as closely as possible, followed by three more widely spaced observations on the downward phase of the flare. There is a period of about two weeks during which the main peak of the maser slowly increases in intensity. It was judged that one observation would be sufficient during this period. The maser then rapidly increases in intensity over the next two weeks and remains at its peak for less than a week before starting to decay. Four observations at weekly intervals were requested during this stage, The decay phase takes another two months, but just two more observations at two week intervals were used.

The VLBA follows a dynamic scheduling policy, so the observations were carried out whenever conditions were favourable during the requested intervals. Table 5.1 gives the dates of the observing runs. Observation G was not correlated since there were too many observational errors at different antennas. Figure 5.1 shows the timing of the observations relative to the flare cycles. The progress of the flare during this time was closely monitored at HartRAO in order to ensure that the VLBA observations were correctly timed[1].

The observations, at both left and right polarisation, were carried out using the full VLBA at 2cm. The continuum source J1733-1304 was used as a calibrator. The sequence of scans consisted of 5 minutes on the calibrator and 30 minutes on source. The total observing time, including the calibration observations, was 6 hours. Since the maser features span ~ 10 km.s^{-1}, a bandwidth of 1 MHz (covering 25 km.s^{-1}) was used. The observations were correlated at the VLBA correlator in Soccoro (USA) using 512 channels, giving a velocity resolution of 0.05 km.s^{-1}. This is sufficient to separate the maser features, since they are typically separated by ~ 1 km.s^{-1}. The central velocity (at channel 257) was 1.28 km.s^{-1} and a rest frequency of 12178.595 MHz was adopted.

[1]I would like to thank Mark Claussen at the NRAO for making sure that the observations were correctly scheduled and for preparing the *SCHED* file.

Figure 5.1: Timing of the VLBA observations relative to the flare cycle of feature C in G9.62+0.20E. The red lines indicate the times of the VLBA observations.

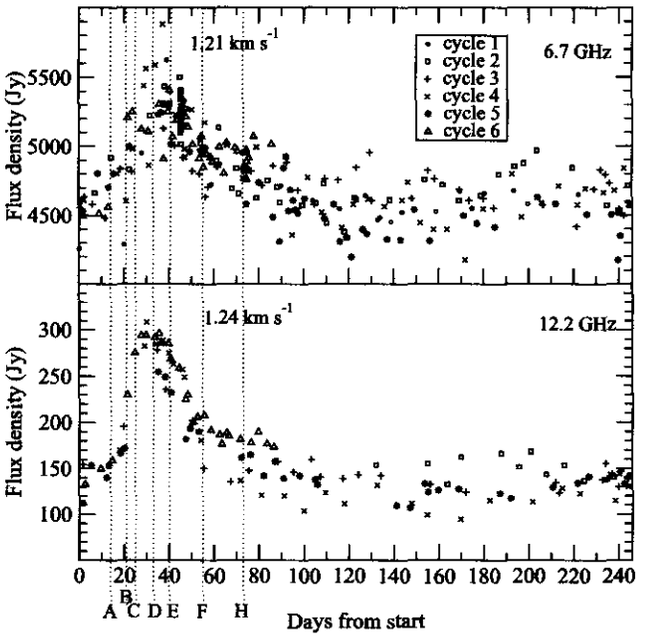

5.3 Reductions

The data were calibrated and reduced using the Astronomical Image Processing System (*AIPS*).

The VLBA correlator mislabels the polarisations in the *uv*-data catalogue. This is fixed using the task *FXPOL*. The VLBA correlator uses a two-bit (four level) quantisation. Gradual voltage drifts can cause errors in the digitisation which lead to errors in amplitude. Since the left- and right- circular polarisations are correlated separately, the digitisation errors can lead to an apparent polarisation in the source. Since methanol masers are only weakly polarised this error is easily noticed. The correlator digitisation errors were corrected using the task *ACCOR*.

The data were examined for bad scans and flagged using *SPFLG* and *IBLED*. *SPFLG* is particularly useful for finding frequency-dependent errors and radio frequency interference (RFI), while *IBLED* enables one to spot time-dependent errors. The data displayed should be smoothly varying in amplitude as a function of hour angle. All obvious discontinuities were blanked out. The observation and correlator logs were also examined for reported problems and particular attention was paid to those antennas.

The fringe rate for the continuum calibrator was found using *FRING* before using *BPASS* to find the time-dependent bandpass corrections for both the auto- and cross-correlated spectra. The velocity information for the source was entered into the catalogues using *SETJY*. The observed frequency of the observations gradually shifts due to the motion of the Earth. These changes in Doppler velocity were corrected using *CVEL*. This task also applies the bandpass calibrations to the data.

5.3.1 Amplitude calibration

There are two options for the amplitude calibration. One can use an external continuum calibrator observed at regular intervals. This has the disadvantage of requiring more observing time off the source of interest. The other option is to select a total power spectrum from a reliable antenna as a template spectrum, and use the gain calibration for that antenna. This method assumes that the amplitude of the maser stayed constant during the six hours of the observation. This assumption is valid in most cases, except at the peak of the flare, but none of the observations were made during this time.

The template spectrum must have no bad data in it and should preferably be taken at maximum elevation. The most important criteria is to make sure that there are no signs of RFI during the scan taken since this leads to errors in the recorded system temperature. The recorded system temperatures for the selected scan were examined carefully to make sure that a constant value was recorded. Once a suitable template spectrum was found, it was compared to all the scans at each antenna and a gain correction calculated relative to it. The task *ACFIT* was used to do this. The *ACFIT* solution was examined and note was taken of solutions with extremely high gain, indicating high attenuation of the signal, usually due to dense cloud, rain or the source being low on the horizon. Once the amplitude calibration was applied, the data with high gain corrections were flagged using *IBLED*.

5.3.2 Phase calibration

The time-dependent phase delay, or instrumental delay, was found by running *FRING* on the continuum calibrator. The delay solution was smoothed using *SNSMO* and then applied to the maser source using two-point interpolation.

The phase rate calibration was found using a compact maser feature as the source model in *FRING*. The channel used corresponded to a feature at 3.6 $km.s^{-1}$ and is visible in the cross-power spectra for the longest baselines, indi-

cating that it is a very compact source. The solutions were examined to make sure they did not have any abrupt changes which would indicate the solution interval was too long. A solution interval of 0.5 minutes was used, while the time interval in the calibration table (CL table) was 0.1 minutes. This self-calibration method destroys the absolute position information, hence all maps displayed in this chapter are relative to the reference feature. The nominal position of this feature is at 18:06:14.659 -20:31:31.57 (J2000).

5.3.3 Imaging

Pairs of antennas record a visibility function in the *uv*-plane. The *uv*-plane describes the distribution of baselines between antennas used. The baseline tracks for a typical observation of G9.62+0.20E are shown in Figure 5.2. The sky brightness function is the Fourier transform of the visibility function. Thus a two-dimensional Fourier transform of the visibility function will produce an image of the target object. However, the sky brightness cannot be retrieved directly because there are a finite number of baselines sampled, leading to incomplete coverage of the *uv* plane. The sky brightness function is usually estimated by using a model of the source to interpolate across gaps in the *uv* coverage. The basic assumption is that the source consists of a number of Gaussian components in an otherwise empty sky. The *CLEAN* algorithm models these components as a series of delta functions, convolved with a clean beam with the same dimensions as the main lobe of the dirty beam. Only a small amount of emission is subtracted at one time. The process is iterated until all the emission is subtracted from the original dirty image. Care has to be taken not to clean too deeply, otherwise emission due to noise will be added to the components modelling the source. The final *CLEAN* image is formed by convolving the accumulated point source model with an elliptical Gaussian fitted to the central lobe of the dirty beam, and adding the residuals to the image. The dirty beam is shown in Figure 5.3 and an example of a cleaned image is shown in Figure 5.4.

The quality of the image can be improved by doing self-calibration to remove the effects of rapidly-changing atmospheric conditions which have not been removed in the previous calibration steps. Since the science goal involves tracking changes in maser amplitude, it is important to retain the absolute amplitude calibration. No further amplitude calibrations were done, since self-calibration, while it improves the S/N, destroys the absolute amplitude calibration. Phase self-calibration destroys the absolute position information, so subsequent image coordinates are relative to the position of the reference feature (known as the phase center). The self-calibration on the phase was done by using a compact maser spot as a reference channel. A preliminary image using 100 *CLEAN* components from *IMAGR* was used as the source model,

Figure 5.2: *uv* coverage for observation A.

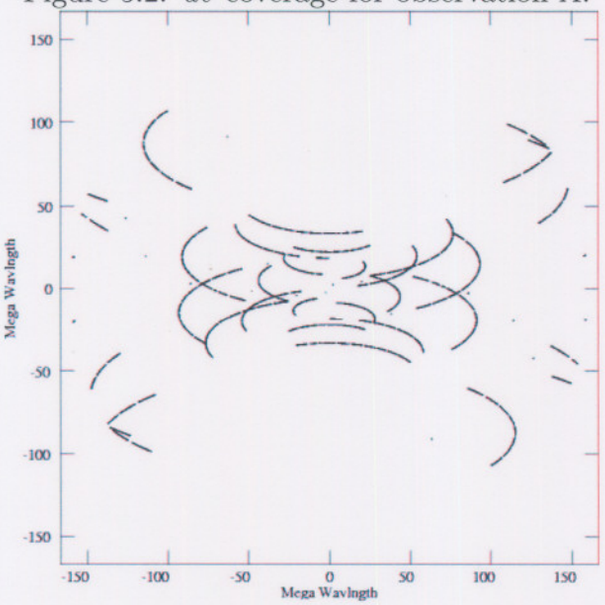

Figure 5.3: Dirty beam for observation epoch A.

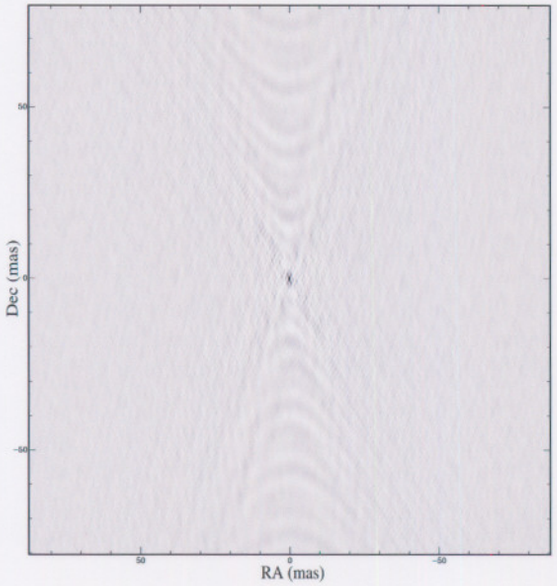

Figure 5.4: Cleaned image of channel at 3.6 km.s^{-1} . The restoring beam is shown to the right.

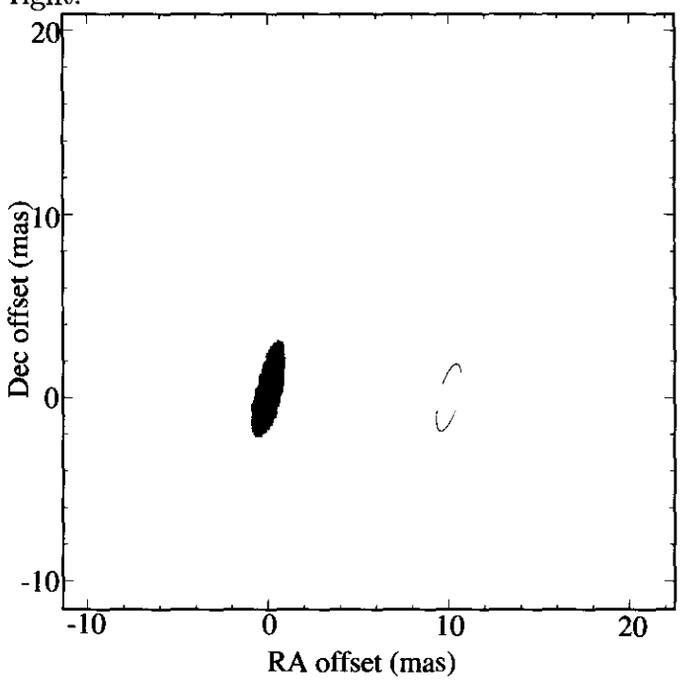

which was then input back into *CALIB*. The subsequent solution was applied to the reference channel and a new image and source model was generated by *IMAGR*. The procedure was iterated until the solution converged. The images were checked at each stage to ensure there was indeed an improvement in the image quality. The rms noise of the images were checked using *IMSTAT*. The solutions typically converged after five iterations. The derived corrections were then applied to all the other channels. The final data cube was produced using *IMAGR* with a cell size of 0.2 mas. The data were *CLEAN*ed until the residual flux limit was 60 mJy (about 4 times the theoretical rms noise).

Care has to be taken in the identification of maser components on the final image since errors in the calibration or imaging process may lead to artifacts. Phase errors can cause multiple identical features scattered around the correct position. The phase calibration was repeated and data with bad solutions were flagged out until no such artifacts were seen in the images. Imperfect subtraction of the dirty beam's sidelobes can create features resembling the sidelobes. The sidelobe features have an amplitude of the order of 0.5% of the peak flux density of the maser spot, so they are not dominant in the image.

Table 5.2: Velocity ranges of 12.2 GHz maser components in G9.62+0.20E

Label	Start velocity $km.s^{-1}$	End Velocity $km.s^{-1}$
E3	4.068	4.357
E4	4.068	4.357
E1	3.444	4.021
E2	2.722	3.396
E5	2.722	3.396
D	2.049	2.674
A	1.713	2.001
B	1.328	1.664
C1	0.991	1.424
C2	0.991	1.424
F1	-0.499	0.222
I	-0.499	-0.162
G1	-1.316	-0.547
G2	-1.028	-0.547
H	-2.181	-1.364
F2	-2.999	-2.230

5.4 Results

5.4.1 Structure of the maser components

The data cubes were examined using the *KARMA* data visualisation tools *KRENZO*, *KVIS* and *XRAY*. Of the 512 velocity channels, only the central 158 channels contain the maser emission. The rest of the channels can be disregarded in the analysis. Sixteen individual maser components, with distinct spatial positions and velocity ranges, were identified. Zero-moment maps, in which the data cube is integrated along the velocity axis for specific velocity ranges, were made using *KRENZO*. The images of Minier et al. (2002b) show the same overall structure as seen here, but the longer integration times used here (six hours compared to about one hour) give a better *uv*-coverage, with the result that feature E is resolved into five separate, compact components. Table 5.2 gives the selected velocity ranges for the components and Figure 5.5 shows their spatial distribution. The nomenclature of Minier et al. (2002b) is adopted and expanded on where necessary.

The maser components A, B and C are connected by weaker emission. Minier et al. (2002b) speculated that component D may be linked to components A, B and C by diffuse emission, but no evidence of such emission is seen here. The region E has a complex structure, with five distinct compact maser components. A channel from the component E2 was used as the reference channel for the phase calibration because of its compactness. G1 has a linear structure with a strong velocity gradient. H consists of two smaller components

Figure 5.5: Distribution of maser features in G9.62+0.20E. The figure was taken from the fourth VLBA observation, when features A, B, C and D were at their maximum intensity. The features are colour-coded according to velocity. The contour levels are at 0.2 Jy/beam in each velocity channel. The inset shows the 12.2 GHz total power spectrum. The colour-bars superimposed on the spectrum indicate the corresponding colour range in the contour map and the features are labelled on the contour map and on the spectrum. Some spurious features due to the sidelobes of the beam can be seen at the same velocity as features C1 and C2. The restoring beam is shown to the bottom left.

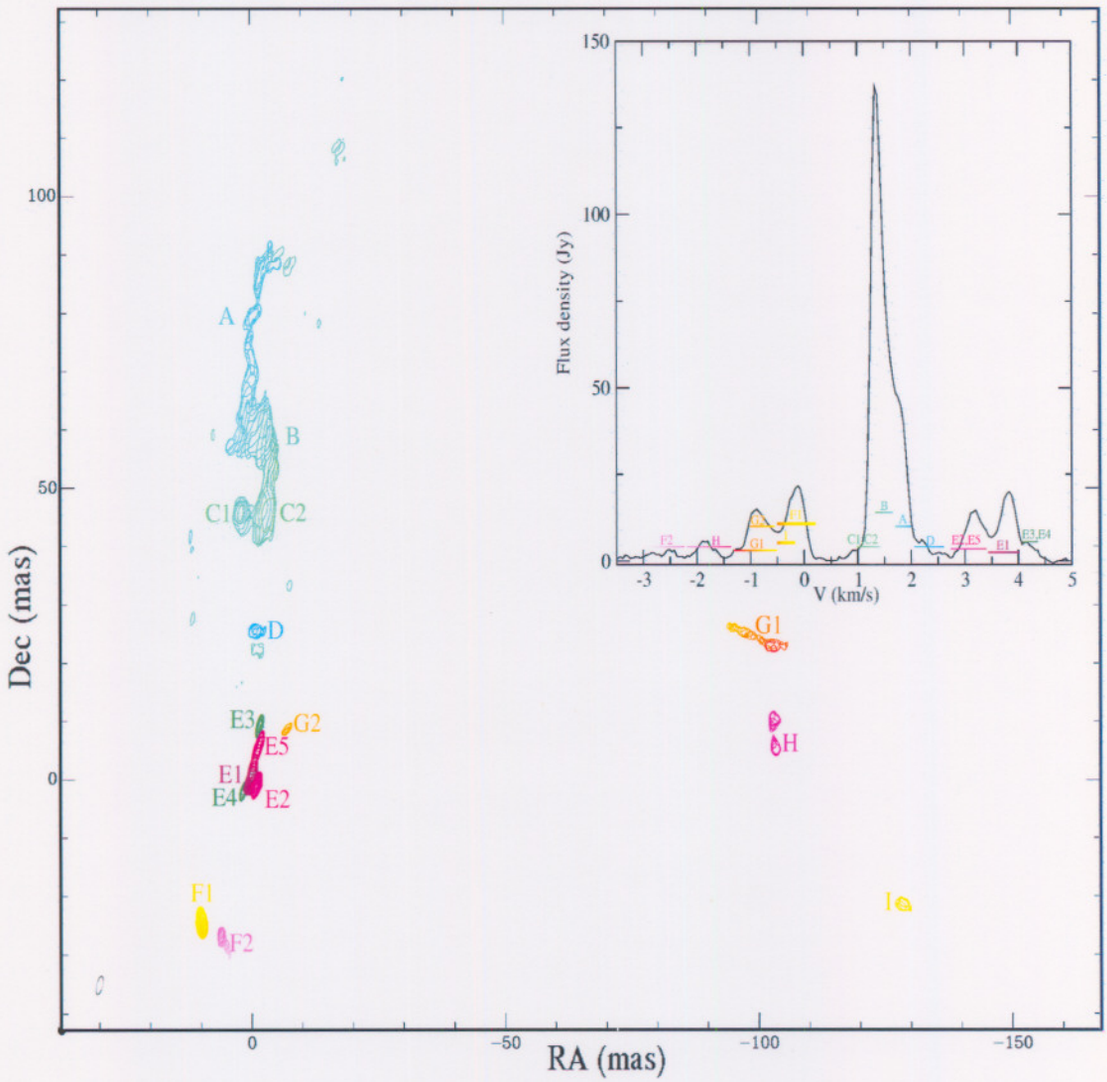

connected by slightly weaker emission, but it has been treated as one structure in the following analysis since there is not an obvious division point between the two components. D and I are weak but compact spots.

The maser components appear to have velocity gradients. This can be seen most clearly in the transition from features A through C, and in F1 and G1 (Figure 5.6). The velocity gradient in the group of components A through C is ~ 0.004 km.s^{-1}.mas^{-1}, while it is 0.20 and 0.22 km.s^{-1}.mas^{-1} in components F1 and G1, respectively. Assuming that the distance to G9.62+0.20 is 5.7 kpc (Hofner & Churchwell, 1996), the velocity gradient for F1 and G1 is ~ 0.03 km.s^{-1}.AU^{-1}.

Different baselines act as filters for different scales of structures. It is possible that some flux could be resolved out for the features with large scale structures since there is no information from extremely short baselines. The amount of flux that is resolved out in the cross-power spectra has to be checked as this could affect the interpretation of the variability in the images. The top panel in Figure 5.7 shows a total power spectrum, which is equivalent to a single-dish spectrum, at the Los Alamos antenna. The second panel shows a cross-power spectrum between Los Alamos and Pie Town, the shortest baseline in the VLBA. It can be seen that flux densities for each maser feature are similar to that of the total power spectrum, thus little or no flux has been resolved out. The third panel shows a cross-power spectrum between Brewster and Mauna Kea, in which the dominant maser feature at 1.2 km.s^{-1} is mostly resolved out, while the more compact features at 3 and 4 km.s^{-1} (features E1-E5) are still clearly visible. The fourth panel shows the longest baseline, between St. Croix and Mauna Kea, where only the most compact features are visible in the spectrum. It can be seen that features A, C, D, and G have compact components.

Another way of examining the structure is with visibility amplitude vs. *uv*-distance plots, which show the amount of emission seen at the different scales. Figure 5.8 shows the visibility amplitudes vs. *uv*-distance of the channels corresponding to each spectral feature. The top-left panel shows an emission-free channel as an estimate of the noise. The noise will be reduced as the square-root of the number of channels averaged for each feature. The longer *uv*-distances show the smaller scale structures. Thus greater emission at smaller *uv*-distance and a rapid drop to zero in amplitude towards greater *uv*-distance, indicates a source that has predominantly large scale structure and is "resolved out" on the longest baselines. It can be seen that the emission from features A, B, C and E1 comes predominantly from large scale structures but they do have compact cores visible at the longest baselines. The emission does not drop to the noise level for features A, B and C, implying that they may have compact cores which are not fully resolved. The emission at longer baselines drops to the noise level for features D, G1, G2, H and F2, hence they are fully

Figure 5.6: Close-up images of the velocity structure of various maser components. The complex of components A, B and C is shown in the left-hand panel. Component F1 is shown to the upper right and G1 to the bottom left.

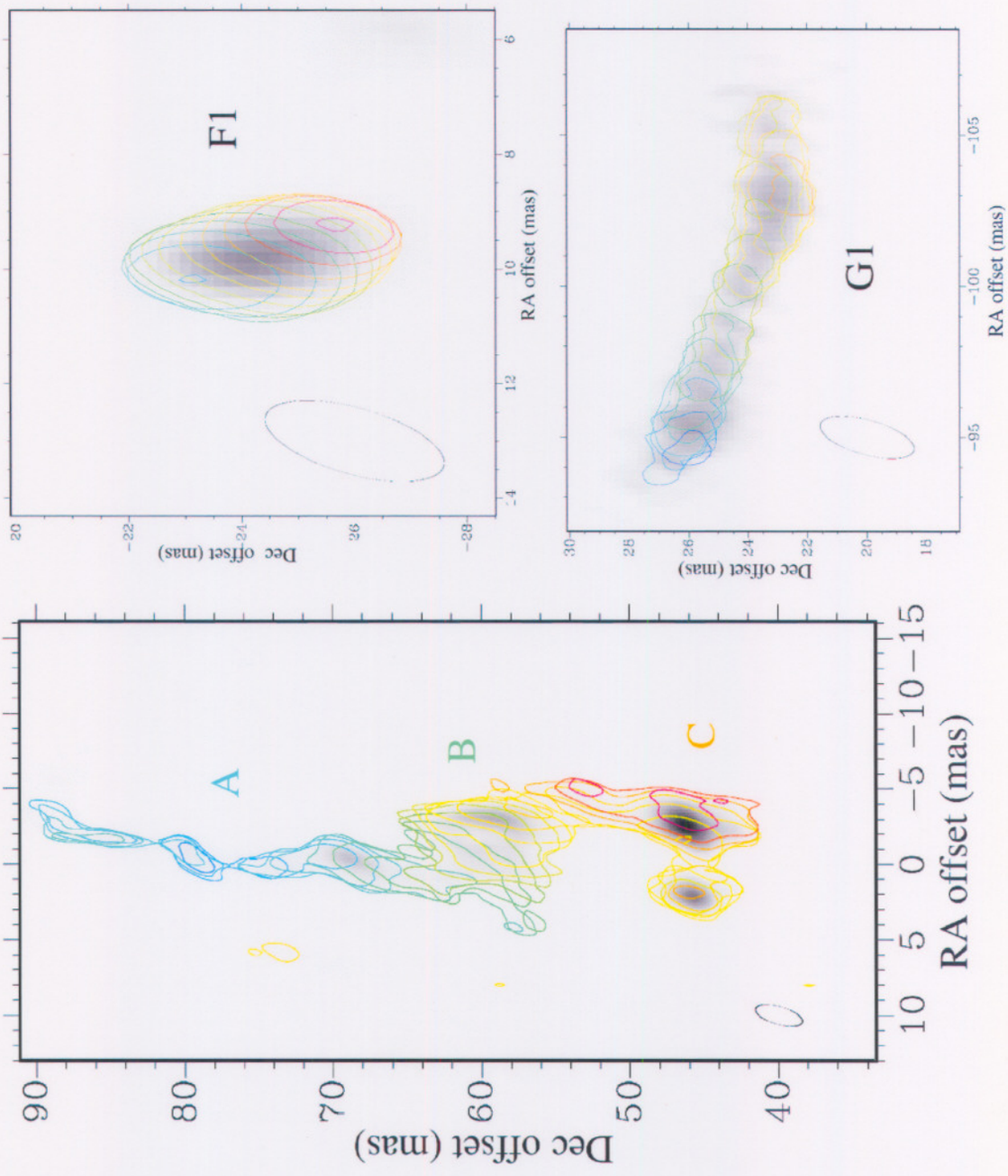

Figure 5.7: Examples of total power (top panel) and cross-power spectra

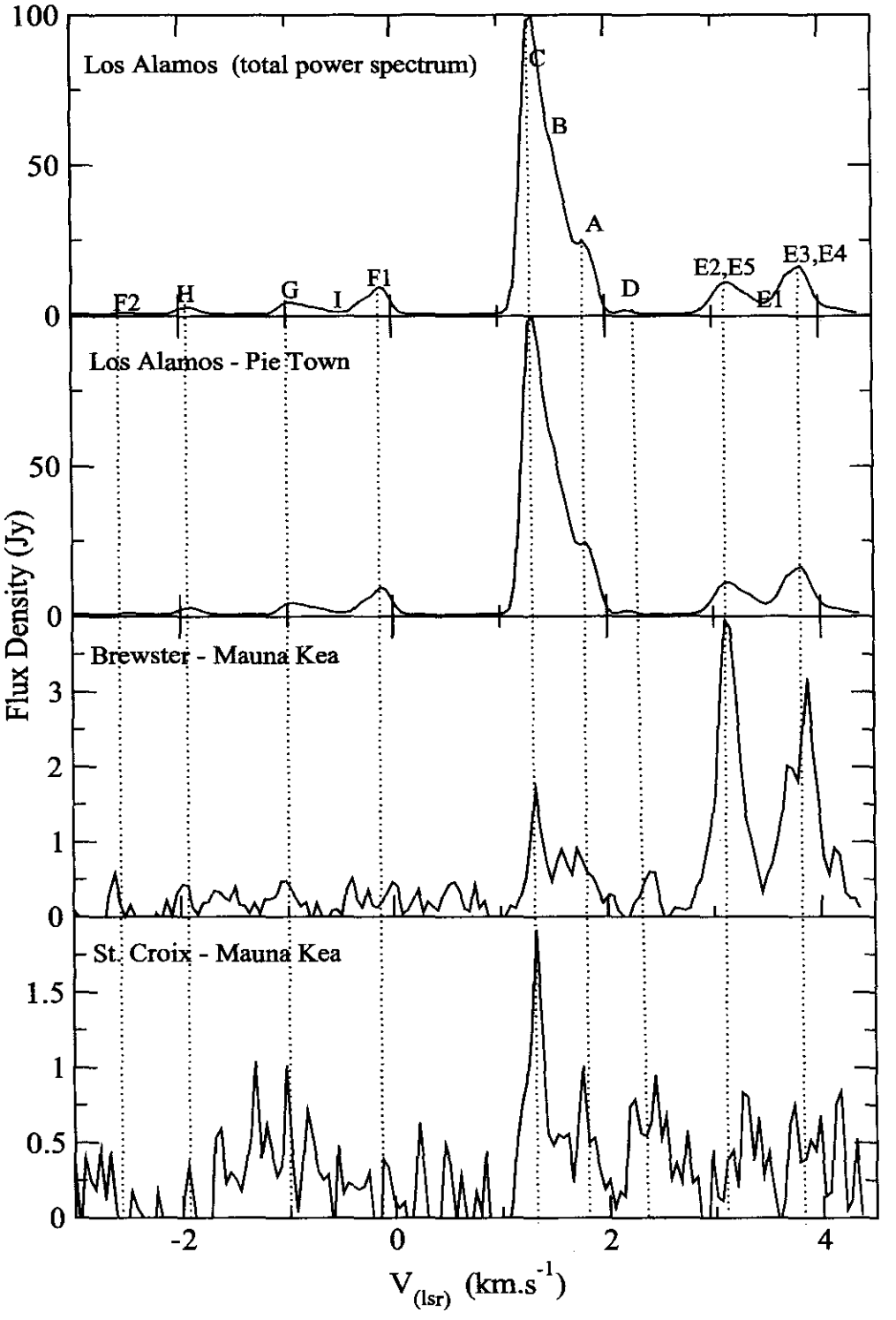

Figure 5.8: Visibility vs. *uv*-distance for the maser features. The visibility amplitudes have been averaged and binned.

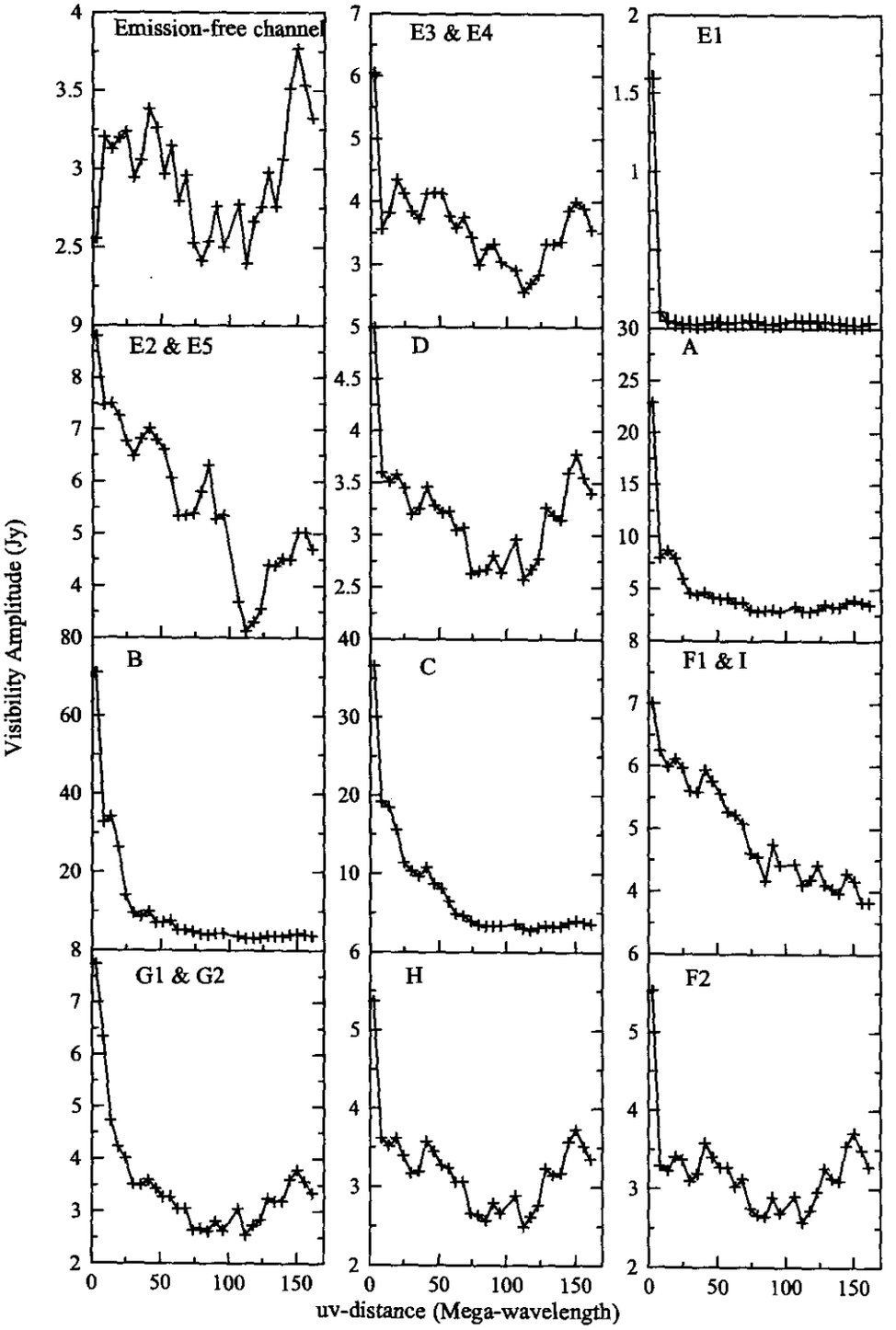

resolved at the longest baselines. The other features have the same velocities so it is not possible to extract the information about their structure from the amplitude vs. *uv*-distance plots.

5.4.2 Variations during the flare

The antennas at Pie Town, Hancock and Fort Davis were either unavailable, or data from them was not usable because of bad weather during some of the observations. As a result of this, the beam sizes for the different epochs are not consistent if all available antennas for a particular observation are used. This affects the observed flux density and apparent structure of the masers. Therefore these antennas were flagged out of all the data sets before running IMAGR to produce the data sets for the following analysis. The resulting beam parameters are listed in Table 5.3. There are still some small variations in beam size and orientation because of temporary problems with some antennas but these should have only a minor effect on the following calculations.

Imaging of individual channels results in a "data cube" with an image of each channel. Zero-moment maps are created by averaging across all the velocity channels in order to produce a single image. The zero-moment maps, for each epoch, derived from the full velocity range in which emission is present are shown in Figure 5.9. There appear to be no changes in the morphology of the maser components during the flare. The features also do not move with respect to the phase centre from one epoch to the next. In addition, no new maser spots are formed during the flare. The maser components simply get brighter and then start to fade to their pre-flare intensity. Comparison of the visibility amplitudes vs *uv*-distance for each epoch show that the amplitude of the variation is independent of the scale of the structures seen. Thus, even if some of the emission on larger scales is resolved out by the VLBA, the time-

Table 5.3: Beam parameters for the different epochs with Pie Town, Hancock and Fort Davis flagged out for all epochs.

Epoch	Maj. Axis (mas)	Min. Axis (mas)	Pos Angle (°)
A	1.7	0.59	-16.27
B	1.8	0.62	-21.04
C	1.7	0.56	-6.86
D	1.7	0.56	-14.64
E	1.7	0.60	-14.45
F	1.7	0.69	-20.79
H	1.7	0.72	-21.9

series described in the following discussion are probably a fair representation of the changes occurring in the maser regions.

Time-series were found for each maser feature using the task *BLSUM* in the following manner. Zero-moment maps were constructed for each of the velocity ranges given in Table 5.2. The noise levels for each map were estimated using *IMSTAT* on an emission-free region of the image (the top right-hand corner does not have emission at any velocity). The noise pixels were then set to an *INDEF* value using *BLANK*. *BLSUM* requires a template blotch map which is used to manually select the area over which to sum. The blotch templates were constructed by averaging the noise-blanked maps for all the epochs using *SUMIM*. The input data cube for *BLSUM* consisted of the zero-moment maps for each epoch, so that the third axis of the cube was in fact a time axis. *BLSUM* cannot automatically correct for the beam size in such a situation, so the flux density is given as an average brightness in Jy/beam. An absolute flux density, which is independent of the beam size, can be calculated by finding the beam size in pixels/beam for each epoch, converting the average brightness to units of Jy/pixel and then multiplying by the total number of pixels in the blotch image.

The results of the calculations are shown in Figure 5.10. There appear to be three different trends in the time-series, depending on the positions of the masers. The masers have been grouped into three different regions based on this behaviour. The progress of the flare is best sampled amongst the features A, B, C and D. The flare appears to peak earlier at the other two groups. The exact times of the peak of the flares at the different maser components cannot be determined because of the poor time resolution, but there may be a 1–2 week delay in the propagation of the flare through the different regions.

The flare reached its maximum between epochs A and C in region 1, while the maximum could be anywhere between epochs B and D in region 2. There is a gap in the observations at HartRAO due to bad weather, but from comparison with other cycles it is likely that the flare in region 3 peaked a few days before epoch D. Unfortunately the S/N of the 12.2 GHz HartRAO observations of the weaker spectral features is inadequate to permit an analysis of their time-series.

The velocity feature at 1.21 km.s^{-1} flares simultaneously at both frequencies but the -0.14 km.s^{-1} feature at 12.2 GHz appears to flare approximately 30 days before the same feature at 6.7 GHz (Figure 5.11). The disparity in the apparent times of the flares can be explained if the 6.7 GHz maser spot is not in the same spatial region as the 12.2 GHz maser. This issue cannot be explored any further until high-resolution spot maps at 6.7 GHz are obtained and observations with better time resolution are obtained for the 12.2 GHz flares.

Figure 5.9: Zero-moment images for each epoch. The restoring beam is shown to the bottom right in each panel. The three regions into which the map is divided in the discussion of the variations in flux density are shown in the first panel.

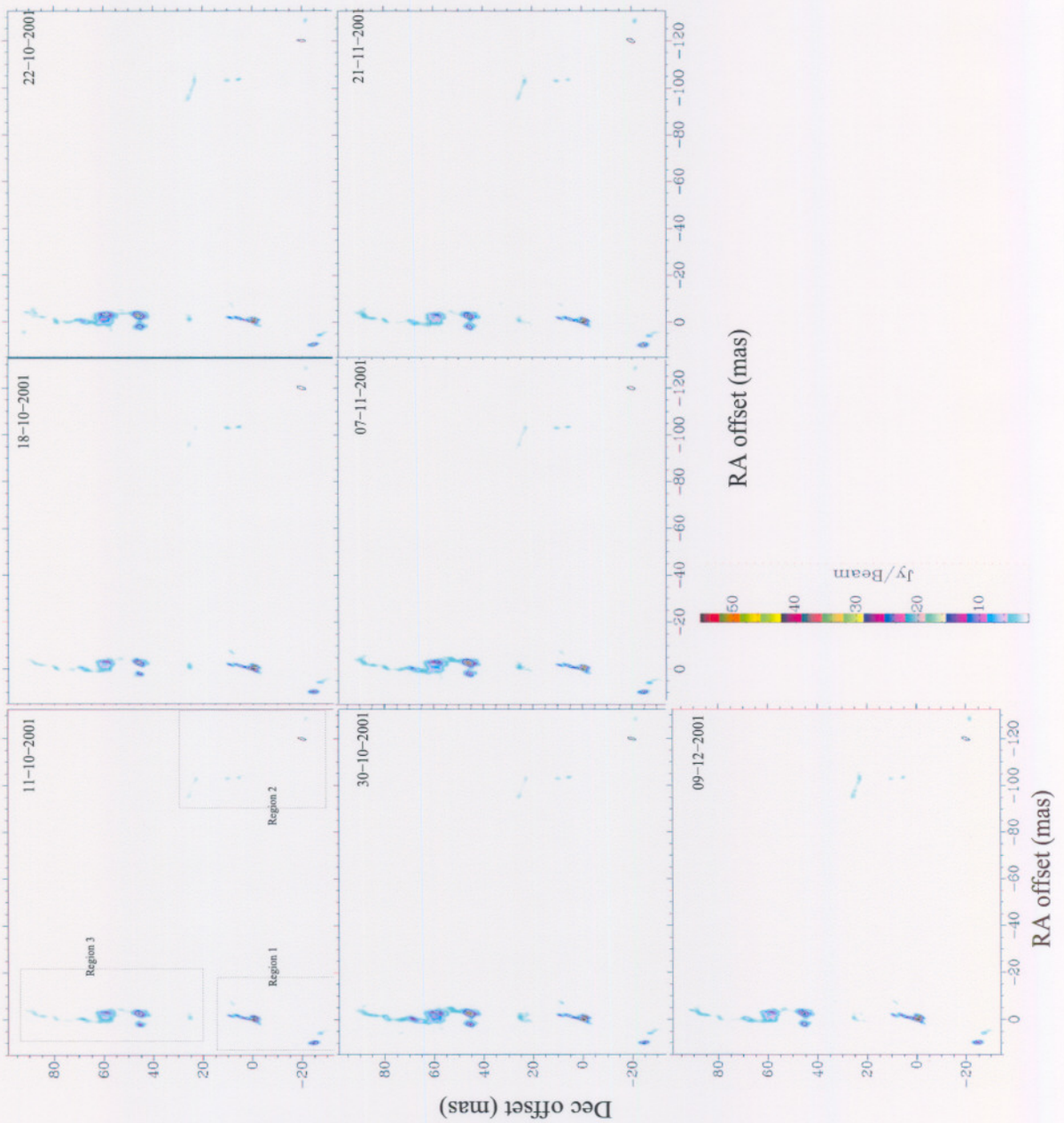

Figure 5.10: VLBA time-series for maser features in G9.62+0.20E. The three panels are divided according to the spatial distribution of the masers. The single-dish observations at HartRAO are also shown for Features C and B.

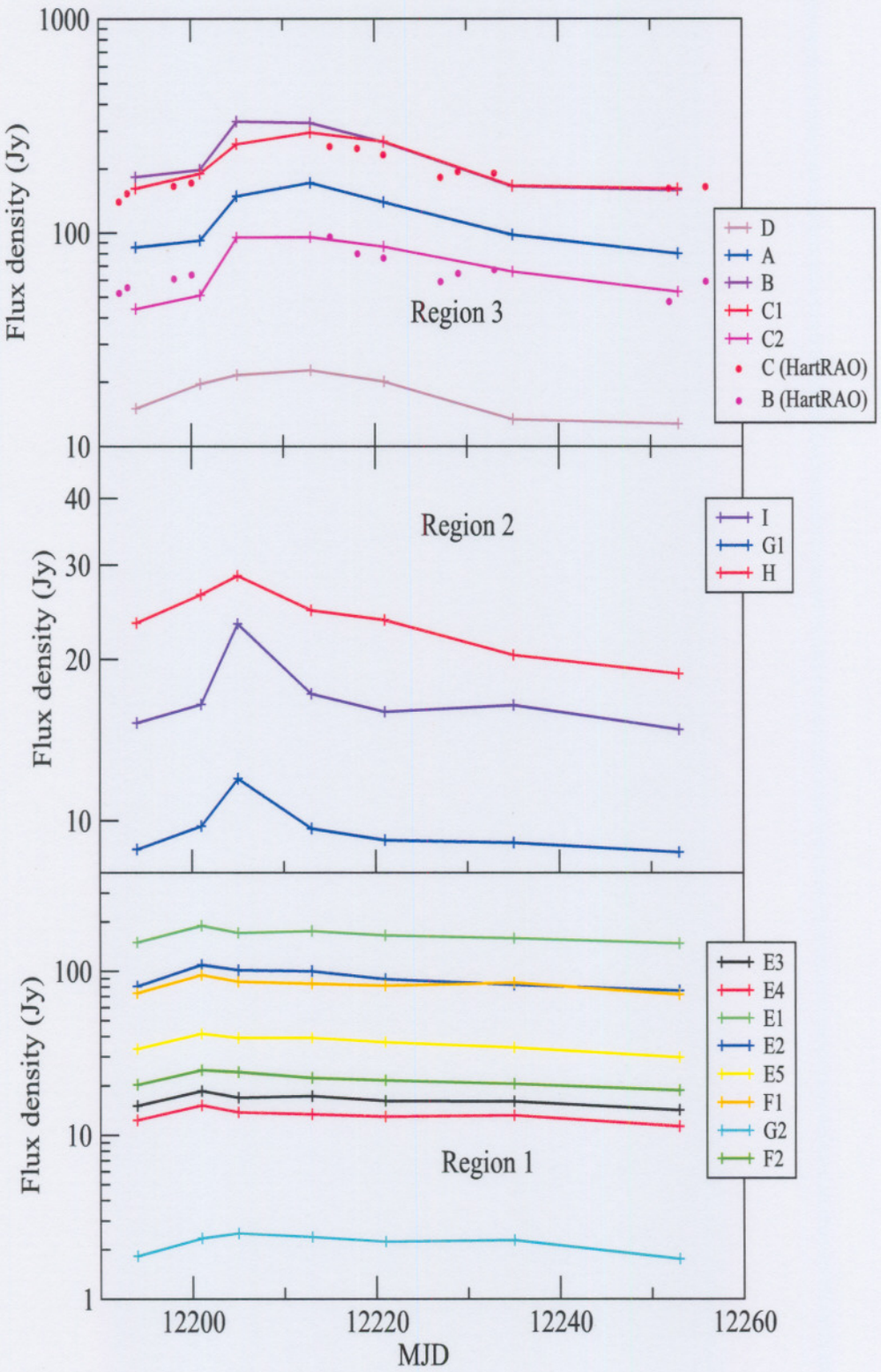

Figure 5.11: Comparison of flux density at 12.2 and 6.7 GHz for the 1.21 km.s^{-1} feature (left panel) and the -0.14 km.s^{-1} feature (right panel).

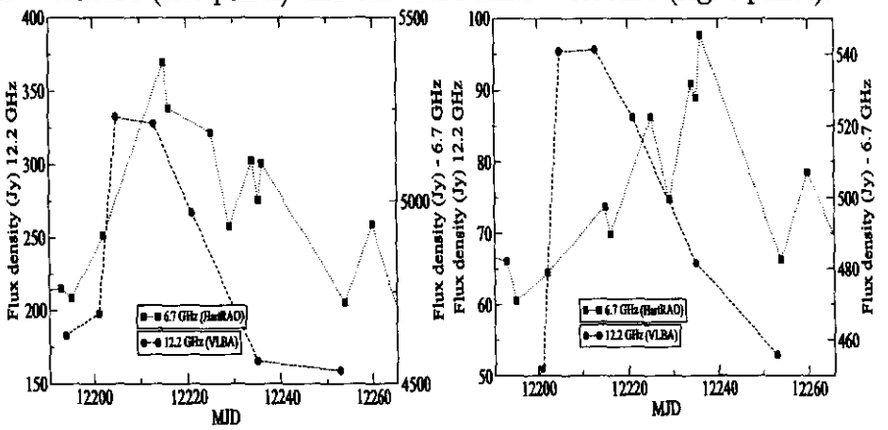

5.5 Discussion

The lack of change in the structure of the masers themselves, and the fact that the masers return to almost the same pre-flare level after each flare, strongly suggests that the cause of the flare is external to the masing region. This rules out the possibility of a disturbance such as a shockwave or clump of matter actually passing through the masing region, since this would radically change the structure of the maser components. The only possibilities left are an increase in the seed photons or, assuming that the masers are radiatively pumped, an increase in the pumping radiation.

If variations in the seed photons are causing the variability, the cause of the modulation would most likely be intrinsic to the star since the cloud is optically thin to radiation at 6.7 and 12.2 GHz. However, there is no known stellar pulsation mechanism that could cause variations on the time-scales observed, or with the irregular profiles seen. A possible means of causing periodic outbursts in the star may be periodic mass dumps from the accretion disc, similar to those seen in cataclysmic variables. This would still require a mechanism to modulate the accretion flow rate in a periodic manner.

A close binary system seems to be the most likely of the flare mechanisms as discussed in the previous chapter, because of the definite periodicity of the flares. As the flare lasts for 3 months, the modulation cannot simply be due to the effects of a binary system since the angular size of the stars would be too small to give rise to an effect that lasts for a third of the orbital period. It is more likely that the effect is due to the motion of a large dust structure. Binary systems in the earliest stages of stellar evolution have not been studied

at all for the case of high mass stars, but the same sort of dynamics found in low mass systems would probably apply. The environment of a young binary system can be highly complex, with interacting circumstellar discs around each star, as well as a circumbinary disc around the entire system (Lubow & Artymowicz, 2000, and references therein). In addition to this is the surrounding molecular cloud, with possible accretion flows onto the discs. The interaction of all of these elements may cause strong modulations of the infrared radiation reaching the maser regions. The exact mechanics of this process cannot be formulated without further knowledge of the composition of the system, but it seems likely that maser flares, small decreases in maser intensity (as in the case of G188.95+0.89) as well as sinusoidal variations (eg G196.45-1.68) can be explained by the same basic scenario. The effects of the propagation of radiation in a region with such complex morphology cannot be easily predicted. The optical depth of the dust is wavelength dependent and different optical depths will shift the radiation to different wavelengths. It is not clear whether an enhancement of the radiation from the central star(s) would lead to a maser flare, or if an eclipse would shift the wavelength of the radiation reaching the maser regions to the appropriate wavelength for maser pumping. This problem can only be solved by modelling the radiative transfer in different scenarios.

The delay in the peak of the flares may possibly be explained from an analysis of light travel times. The projected sizes of the different regions are as follows: The longest extent of region 1 is $\sim$ 44 mas, which at an assumed distance of 5.7 kpc gives 247 AU. The light travel time across this distance is 1.3 days. The longest extent of region 2 is $\sim$ 63 mas or 357 AU, which gives a light travel time of 1.9 days. The longest extent of region 3 is $\sim$ 67 mas or 384 AU, which gives a light travel time of 2.3 days. Since the interval between observations with the VLBA is of the order of a week, delays of about a day would not be detected. The single-dish observations at HartRAO were usually separated by about a day at the peak of the flare at features A, B and C, but no time delays were noticed.

The distances between the regions are as follows: The separations between regions 1 and 2 is approximately 665 AU or 3.6 days, between 1 and 3 approximately 437 AU or 2.4 days, and between 2 and 3 760 AU or 4.2 days. The observed time delays are of the order of a week or more. The discrepancy could be explained if the maser groups are not at the same distance along the line of sight. Another possibility is if the modulating radiation is strongly beamed and moves across the sky in such a way as to pass across each region in succession. However, it is not obvious how such an effect or the observed pattern, would be created.

5.6 Conclusion

The series of images taken over the course of three months show no change to the structure or relative positions of the maser components. The mechanism causing the flare is therefore spatially separate from the masers. The flares are probably caused by modulation of the pumping infrared radiation and the regularity of the flares is best explained by a binary system. The evidence of a delay in the propagation of the flare in different maser components is worth further investigation since this may help locate the origin of the cause of the flares, or be a means of estimating the relative offset of the maser groups along the line of sight.

Chapter 6

Summary and outlook

A multi-wavelength approach has been used to study class II methanol maser sources. Twelve maser sources were imaged in the near-infrared at I, J, H and K bands. A total of 54 masers were monitored from January 1999 to April 2003 at 6.7 GHz and several were found to have periodic variations. The analysis of the overall variability only covers the period up to September 2002, while the all available data was analysed when investigating the possible periodic sources. The periodic source G9.62+0.20E was imaged in 2001, during the course of a flare, using the VLBA at 12.2 GHz.

These observations have given us new information about the methanol maser sources but are not sufficient to develop a definitive model of the conditions producing them. In fact, more questions have been raised than have been answered. In this chapter, I summarise my results and conclusions and suggest strategies to follow up on some of the questions raised.

6.1 Variability of 6.7 GHz methanol masers

The maser monitoring programme found that most of the masers were variable to some extent. Some were found to drop below the detection limit for a while; this should be kept in mind when considering the completeness of methanol maser surveys. However, since the variability of the masers is not predictable in most cases, it is not possible to determine the percentage of masers which may have been below the detection limit during surveys.

The velocities of spectral features were not found to change over the four-year monitoring period. This is in contrast to the results obtained for water masers, which are frequently associated with high-velocity outflows.

The most significant result was the discovery that a number of sources (14% of the total sample) undergo periodic or quasi-periodic variations. G9.62+0.20E was found to have simultaneous flares at both 6.7 and 12.2 GHz. A series of seven imaging observations at 12.2 GHz was done using the VLBA. It was found that the maser spots did not change in position or shape and no new ones appeared. Instead, the masers simply increased in intensity and then decreased, implying an increase in the background flux of the pump or seed photons. There is evidence of a delay in the progression of the flare across the entire region, but the time resolution of the observations is not sufficient to reach any conclusions on the meaning of such a delay.

The periods range from 132 to 668 days. Such long periods cannot be explained by either stellar pulsations or rotation since these have periods of the order of hours to a day for high mass stars (Lang, 1992). The most plausible mechanism for causing periodic flares with the periods observed is the presence of a close binary system. The coalescence theory is strongly in favour of binary or higher order systems. However, clumps in an accretion disc or precessing or helical outflows may also give rise to periodic modulations of the infrared pumping flux. The current data does not make it possible to distinguish between these scenarios.

Short-term, random, uncorrelated variations are probably due to turbulence. Correlated variations may be due to changes in stellar luminosity as the protostar evolves. Low amplitude correlated variations with a time-scale of days to weeks may be due to interstellar scintillation.

6.2 The environment of methanol masers

A subset of the masers being monitored at 6.7 GHz were examined in greater detail by doing infrared imaging at I, J, H and K bands and considering the position of the methanol masers relative to that of MSX and IRAS point sources, H II regions, hydroxyl masers and water masers. Of the 12 fields imaged in the infrared, containing a total of 14 maser sites, 7 NIR sources with the characteristics of deeply embedded stars were found within 8 kAU of a maser site. The areas around the masers were crowded, indicating the presence of a cluster, but the sources closest to the methanol masers were typically the reddest in the field. They are not point sources, implying that there is either more than one unresolved source, or that the object imaged has a non-spherical morphology.

The number of IRAS point sources found to be close to the maser sites was relatively low compared to MSX sources. Thus the MSX catalogue is a better

tool for searching for infrared counterparts to methanol masers. However, the MSX satellite has insufficient resolution to locate the source powering the masers.

No definite pattern was found in the association of the methanol masers with H II regions and water or hydroxyl masers. However, there are always hydroxyl masers present in the cases where an UC H II region is present, but the converse is not true. This is consistent with the hypothesis that the methanol masers start at an earlier evolutionary stage than the hydroxyl maser, which are in turn excited before a detectable UC H II region is formed.

6.3 Suggestions for future work

The results of this thesis are not conclusive but there are a number of avenues of investigation that could be followed:

- The methanol maser monitoring at HartRAO should be continued, at least for those sources which have displayed significant variability. Of particular importance are the periodic sources. Longer time-series are needed to confirm the periodicity of the long-period sources. It is also possible that the periods of the flares could change over time if the orbital systems are not stable or are evolving.
- Other aspects of the methanol maser variability also need further investigation. There are sources which are monotonically increasing or decreasing in intensity. This behaviour may indicate changes in path length related to the dynamics of the region eg infall of matter. Likewise, the short-term flickering of some maser features could yield information about turbulence in the cloud.
- The possible time-delay between flares in features in G9.62+0.20E is intriguing and should be followed up on, either by doing more closely spaced observations with the VLBA, or by attempting to improve the S/N of observations done at HartRAO so that the weaker features can be monitored. Single-dish observations of this maser may be limited by the fact that some of the features have the same velocities, even though they are spatially separate. High resolution maps at 6.7 GHz will also be of help, since a longer and better quality time-series is available, but we cannot be sure that the 6.7- and 12.2-GHz maser features are exactly spatially coincident.
- High-resolution maps, covering as much of the range of emission scales as possible, are needed for the southern maser sources in order to un-

derstand the maser variability in cases where the maser structure is very complex.

- A causal relation between a methanol maser and a NIR source cannot be established on the basis of proximity alone, but monitoring the NIR along with the maser emission may be a way to determine if any of the visible NIR sources are linked to the masers. However, since a significant number of methanol maser sources cannot be associated with a NIR source, such an approach may not be very successful.

- Currently, mid-infrared imaging appears to offer the best possibility of locating the stars or compact cores powering the methanol masers. There is a much lower probability of confusion, since the more evolved stars in the cluster are not seen towards longer wavelengths. High-resolution detectors on telescopes such as Keck and VLT are also now becoming available. The link between the pumping of the masers and the flares can be investigated by simultaneously monitoring the mid-infrared and the maser emission.

- Close binary systems in high mass star-forming regions would have such small angular sizes that they cannot be imaged directly. However, evidence for these systems may be found by mapping the structure of the molecular core. There may be evidence of accretion structures or multiple outflows. Currently it is very difficult to distinguish between multiple outflow systems and uncollimated outflows. Future instruments such as ALMA have great potential for probing and mapping deeply embedded cores.

In conclusion, the variability of 6.7 GHz methanol masers promises to be a powerful tool for probing conditions in the earliest phases of massive star formation. However, at this stage in our understanding, any monitoring programme needs to be supplemented by supporting high-resolution, multi-wavelength observations in order to understand the processes triggering the changes in the masers.

Appendix A

Zero magnitude fluxes for the LCO system

The flux density in Jy at a particular wavelength is given by

$$F_\lambda = F_\lambda^0 10^{-\frac{m_\lambda}{2.5}} \tag{A.1}$$

where F_λ^0 is the flux density at λ of a zero magnitude star and m_λ is the magnitude at λ. Cohen et al. (1992) give the zero magnitude flux calibration for the stars Vega and Sirius. However, these fluxes were measured using the UKIRT photometric system. Our source magnitudes are calibrated to the LCO Persson et al. (1998) photometric system. A direct conversion between the two systems is not available in the literature. However, Carpenter (2001) gives transformation equations for a number of photometric systems (including UKIRT and LCO) to the 2MASS photometric system. It is therefore possible to derive the transformation equations to convert from the UKIRT system to the LCO system. The transformation equations are given below.

$$K_{LCO} = K_{UKIRT} + 0.005(J-K)_{UKIRT} + 0.008 \tag{A.2}$$

$$H_{LCO} = 1.054(H-K)_{UKIRT} + K_{LCO} + 0.015 \tag{A.3}$$

$$J_{LCO} = 1.055(J-K)_{UKIRT} + K_{LCO} - 0.005 \tag{A.4}$$

We can then obtain the flux densities for Vega on the LCO system. Table A.1 gives the converted values.

Table A.1: Fluxes for Vega on the LCO system

Filter	λ	m_λ	νF_ν	F_λ
	μm	Mag	Wm^{-2}	Jy
J	1.25	20.90	4.365e-09	1.819e3
H	1.65	21.77	1.959e-09	1.077e3
K	2.2	22.61	9.036e-10	6.626e2

Appendix B

Intensity contour plots for periodic maser candidates

Figures 1 to 10 show intensity contour plots for the sources discussed in Chapter 4. The velocity is plotted along the x-axis, while time is along the y-axis. The colour-scales and contour lines depict the intensity in Jy, with the range from low intensity to high intensity scaling from blue, through yellow, to red.

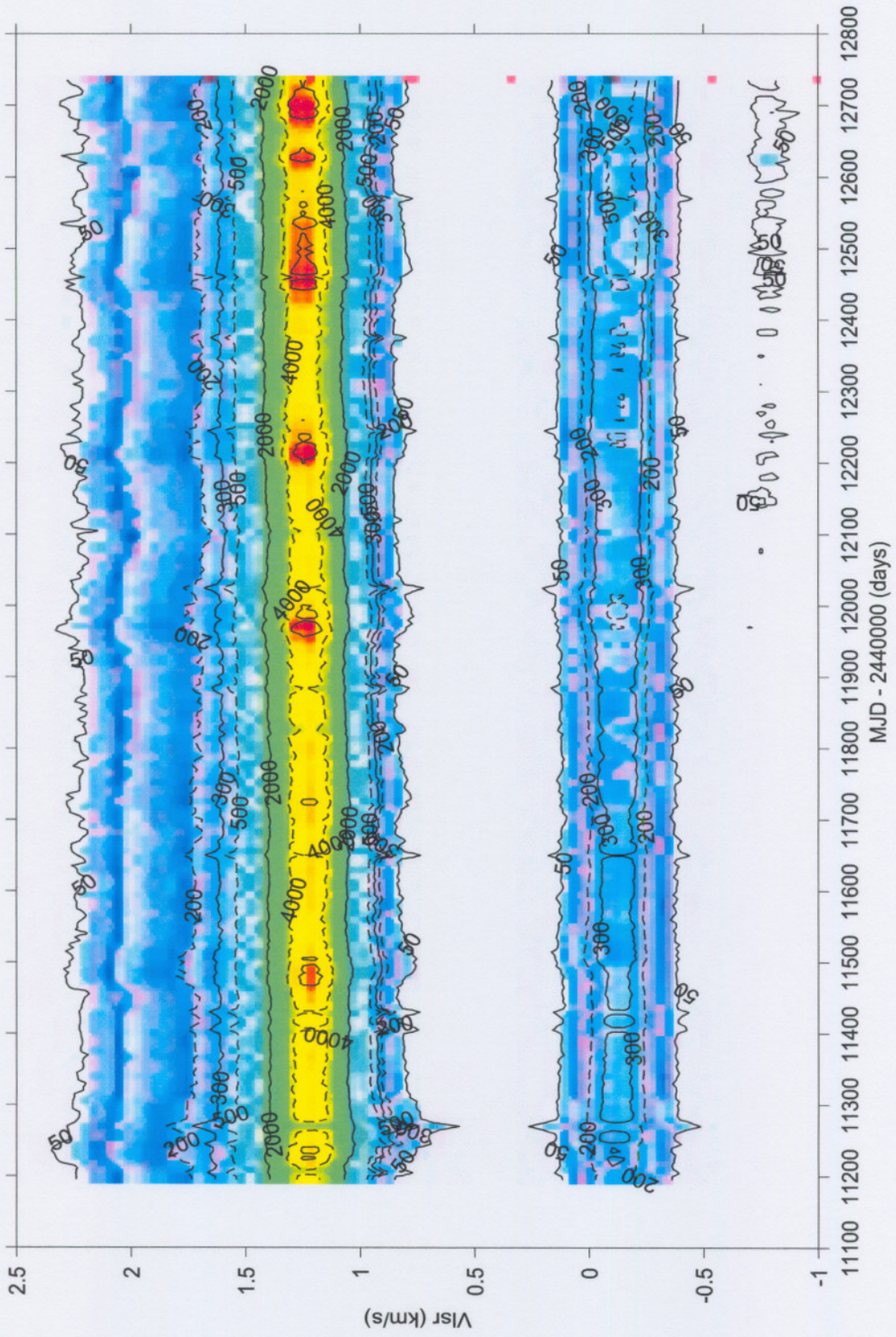

Figure 1: Intensity contour plot for G9.62+0.20

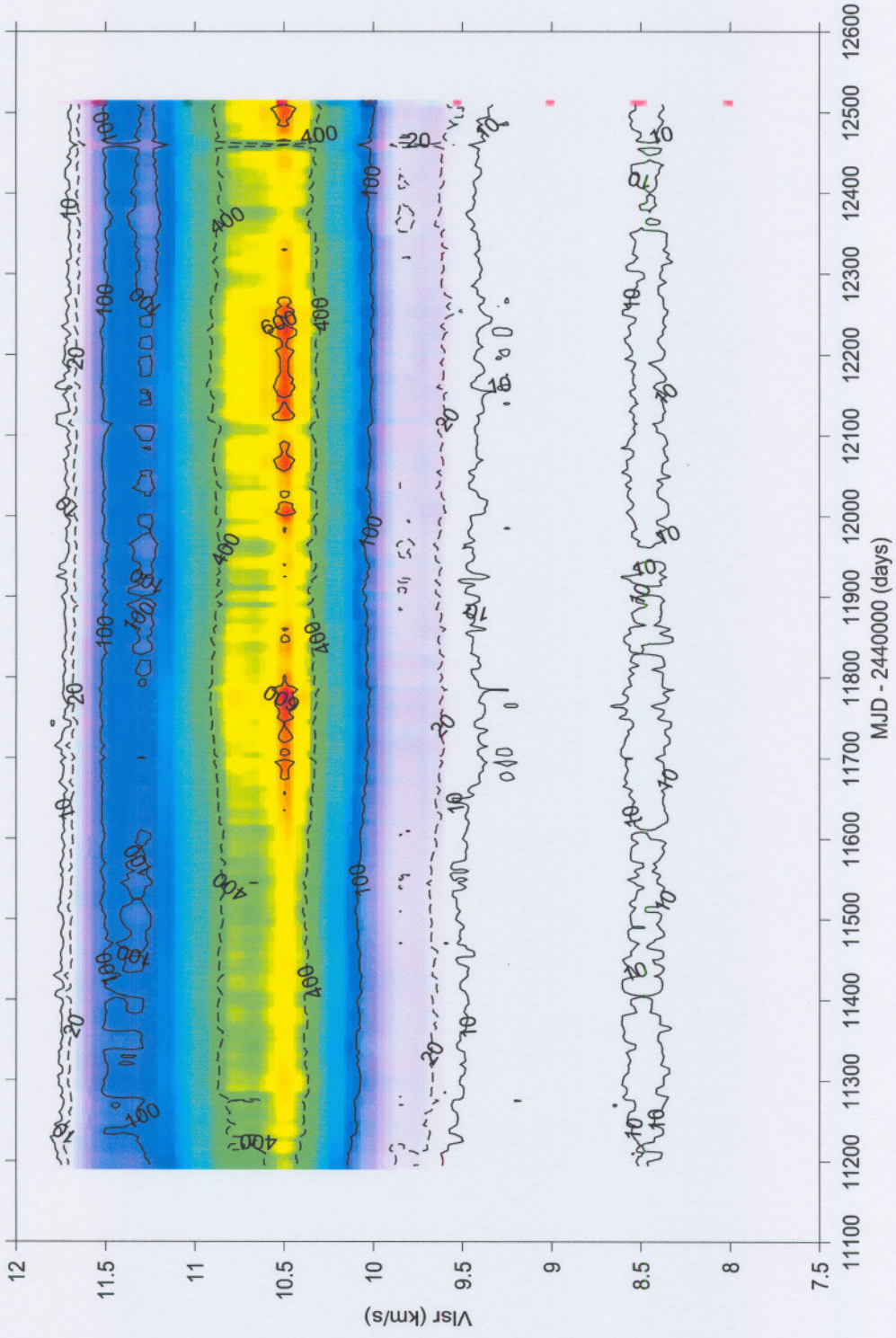

Figure 2: Intensity contour plot for G188.95-0.89

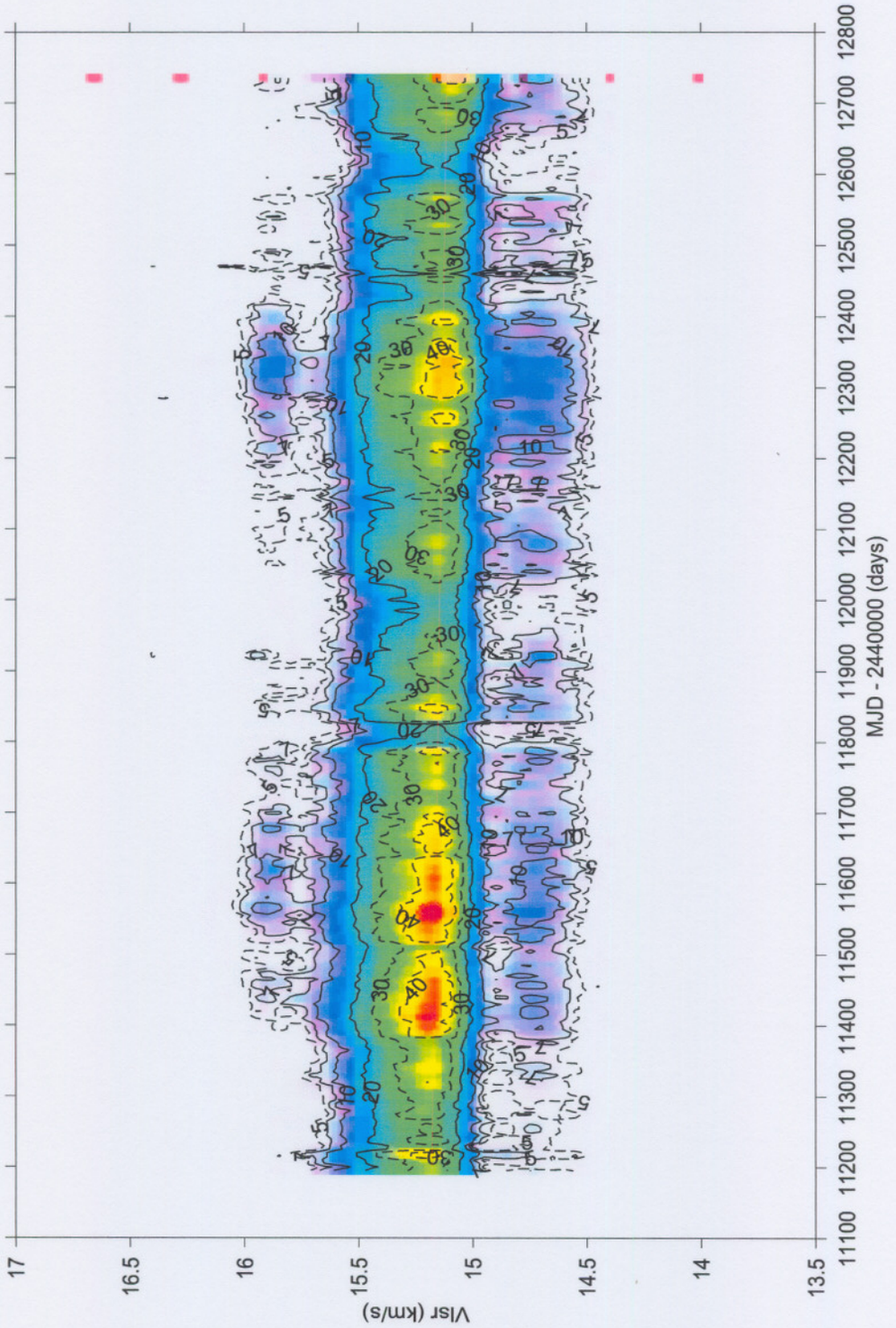

Figure 3: Intensity contour plot for G196.45-1.68

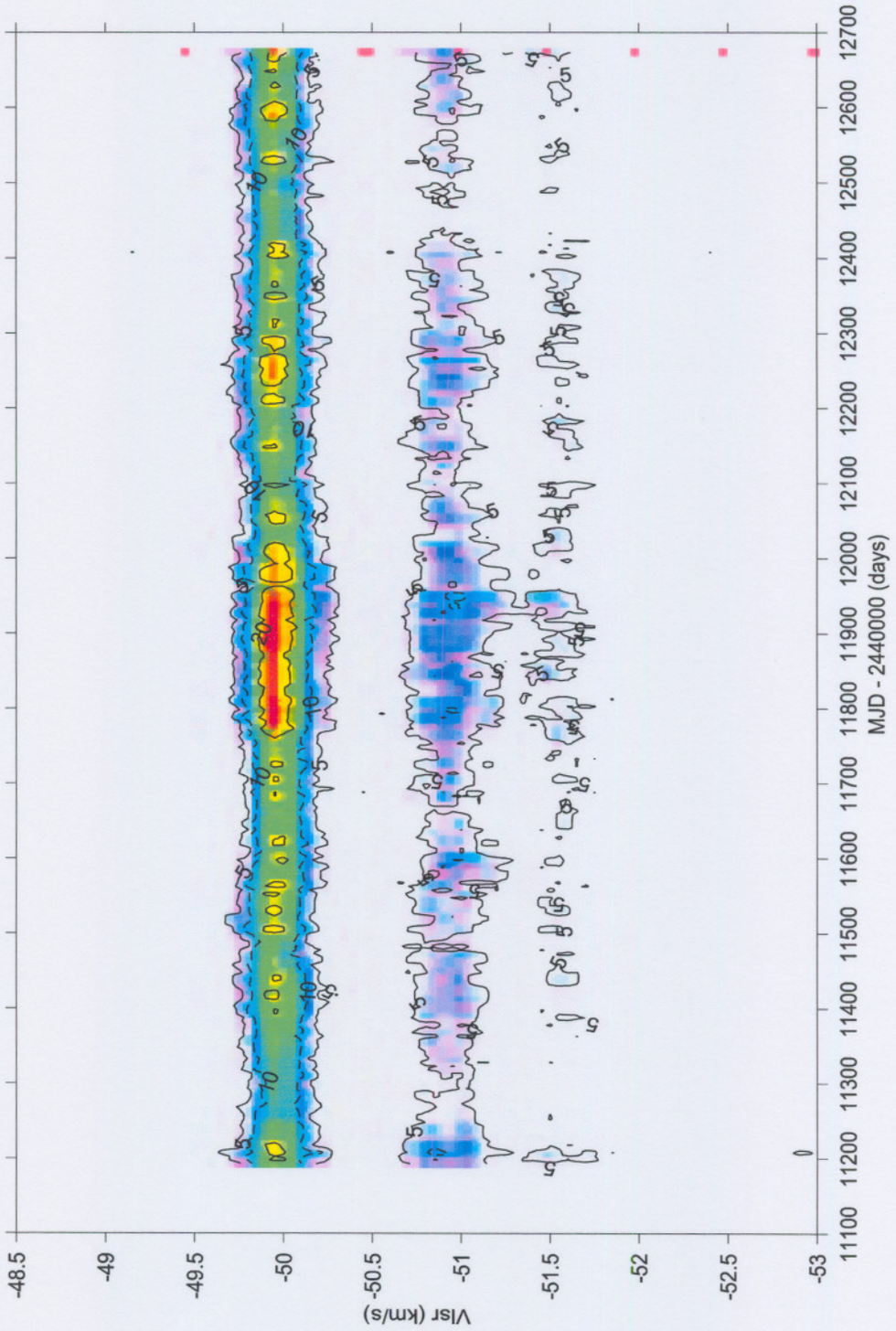

Figure 4: Intensity contour plot for G312.11+0.26

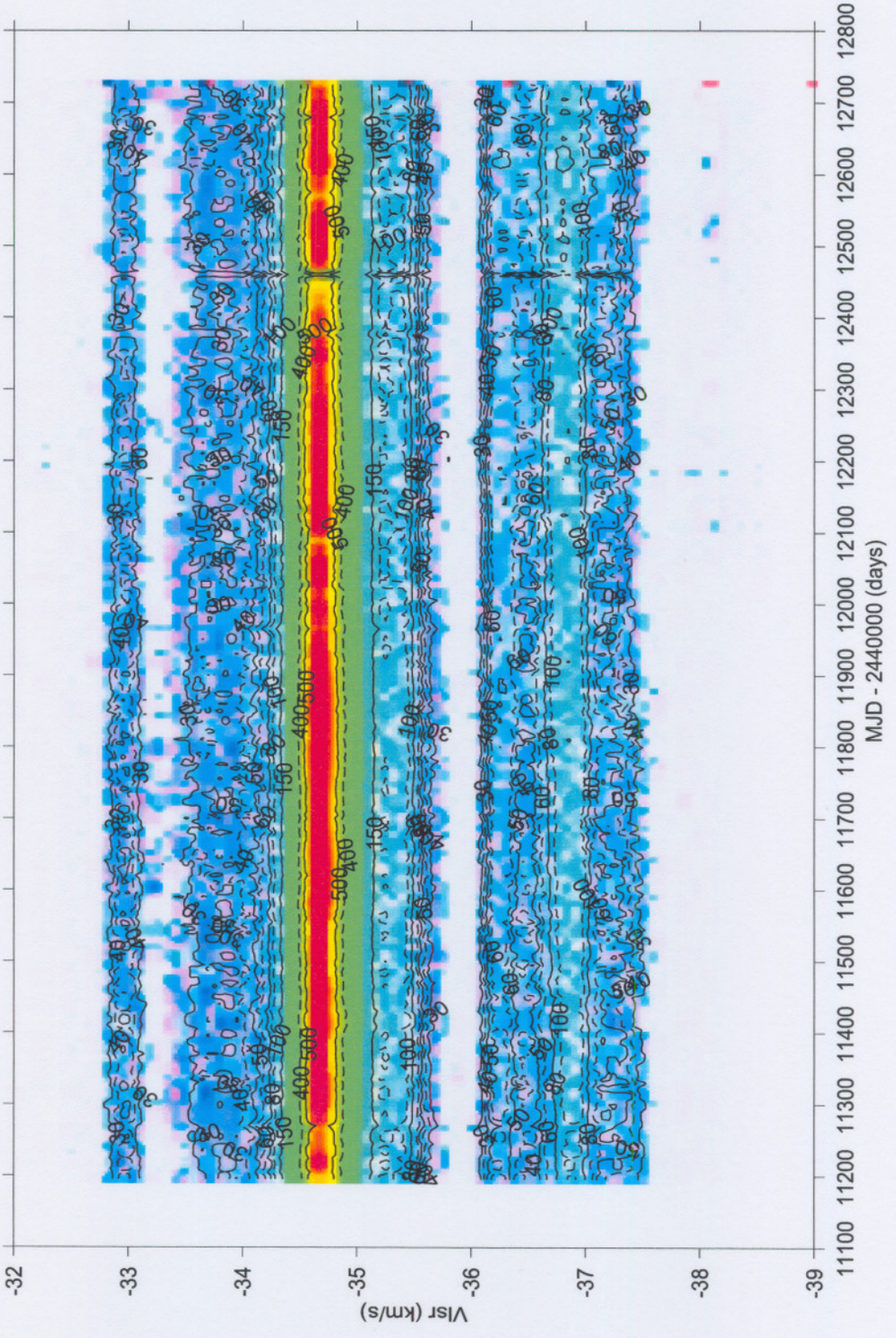

Figure 5: Intensity contour plot for G318.95-0.20

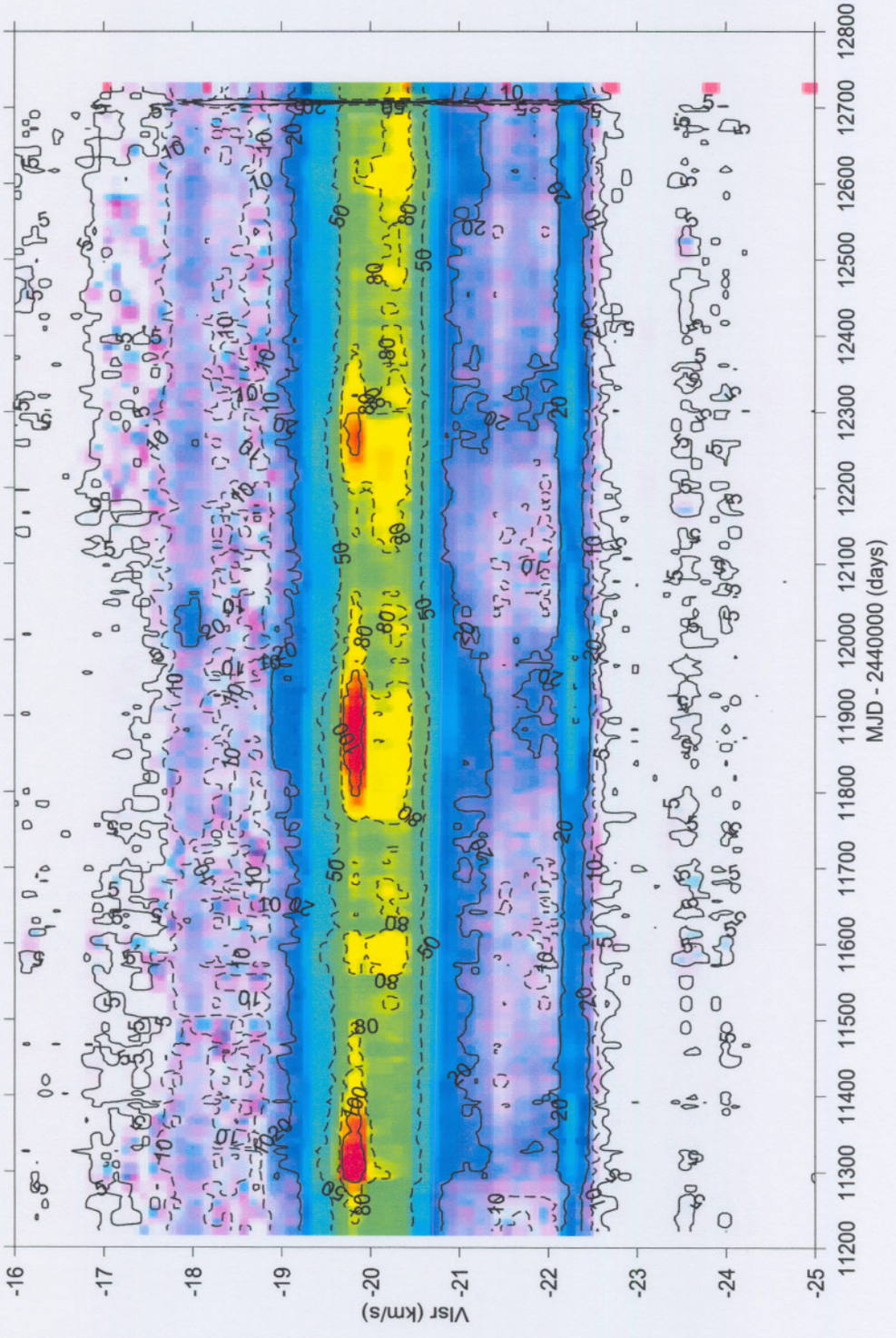

Figure 6: Intensity contour plot for G316.64-0.09

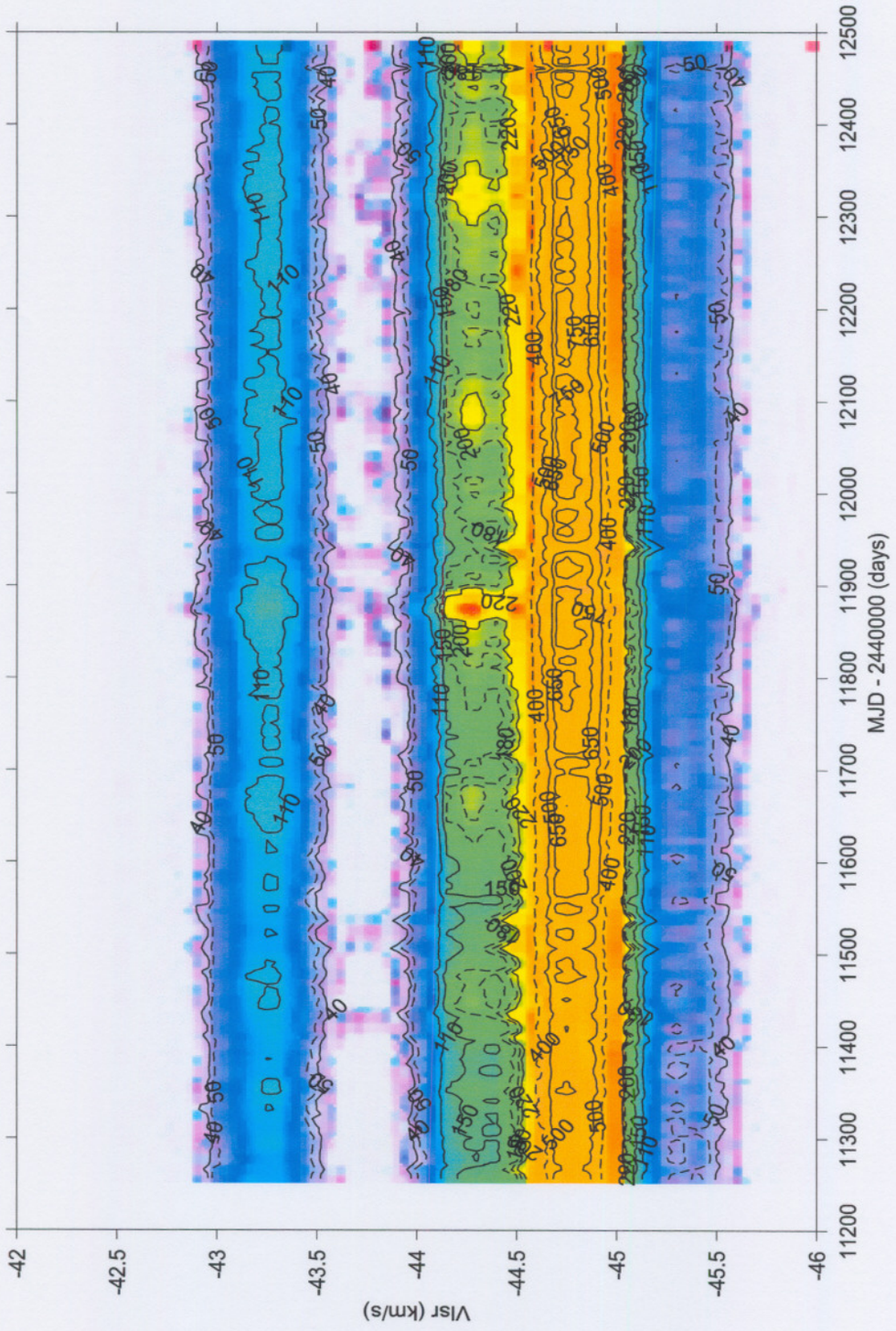

Figure 7: Intensity contour plot for G328.24-0.53

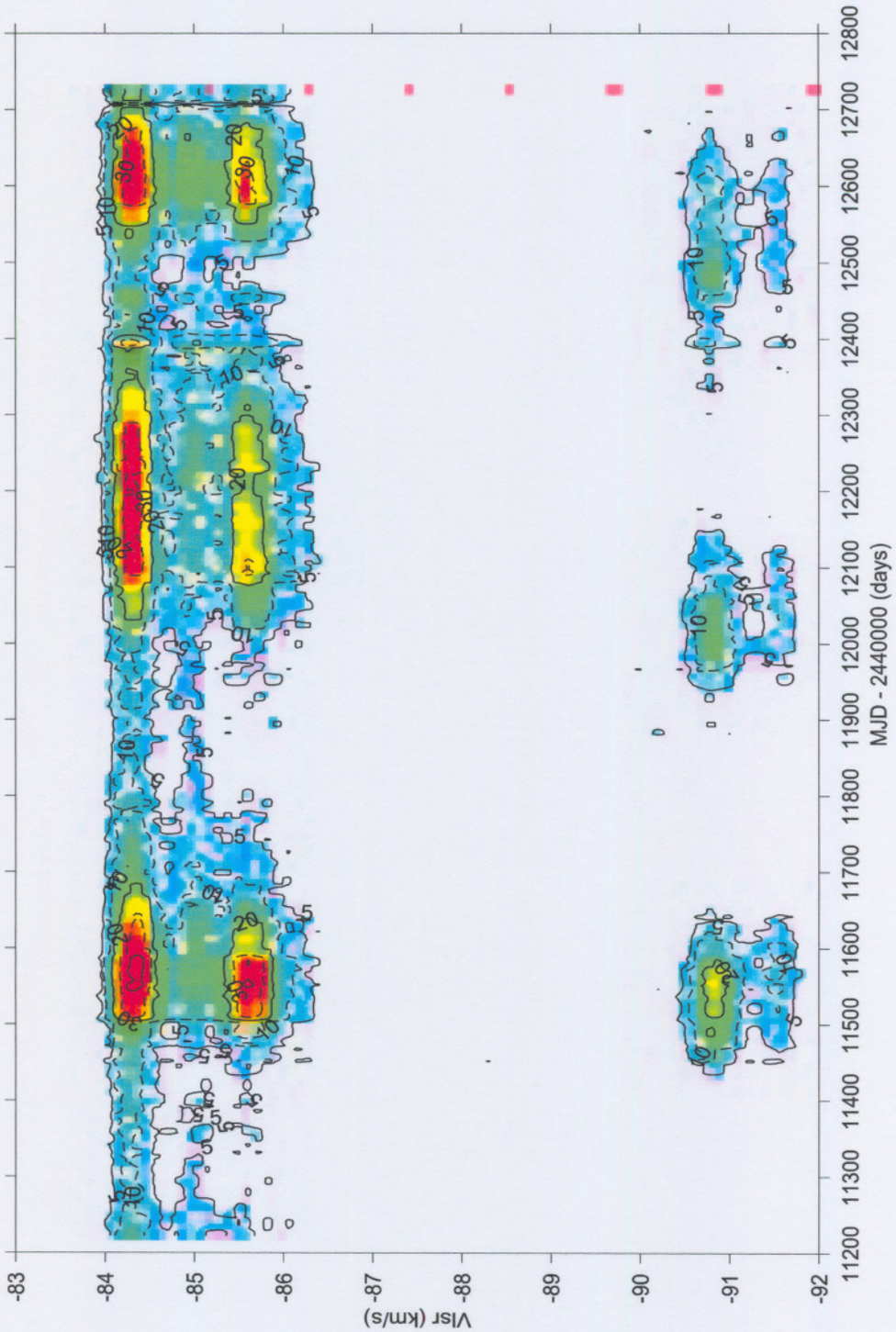

Figure 8: Intensity contour plot for G331.13-0.24

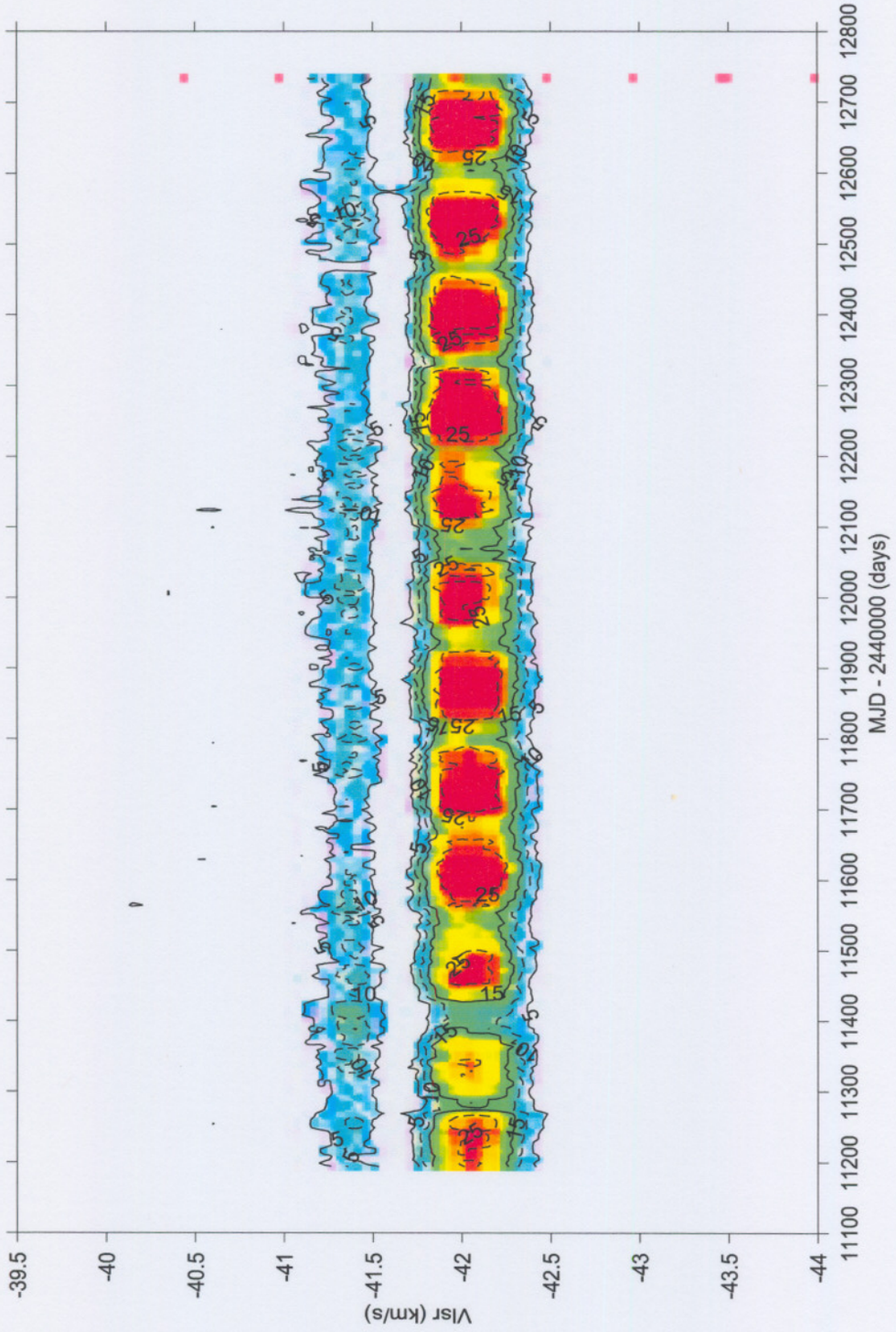

Figure 9: Intensity contour plot for G338.93-0.06

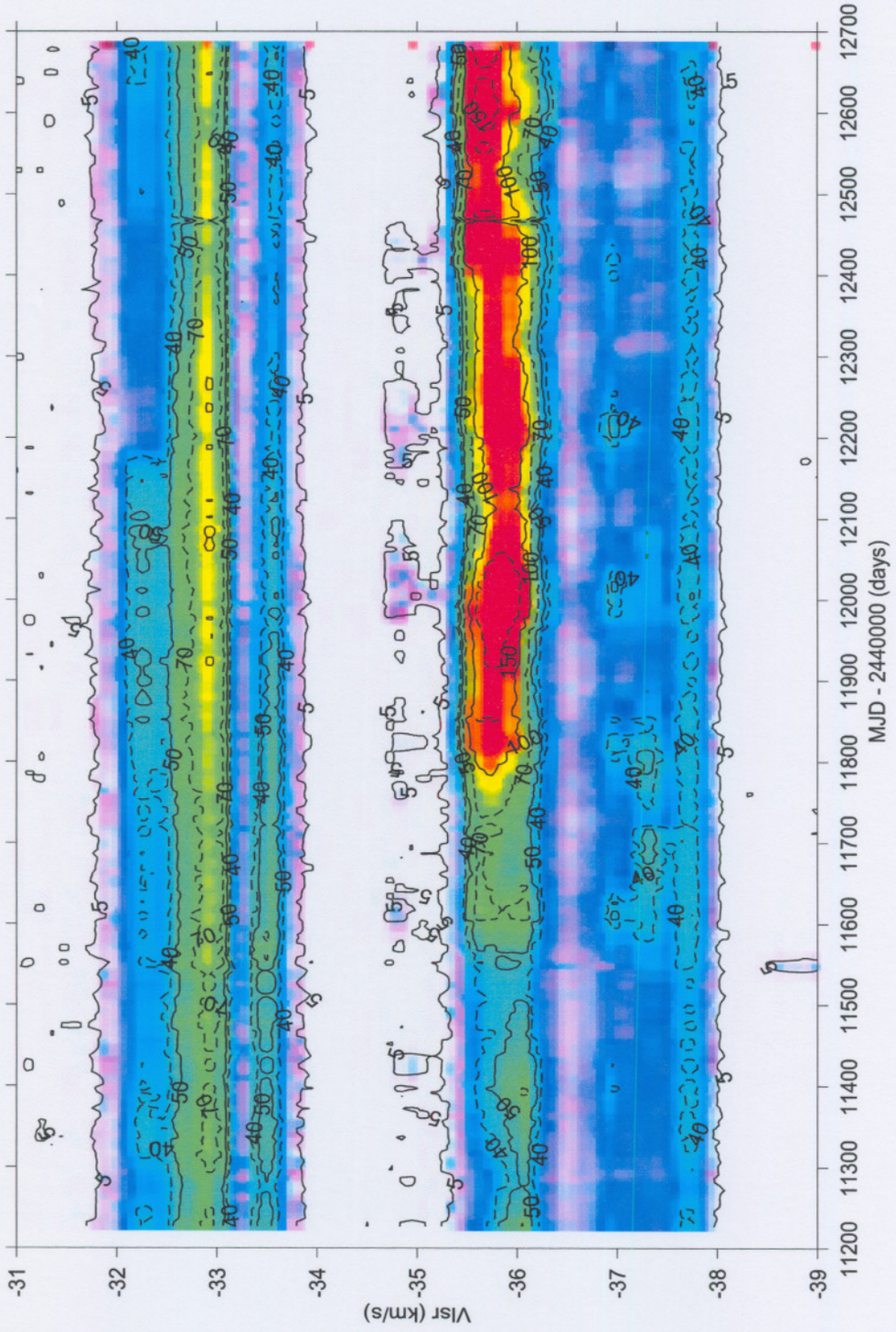

Figure 10: Intensity contour plot for G339.62-0.12

Bibliography

Abt H., 1979, AJ, 84, 1591

Abt H. A., 1983, Ann. Rev. Astron. Astrophys, 21, 343

Alexander T., 1997, in Astronomical time series, Maoz D., Sternberg A., Leibowitz E. M., eds., Kluwer, Dordrecht, p. 163

Argon A. L., Reid M. J., Menten K. M., 2000, ApJS, 129, 159

—, 2003, ApJ, 593, 925

Bachiller R., Terebey S., Jarrett T., Martín-Pintado J., Beichman C. A., D. van Buren, 1994, ApJ, 437, 296

Batchelor R. A., Caswell J. L., Goss W. M., Haynes R. F., Knowles S. H., Wellington K. J., 1980, Aust. J. Phys., 33, 139

Batrla W., Mathews H. E., Menten K. M., Walmsley C. M., 1987, Nat, 326, 49

Becker R. H., White R. L., Helfand D. J., Zoonematkermani S., 1994, ApJS, 91, 347

Beech M., Mitalas R., 1994, ApJS, 95, 517

Beuther H., Schilke P., Gueth F., McCaughrean M., Andersen M., Sridharan T., K.Menten, 2002, A&A, 387, 931

Bieging J. H., Pankonin V., Smith L. F., 1978, A&A, 341, 341

Bonnell I. A., Bate M. R., 2002, MNRAS, 336, 659

Bonnell I. A., Bate M. R., Zinnecker H., 1998, MNRAS, 298, 93

Brand J., Cesaroni R., Caselli P., Catarzi M., Codella C., Comoretto G., Curioni G. P., Curioni P., S. Di Franco, Felli M., Giovanardi C., Olmi L., Palagi F., Palla F., Panella D., Pareschi G., Rossi E., Speroni N., Tofani G., 1994, A&AS, 103, 541

Brand J., Cesaroni R., Comoretto G., Felli M., Palagi F., Palla F., Valdettaro R., 2003, A&A, 407, 573

Bronfman L., Nyman L., May J., 1996, A&AS, 115, 81

Carey S. J., Clark F. O., Egan M. P., Price S. D., Shipman R. F., Kuchar T. A., 1998, ApJ, 508, 721

Carpenter J. M., 2001, ApJ, 121, 2851

Caswell J. L., 1996, MNRAS, 283, 606

—, 1998, MNRAS, 297, 215

Caswell J. L., Haynes R. F., 1983, Aust. J. Phys, 36, 361

Caswell J. L., Vaile R. A., Ellingsen S. P., 1995a, Publ. Astron. Soc. Aust., 12, 37

Caswell J. L., Vaile R. A., Ellingsen S. P., Whiteoak J. B., Norris R. P., 1995b, MNRAS, 272, 96

Caswell J. L., Vaile R. A., Forster J. R., 1995c, MNRAS, 277, 210

Cesaroni R., Churchwell E., Hofner P., Walmsley C. M., Kurtz S., 1994, A&A, 288, 903

Cesaroni R., Felli M., Jenness T., Neri R., Olmi L., Robberto M., Testi L., Walmsley C. M., 1999, A&A, 345, 949

Cesaroni R., Felli M., Testi L., Walmsley C. M., Olmi L., 1997, A&A, 325, 725

Chini R., Krügel E., Kreysa E., 1986, A&A, 167, 315

Churchwell E., Wolfire M. G., Wood D. O. S., 1990, ApJ, 354, 247

Clarke C. J., Bonnell I. A., Hillenbrand L. A., 2000, in Protostars and Planets IV, Mannings V., Boss A., Russell S. S., eds., University of Arizona Press, Tuscon, p. 151

Clegg A. W., 1992, in Astrophysical masers, Arlington, Virginia, USA 1992, Clegg A. W., Nedoluha G. E., eds., Springer-Verlag, p. 279

Cohen M., Walker R. G., Barlow M. J., Deacon J. R., 1992, AJ, 104, 1650

Cragg D. M., Sobolev A. M., Ellingsen S. P., Caswell J. L., Godfrey P. D., Salii S. V., Dodson R. G., 2001, MNRAS, 323, 939

Cragg D. M., Sobolev A. M., Godfrey P. D., 2002, MNRAS, 331, 521

Davis C. J., Moriarty-Schieven G., Eislöffel J., Hoare M. G., Ray T. P., 1998, ApJ, 115, 1118

De Buizer J. M., 2003, MNRAS, 341, 277

De Buizer J. M., Piña R. K., Telesco C. M., 2000, ApJS, 130, 437

De Buizer J. M., Radomski J. T., Piña R. K., Telesco C. M., 2002a, ApJ, 580, 305

De Buizer J. M., Walsh A. J., Piña R. K., Phillips C. J., Telesco C. M., 2002b, ApJ, 564, 327

Deng L., Xiong D., 2001, MNRAS, 327, 881

Durisen R. H., Mejia A. C., Pickett B. K., Hartquist T. W., 2001, ApJ, 563, L157

Egan M. P., Shipman R. F., Price S. D., Carey S. J., Clark F. O., Cohen M., 1998, ApJ, 494, L199

Ellingsen S. P., von Bibra M. L., McCulloch P. M., Norris R. P., Deshpande A. A., Phillips C. J., 1996, MNRAS, 280, 378

Forster J., Caswell J., 1999, A&AS, 137, 43

Forster J. R., Caswell J. L., 1989, A&A, 213, 339

—, 2000, ApJ, 530, 371

Furaya R. S., Kitamura Y., Wootten A., Claussen M. J., Kawabe R., 2003, ApJS, 144, 71

Fürst E., Reich W., Reich P., Reif K., 1990, A&AS, 85, 805

Garay G., Reid M., Moran J. M., 1985, ApJ, 289, 681

Garay G., Rodrígues L. F., Moran J. M., Churchwell E., 1993, ApJ, 418, 368

Gaylard M. J., MacLeod G. C., 1993, MNRAS, 262, 43

Godbout S., Joncas G., Durand D., Arsenault R., 1997, ApJ, 478

Goedhart S., Gaylard M. J., van der Walt D. J., 2003, MNRAS, 339, L33

Goedhart S., van der Walt D. J., Gaylard M. J., 2002, MNRAS, 335, 125

Goedhart S., van der Walt D. J., Schutte A., 2000, MNRAS, 315, 316

Gooch R., 1996, Proc. Astron. Soc. Aust., 14, 106

Griffith M. R., Wright A. E., Burke B. F., Ekers R. D., 1994, ApJS, 90, 179

Halbwachs J. L., 1983, A&A, 128, 399

Haschick A. D., Ho P. T. P., 1983, ApJ, 267, 638

Hillenbrand L. A., 1997, AJ, 113, 1733

Hofner P., Churchwell E., 1996, A&AS, 120, 283

Hofner P., Kurtz S., Churchwell E., Walmsley C. M., Cesaroni R., 1996, ApJ, 460, 359

Hofner P., Wyrowski F., Walmsley C. M., Churchwell E., 2000, ApJ, 536, 393

Hughes V. A., MacLeod G. C., 1993, AJ, 105, 1495

Hunter T. R., Phillips T. G., Menten K. M., 1997, ApJ, 478, 283

Hunter T. R., Taylor G. B., Felli M., Tofani G., 1994, A&A, 284, 215

Kenyon S. J., Kolotilov E. A., Ibragimov M. A., Mattei J. A., 2000, ApJ, 531, 1028

Kholopov P. N., Samus N. N., Frolov M. S., Goranskij V. P., Gorynya N. A., Kireeva N. N., Kukarkina N. P., Kurochkin N. E., Medvedeva G. I., Perova N. B., Shugarov S. Y., 1985, General Catalogue of Variable Stars, 4th edn. Nauka Publishing House, Moscow

Kuchar T. A., Clark F. O., 1997, ApJ, 488, 224

Kurtz S., Cesaroni R., Churchwell E., Hofner P., Walmsley C. M., 2000, in Protostars and Planets IV, Mannings V., Boss A., Russell S. S., eds., University of Arizona Press, Tuscon, p. 299

Kurtz S., Churchwell E., Wood D. O. S., 1994, ApJS, 91, 659

Lada C. J., Adams F. C., 1992, ApJ, 393, 278

Lada C. J., Blitz L., Reid M. J., Moran J. M., 1981, ApJ, 243, 769

Lang K. R., 1992, Astrophysical data: Planets and stars. Springer-Verlag

Langer W. D., van Dishoeck E. F., Bergin E. A., Blace G. A., Tielens A. G., Velusamy T., Whittet D. C., 2000, in Protostars and Planets IV, Mannings V., Boss A. P., Russell S. S., eds., University of Arizona Press, Tuscon, p. 29

Liljeström T., Mattila K., Toriseva M., Anttila R., 1989, A&AS, 79, 19

Lubow S. H., Artymowicz P., 2000, in Protostars and Planets IV, Mannings V., Boss A., Russell S. S., eds., University of Arizona Press, Tuscon, p. 731

MacLeod G. C., Gaylard M. J., 1993, in Astrophysical masers; Proceedings of the Conference, Arlington, VA, USA, 1992, Clegg A. W., Nedoluha G. E., eds., Springer-Verlag, pp. 195–198

—, 1996, MNRAS, 280, 868

McCaughrean M. J., O'Dell C. R., 1996, AJ, 111, 1977

McKee C., Ostricker J., 1977, ApJ, 218, 148

Menten K. M., 1991, ApJ, 380, L75

—, 2002, in IAU symposium 206. Cosmic masers: From protostars to blackholes., Migenes V., Reid M., eds., Astronomical Society of the Pacific, San Francisco, p. 125

Menten K. M., Walmsley C. M., Henkel C., Wilson T. L., 1986a, A&A, 157, 318

Menten K. M., Walmsley C. M., Henkel C., Wilson T. L., Snyder L. E., Hollis J. M., Lovas F. J., 1986b, A&A, 169, 271

Minier V., Booth R. S., Burton M. G., Pestalozzi M. R., 2002a, in Proceedings of the 6th European VLBI Network Symposium, Ros E., Porcas R., Lobanov A., Zensus J., eds.

Minier V., Booth R. S., Conway J. E., 2000, A&A, 362, 1093

—, 2002b, A&A, 383, 614

Minier V., Conway J. E., Booth R. S., 2001, A&A, 369, 278

Minier V., Ellingsen S. P., Norris R. P., Booth R. S., 2003, A&A, 403, 1095

Molinari S., Testi L., Brand J., Cesaroni R., Pallo F., 1998, ApJ, 505, L39

Moscadelli L., Catarzi M., 1996, A&AS, 116, 211

Norris R. P., Byleveld S. E., Diamond P. J., Ellingsen S. P., Ferris R. H., Gough R. G., Kesteven M. J., McCulloch P. M., Phillips C. J., Reynolds J. E., Tzioumis A. K., Takahashi Y., Troup E. R., Wellington K. J., 1998, ApJ, 508, 275

Norris R. P., Whiteoak J. B., Caswell J. L., Wieringa M. H., Gough R. G., 1993, ApJ, 412, 222

Olmi L., R.Cesaroni, Walmsley C. M., 1993, A&A, 276, 489

Osterloh M., Henning T., Launhardt R., 1997, ApJS, 110, 71

Ott M., Witzel A., Quirrenbach A., Krichbaum T. P., Standke K. J., Schalinski C. J., Hummel C. A., 1994, A&A, 284, 331

Ouyed R., Clarke D. A., Pudritz R. E., 2003, ApJ, 582, 292

Palla F., Stahler S. W., 1993, ApJ, 418, 414

Palumbo G. G. C., Scappini F., Pareschi G., Codella C., Caselli P., Attolini M. R., 1994, MNRAS, 266, 123

Persi P., Tapia M., Roth M., Marenzi A. R., Testi L., Vanzi L., 2003, A&A, 397, 227

Persson S. E., Murphy D. C., Krzeminski W., Roth M., Rieke M. J., 1998, AJ, 116, 2475

Phillips C. J., Norris R. P., Ellingsen S. P., McCulloch P. M., 1998, MNRAS, 300, 1131

Poveda A., Allen C., Parrao L., 1982, ApJ, 258, 589

Price S. D., Egan M. P., Carey S. J., Mizuno D. R., Kuchar T. A., 2001, AJ, 121, 2819

Reipurth B., 2000, AJ, 120, 3177

Scalise E., Braz M. A., 1980, A&A, 85, 149

Scalise E., Rodrígues L. F., Mendoza-Torres E., 1989, A&A, 221, 105

Scappaticci G., Watson W. D., 1995, ApJ, 448, 862

Scargle J. D., 1982, ApJ, 263, 835

—, 1989, ApJ, 343, 874

Shepherd D. S., Churchwell E., 1996, ApJ, 457, 267

Slysh V. I., Val'tts I. E., Kalenskii S. V., Voronkov M. A., Palagi F., Tofani G., Catarzi M., 1999, A&AS, 134, 115

Smith N., Bally J., Morse J. A., 2003, ApJ, 587, L105

Smits D. P., 2003, MNRAS, 339, 1

Stahler S. W., Palla F., Ho P. T. P., 2000, in Protostars and Planets IV, Mannings V., Boss A. P., Russell S. S., eds., University of Arizona Press, Tuscon, p. 327

Stetson P. B., 1996, PASP, 108, 851

Tamura M., Gatley I., Joyce R. R., Ueno M., Suto H., Sekiguchi M., 1991, ApJ, 378, 611

Testi L., Felli M., Persi P., Roth M., 1994, A&A, 288, 634

—, 1998, A&AS, 129, 495

Testi L., Felli M., Taylor G. B., 1999, A&AS, 138, 71

Torrelles J. M., Gómez J. F., Rodríguez L. F., Ho P. T. P., Curiel S., Vázquez R., 1997, ApJ, 489, 744

van der Walt D. J., Churchwell E., Gaylard M. J., Goedhart S., 2003, MNRAS, 341, 270

van der Walt D. J., Retief S. J. P., Gaylard M. J., MacLeod G. C., 1996, MNRAS, 282, 1085

Wallin B. K., Watson W. D., Wyld H. W., 1998, ApJ, 495, 774

Walsh A., Lee J.-K., Burton M., 2002, MNRAS, 329, 475

Walsh A. J., Bertoldi F., Burton M. G., Nikola T., 2001, MNRAS, 326, 36

Walsh A. J., Burton M. G., Hyland A. R., Robinson G., 1998, MNRAS, 301, 640

—, 1999, MNRAS, 309, 905

Wood D. O. S., Churchwell E., 1989a, ApJ, 340, 265

—, 1989b, ApJS, 69, 831

Wouterloot J. G. A., Brand J., 1989, A&AS, 80, 149

Wright A. E., Griffith M. R., Burke B. F., Ekers R. D., 1994, ApJS, 91, 111

Xu Y., Zheng X. W., Zhang E. J., Yu Z. Y., Han P., Scalise E., Chen Y. J., 2000, A&A, 364, 232

Yorke H. W., Sonnhalter C., 2002, ApJ, 569, 846

Zeng Q., Lou G. F., 1990, A&A, 228, 480